12-14-2013

Investigation of the Structure-Activity Relationship of Pseudo-Single-Crystal Platinum Electrodes by Scanning Electrochemical Microscopy

Yulin Wang

Recommended Citation

Wang, Yulin, "Investigation of the Structure-Activity Relationship of Pseudo-Single-Crystal Platinum Electrodes by Scanning Electrochemical Microscopy" (2013). *Theses and Dissertations*. 2861.
https://scholarsjunction.msstate.edu/td/2861

Investigation of the structure-activity relationship of pseudo-single-crystal platinum electrodes by scanning electrochemical microscopy

By

Yulin Wang

A Dissertation
Submitted to the Faculty of
Mississippi State University
in Partial Fulfillment of the Requirements
for the Degree of Doctor of Philosophy
in Chemistry
in the Department of Chemistry

Mississippi State, Mississippi

December 2013

Investigation of the structure-activity relationship of pseudo-single-crystal platinum electrodes by scanning electrochemical microscopy

By

Yulin Wang

Approved:

David Wipf
(Major Professor)

William P. Henry
(Committee Member)

Dongmao Zhang
(Committee Member)

Todd E. Mlsna
(Committee Member)

Stephen C. Foster
(Committee Member/Graduate Coordinator)

R. Gregory Dunaway
Professor and Dean
College of Arts & Sciences

Name: Yulin Wang

Date of Degree: December 14, 2013

Institution: Mississippi State University

Major Field: Chemistry

Major Professor: Dr. David O. Wipf

Title of Study: Investigation of the structure-activity relationship of pseudo-single-crystal platinum electrodes by scanning electrochemical microscopy

Pages in Study: 157

Candidate for Degree of Doctor of Philosophy

The study of the structure-activity relationship of electrode surfaces is fundamentally important in electrocatalysis research. Yet, the methods and techniques used for the examination of structure-activity relationship so far are limited by their capabilities, and the exploration of electrochemistry at complex surfaces is very challenging. In this study, the correlation between the electrode surface structure and its corresponding activity in two electrochemical reactions were investigated: an electrochemical etching reaction and an electrocatalysis reaction.

A polycrystalline Pt electrode was galvanically etched to expose the underlying well-defined crystallites serving as pseudo-single-crystal electrodes. Atomic force microscopy (AFM) complemented with electron backscatter diffraction (EBSD) was employed for the elucidation of the effects of electrode surface structure on its etching rate. Electrochemical measurements of the electrocatalytic activity of the hydrogen oxidation reaction on individual grain surfaces were performed with high spatial resolution scanning electrochemical microscopy (SECM) coupled with electron backscatter diffraction (EBSD).

The etching experiment and surface characterization results show the more deeply etched regions on polycrystalline Pt surface correspond to Pt(100). The etching rate of the Pt catalyst is Pt(111), Pt(100), and Pt(110) in increasing order.

The structure-reactivity relationship showed that the catalytic activity for hydrogen oxidation reaction (HOR) increases in the order Pt(100) < Pt(110) < Pt(111), where the Miller index plane represents the terrace orientation of the high-index facets. A clear correlation is observed between the increase in HOR activity and step sites density on a given base orientation. Quantitative kinetic measurements at crystal domains were made from current-potential plots and SECM approach curves.

DEDICATION

I would like to dedicate this dissertation to my parents and my husband.

ACKNOWLEDGEMENTS

First, I would like to express my gratitude to Department of Chemistry and Mississippi State University for giving me the opportunity to study here.

It is a great opportunity for me to express my sincere appreciation to my Ph. D. advisor, Dr. David O. Wipf, for his invaluable guidance, patience, encouragement, and support during my research. I would like to express my deepest appreciation to him for guiding me through the Ph.D. study. Without him, this dissertation would be impossible. I would also like to thank my committee members: Dr. William P. Henry, Dr. Dongmao Zhang, Dr. Todd E. Mlsna, and Dr. Stephen C. Foster for all their help. I thank Dr. Stephen C. Foster, the graduate coordinator, for his time, patience, and support during my Ph.D. study. I would like to thank Dr. Deb Mlsna, Dr. Sean Stokes, Mr. Steven C. Holman, lab coordinators, for their teaching and help in my TA work. My special thanks go to Dr. I-wei Chu at the Institute for Imaging & Analytical Technologies for all her help in conducting AFM experiments.

I would like to thank all my lab mates: Maria C. Cebada-Ricalde, Changhong Han, Migelhewa Kaumal, Hadi Khani, David C. Clark, and Timothy J. Dowell for their encouragement and support at all times during my Ph.D. study. I am extremely grateful to Maria, my best friend in life, who has always been there for me whenever I needed her.

I would like to extend my thanks to all the graduate students in the Department of Chemistry at Mississippi State University for their friendship.

Last but not the least, I would like to thank my parents, my husband, and all my friends, for their unconditional love and support in my life. Without them, I would not have made it this far.

TABLE OF CONTENTS

CHAPTER

LIST OF TABLES

LIST OF FIGURES

CHAPTER I

INTRODUCTION

1.1 Structure-Activity Relationship of Solid Metallic Materials

Metals, as a very developed engineering material, are widely used in transportation, bridges, construction, tools, heavy manufacturing, and recently biomedical, electronics, etc. Many properties of metals, such as yield strength, elongation, ultimate tensile strength, thermal conductivity, corrosion resistance, and electric resistance are directly and sensitively related to the material's microstructure.[1] The microstructure covers a wide range of structural features at microscopic dimensions, such as grain size, dislocation densities, particle volume fractions, microcracking, and microporosity.[2] For example, the mechanical strength of many metals and alloys depends strongly on the grain size.[3] The chemical and functional characteristics of metal electrodes are highly based on the electrode material composition and the physical nature of its surface.[4-5] The grains, grain boundaries, and grain orientations are part of the microstructural features of the crystalline material. The understanding of the relationship between microstructure and properties of materials plays an important role in the control and development of metallic materials.[1]

1.2 Platinum Catalysts

Platinum as one of the noble metallic materials has been overwhelmingly involved in the field of jewelry, energy, medicine, aerospace, electronics, etc. owing to its distinctive chemical and physical properties such as enhanced strength and toughness, excellent thermal and electrical conductivity, and high melting point. It is also of great technological importance in modern chemical industry, automobile exhaust purification, and fuel cells as electrocatalysts.[6-7] However, as fuel cells catalysts, its high price and non-ideal catalytic performance have detained the wide commercialization of low-temperature fuel cells. There is much interest in replacing Pt with less expensive metal materials while maintaining catalytic activity at least equal to that of Pt, such as non-platinum catalysts,[8-11] transition metal alloys,[12-14] and metal oxides[15]. However, platinum is still considered to be among the most efficient and widely used electrocatalyst for a variety of reactions.[16-17] In addition, it is well known that the electrochemical behavior of metal catalysts strongly depends on the structure of the electrode material.[5, 18] Therefore, it is of fundamental importance to understand the structure-activity relationship of platinum electrodes in order to find optimum forms of Pt catalysts with enhanced catalytic activity and stability. Accordingly, the development of new types of Pt-based electrocatalysts and the industrial manufacture processing route in relevant fields can be rationally tuned.

1.2.1 Surface Structure of Pt

Metal single-crystal planes can provide a variety of surface structures with well-defined atomic arrangements, and they have been used as model catalysts for the structure-activity relationship study during the past decades.

The surfaces of crystals are typically denoted by Miller indices, a universal notation to designate planes and lattice vectors in bulk lattice. There are two kinds of Miller indices: the Miller indices for a plane in a lattice, and the Miller indices for a given direction in a crystal lattice. An arbitrary surface plane on a cubic crystal can be denoted by the Miller indices as (*hkl*) which is orthogonal to a [*uvw*] direction, where *h*, *k*, *l* are three integers based on the reciprocal of the intersects of the plane with the axes of a coordination system that is defined by the unit cell.[19] In cubic crystals, the Miller indices are the same for a crystal plane and its normal direction.[2]

A model of a face-centered cubic (fcc) unit cell with highlighted low-index planes (100), (110), and (111) is shown in Figure 1.1. The schematic of the packing arrangement of atoms in the low Miller index surface planes of an fcc crystal is illustrated in Figure 1.2. It can be seen that Pt(100) and Pt(111) planes are flat on the atomic scale with a close-packed structure, but Pt (110) place has a rough surface with step atoms.

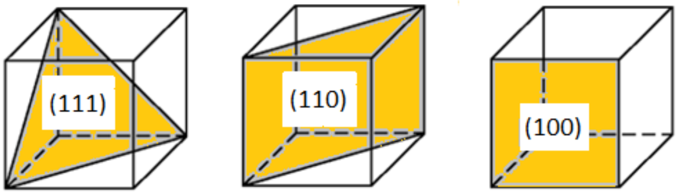

Figure 1.1 A schematic of the (111), (110), (100) planes in a cubic lattice.[20]

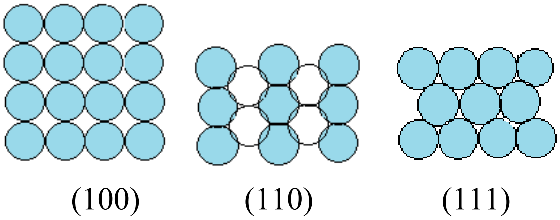

Figure 1.2 The (100), (110), and (111) faces of an FCC crystal.[21]

The high-index surfaces are planes where at least one Miller index is bigger than unit. They usually consist of regularly spaced terraces and steps. Most of the high-index surfaces have close-packed terraces separated by steps one atom in height, which is denoted as a stepped surface and the general notation is Pt (s)-[$n(h_tk_tl_t) \times (h_sk_sl_s)$]. If the steps themselves are high-index faces, this kind of stepped surface is termed a kinked surface.[17] The unit stereographic triangle of fcc structure is shown in Figure 1.3. In this graph, three vertices represent three typical low-index facets (100), (110), and (111) while the three connecting lines are called zone axes. For example, the line extending between the (100) and (110) planes is called [001] zone axis. The single crystal plane with a terrace-step surface lies on these three lines. Other planes within the center of the stereographic triangle are also high-index planes but have a mixture of terraces, steps, and kinks. These surfaces are often difficult to describe and are rarely studied.[19]

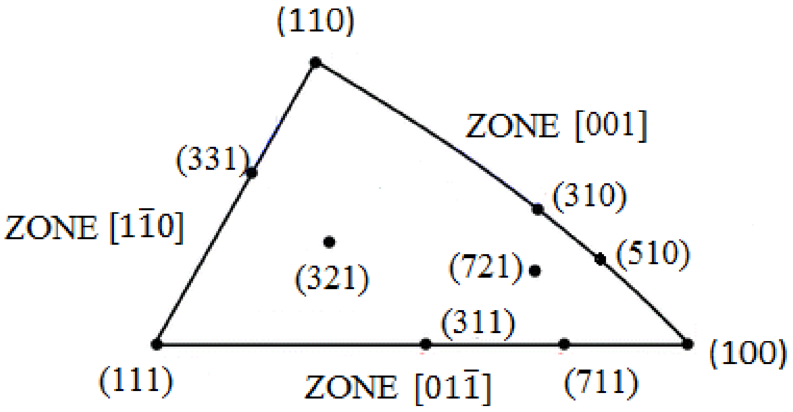

Figure 1.3 Unit stereographic triangle for the fcc structure.[7]

1.2.2 Previous Studies of Structure-Activity Relationship on Pt Catalysts

A lot of work involving Pt single-crystal electrodes with well-defined surface structure has been conducted to investigate the relationship between the surface structure of the Pt catalysts and the electrochemical characteristics including activity, selectivity, and stability.[7,10,17,22-26]

It has been reported that high-index single crystal surfaces with an open structure exhibit superior catalytic performances to the low-index planes. In the case of electrooxidation of methanol, the catalytic activity is found to have an order of Pt(110) > Pt(100) > Pt(111) on low-index planes.[27] However, the catalytic activity is greatly promoted after introducing step atoms on the surface. Koper et al. reported the order of the activity is Pt(111) < Pt (110) < Pt(554) < Pt(553) of the Pt single crystal planes lying in the [1$\bar{1}$0] zone for methanol oxidation.[28-30] Stepped surfaces belonging to the [1$\bar{1}$0] zone were also studied for electrooxidation of methanol, and Pt(755) was found to possess the highest catalytic activity. The activity decreases with an increase in step atom density as the order shows Pt(755) [= 6(111) × (100)] > Pt(211) [= 3(111) × (100)] > Pt(311) [= 2(111) × (100)].[31] The oxidation of CO was also studied on high-index and low-index Pt surfaces in acidic and alkaline solutions, respectively. Lebedeva et al. demonstrated that the active sites for CO oxidation consist of step atoms and the rate constant is proportional to the step fraction on the Pt surface in 0.5 M H_2SO_4.[32-33] Garcia et al reported the activity order of CO oxidation in alkaline solution is kinks > steps > terraces based on their observations from voltammetry.[34] The kinetics of oxygen reduction reaction (ORR) have been extensively studied using the rotating ring-disk electrode with Pt single crystal surfaces. It is demonstrated that the electrocatalytic activity vary with the crystal faces in a different manner depending on the electrolyte composition. It was reported that the catalytic activity on Pt low-index single crystals follows the order Pt(111) < Pt(100) < Pt(110) in H_2SO_4. However, the order of activity increases in the sequence Pt(100) < Pt(110) < Pt(111) in KOH solution.[24] Feiliu et al. studied the structure-activity relationship of Pt high-index surfaces lying in the $[1\bar{1}0]$ and $[01\bar{1}]$ zones for the oxygen reduction reaction. Their results show that stepped surfaces exhibit higher catalytic activity than low-index surfaces, irrespective of step site symmetry. Moreover, they reported that the Pt(211) plane holds the highest catalytic activity for ORR among the studied planes lying in the $[01\bar{1}]$ zone, and the exchange current density (i.e. the reaction rate) for ORR of Pt(211) is over 10 times higher than that of Pt(111) and 4 times higher than that of Pt(110) in 0.5 M H_2SO_4. Furthermore, the differences in catalytic activity of these surfaces become less significant when the experiments were conducted in 0.1 M $HClO_4$ solution.[35-38] The catalytic selectivity and stability were also investigated on Pt high-index surfaces. Tarnowski et al. reported an increase in the yield of CO_2 in electrooxidation for ethanol of Pt stepped surface compared to Pt basal planes for a surface catalytic selectivity study.[39] In addition, the stability of high-index surface was demonstrated by Sun and co-workers.[40] Pt(331) exhibits the highest activity and stability among Pt(331), Pt(332), Pt(111), and Pt(110) electrodes.[40]

1.3 Hydrogen Oxidation Reaction

The hydrogen oxidation reaction (HOR) has attracted a great deal of attention over the last century due to its great importance as a fundamental electrocatalytic reaction in electrochemistry and its application in energy conversion and storage, especially its practical utility as an anode reaction in the area of fuel cells. Intense research has been conducted to develop an understanding of its kinetics and mechanism on a variety of metallic catalysts and in different aqueous solutions in the search for better catalysts for use in fuel cells and other electrochemical applications. [41-43] The mechanism of the hydrogen oxidation reaction on polycrystalline metal surfaces is generally accepted to involve two steps: the initial adsorption of hydrogen molecules and a charge-transfer step. The reactions are as follows:[18]

Tafel: $$\mathrm{H_2 \rightarrow 2H_{ad}} \tag{1.1}$$

Heyrovsky: $$\mathrm{H_2 \rightarrow H_{ad} + H^+ + e^-} \tag{1.2}$$

Volmer: $$\mathrm{H_{ad} \rightarrow H^+ + e^-} \tag{1.3}$$

The first step takes place either by the dissociation of hydrogen molecules into atoms (Equation 1.1) or the dissociation into ion and atom (Equation 1.2). The rate determining step is generally believed to be the Tafel and Heyrovsky reactions for both the proposed Tafel-Volmer and Heyrovsky-Volmer mechanisms.[44-45]

1.3.1 Previous Study of the Electrocatalysis of HOR on Pt Catalysts

Up to now, hydrogen oxidation has been examined extensively on Pt single crystal electrodes,[46] Pt polycrystalline electrodes,[47-48] Pt-based multi-component catalyst,[49-50] and Pt nanocatalysts[51-52] to investigate the influence of catalyst surface structure, metal crystal orientation, catalyst composition, and catalyst loading on the electrocatalytic activity. For example, Marković's group studied the relationships between the atomic-scale structure and electroanalytic activity in electroanalysis of HOR using Pt (111), Pt (100), Pt (110) single crystal electrodes.[53-54] Nicholson et al. reported the effect of Pt nanoparticle loading on the heterogeneity of catalytic reactivity towards the hydrogen oxidation reaction.[55]

The structure-sensitivity of HOR was first demonstrated by Marković et al. and then by Conway and co-workers on low-index Pt single crystals. The activity is in the order (111) < (100) < (110) for HOR in both alkaline and acid solution as reported by Marković et al.[46,53] The findings in Conways's work showed the activity order is (100) < (111) < (110) for Pt single crystals which is different from Marković's results.[56-57] Both Marković and Conway et al. have proposed the reactive intermediate on Pt surfaces is the overpotentially deposited hydrogen (H_{opd}) state which is a relatively weakly adsorbed hydrogen state compared with the underpotentially deposited hydrogen (H_{upd}). [26] The effects of anion adsorption on Pt low-index surfaces have been reviewed, and the strength of interaction increases in the sequence $ClO_4^- < HSO_4^- < Cl^- < Br^- < I^-$.[24] It has been reported that the adsorption of these anions on metal electrodes generally have adverse effects on the kinetics for fuel cell reactions.[18, 24,43] Marković et al. reported that the ORR is strongly inhibited on Pt(100) surface modified with adsorbed Cl^- (Cl_{ad}), and the inhibition effect is small on Pt(111)-Cl_{ad}. The results also show there is no inhibition effect of Cl_{ad} on the kinetics of HOR on Pt(111), but large inhibition of HOR on Pt(100) was observed.[23] The adsorption of hydrogen sulfate ion (HSO_4^-) showed a blocking effect on Pt(111) and Pt(110), but no effect on Pt(110) in the study of the HOR. [58]

1.4 Scanning Electrochemical Microscopy (SECM)

SECM, as one type of scanning probe microscopy (SPM) has been employed in the study of a wide range of electrochemical processes.[59-60] It was introduced in the late 1980s and has developed into a powerful technique that can be applied to the study of biophysical systems, biological processes, dissolution processes, heterogeneous and homogeneous reactions, surface reactivity, local corrosion, charge transfer mechanism, liquid/liquid interface, and adsorption and desorption.[60-61]

The SECM instrument uses an ultramicroelectrode (UME) as the probe to scan over the surface of interest using a high-precision position controller. A bipotentiostat is employed to adjust the potential of the UME and the substrate electrode to induce an electrochemical reaction, and record the corresponding current due to the reaction.

The schematic diagram of feedback mode of SECM operation is illustrated in Figure 1.4. In SECM imaging experiments, the UME is positioned over the substrate electrode in an electrolyte solution at a close tip-substrate separation. When the tip is rastered across the substrate surface, an electrochemical activity map of the scanned area on the substrate is produced based on the perturbation of the tip signal by the substrate surface. The electrochemical response of the probe is recorded as a function of the lateral position of the probe for sample imaging. The mechanism is mainly due to the nature and the local properties of the substrate electrode material such as its composition, surface topography, and structure.[59]

In the SECM approach-curve experiment, a tip approaching a conducting surface causes a tip current to increase as the tip-substrate distance decreases due to the extra flux of redox active species between the tip and the substrate. This phenomenon is termed positive feedback. On the other hand, the tip current decreases if it is brought close to an insulating surface because the electron transfer between the solution mediator and the substrate is blocked by the nonconducting surface. This decrease in tip current is called negative feedback. This operation mode where only the tip current is monitored is called feedback mode.[61]

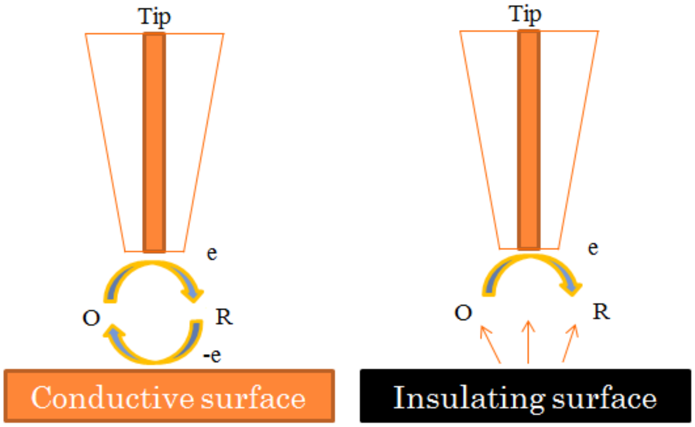

Figure 1.4 Schematic diagram of SECM feedback mode.[61]

Notes: (a) Positive feedback at a conductive substrate. (b) Negative feedback at insulator substrate. R is an oxidizable species and O is the oxidized form of R.

There is also generation/collection (G/C) mode in SECM where both tip and substrate can be used as working electrodes. One working electrode generates electroactive species that are collected at the other electrode. There are two different G/C modes: tip generation/substrate collection (TG/SC) mode and substrate generation/tip collection (SG/TC) mode. A TG/SC experiment measures both tip and substrate current simultaneously, and it has been applied in homogeneous and heterogeneous electron transfer studies. The SG/TC mode is most useful for concentration profile measurement experiments. It was reported that the collection efficiency in SG/TC mode is much lower than that in TG/SC mode, and the tip/substrate separation distance is difficult to control in SG/TC mode.[60-61]

In addition, there are other operation mode derived from basic feedback mode and G/C mode, such as ion-transfer feedback mode,[62] penetration mode,[63] equilibrium perturbation mode,[59] and further instrumentation development for various electrochemical processes investigation and electrochemical response measurements such as alternating current impedance feedback (AC-SECM)[64] and scanning electrochemical cell microscopy (SECCM).[61,65]

Furthermore, the combination of SECM with other analytical methods with simultaneous measurements has been proposed and has become a powerful approach to the studies of surface structures and dynamics. These hybrid techniques include AFM-SECM, SPR-SECM, FS-SECM, NSOM-SECM, etc.[60,66-67]

1.4.2 Study of the Electrocatalysis of HOR on Pt catalysts by SECM

Many methods have been used to study the hydrogen oxidation reaction on platinum catalysts including cyclic voltammetry,[68-70] rotating disk electrode (RDE) and rotating ring disk electrode (RRDE) techniques,[49,71-74] and recently, scanning electrochemical microscopy (SECM).[44, 75-77] However, the capability and sensitivity of these voltammetry techniques are restricted in carrying out HOR studies due to ohmic drop, double-layer charging, and mechanical limitations. In addition, the preparation of single crystal Pt electrodes with only a single surface orientation each time is very challenging as well as expensive and time-consuming—requiring extreme care and caution.[25, 78]

As one of the local electrochemical measurement techniques, SECM is a powerful tool to characterize the redox activity of the HOR reaction at the metal catalyst electrode/electrolyte interface owing to its high spatial resolution and electrochemical sensitivity. It employs an ultramicroelectrode (UME) as the probe which increases the mass transfer rate constant to a great extent compared to an RDE method. For example, in order to reach the same mass transfer rate constants as in SECM, it would require at least 10^6 rotations per minute (rpm) rotation rate in the RDE measurement.[79] Thus, kinetic rate constants obtained with SECM are two to three orders of magnitude higher than allowed by RDE voltammetry. Moreover, the steady-state kinetic measurement employed in SECM has liberated it from the difficulties (ohmic drop, double-layer charging problems, and mechanical issues) of conventional hydrodynamic-based voltammetry techniques.[66, 75]

Electrocatalysis of HOR and ORR are the two most studied electrocatalytic reactions by SECM owing to their importance in fuel cells and other applications. The rates of these two reactions strongly depend on the catalytic activity of the substrate surface.[60] Both SECM electrochemical activity imaging and the approach curve methods have been used to explore the mechanism and kinetics of HOR on Pt metal catalysts. Zhou et al. have studied the electrocatalysis of hydrogen oxidation in $HClO_4$ and HNO_3 solution at platinum substrates using SECM feedback mode, and examined the inhibitory effect of adsorbed Br^-, Cl^- and NO_3^- on the kinetics of HOR.[77] Kucernak et al. investigated the hydrogen evolution reaction on platinum catalyst dispersed onto a highly orientated pyrolytic graphite (HOPG) electrode.[80] Linkov et al. studied the hydrogen oxidation and evolution reaction on a HOPG, and a Pt-polyaniline-HOPG substrate surface with SECM feedback, substrate generation/tip collection (SG/TC), and chronoamperometric modes.[51] The authors quantitatively determined the heterogeneous electron transfer rates for the HOR reaction by SECM approach curves. Zoski examined the mechanism and kinetics of HOR at polycrystalline noble metal electrodes (Pt, Ir, and Ru), and reported the rate constants for HOR on Pt (0.22 cm/s), Ir (0.25 cm/s), and Ru (0.001 cm/s) obtained by fitting SECM experimental approach curves to theory.[47]

The combinatorial screening methods developed by Xiang et al.[81] have been widely applied in the field of heterogeneous catalysis in searching for novel metallic electrocatalysts. Jayaraman and Hillier have used this screening method to quantitatively detect protons at a surface covered nonuniformly with a platinum layer using SECM feedback mode. The variation in reactivity of the platinum catalysts for HOR was measured directly as a function of spatial position. It was found that the local rate constant value was proportional to the local platinum surface coverage.[76] The same group used SECM to study the kinetics of HOR on platinum and the poisoning effect of CO.[48] In addition, they reported the HOR activity on Pt_xRu_y and $Pt_xRu_yMo_z$ in the absence and presence of a monolayer of CO. Their results demonstrated that CO tolerance was significantly increased by introducing small amounts of Ru and Mo to Pt.[82]

1.5 Electron Backscatter Diffraction (EBSD)

EBSD imaging is a powerful quantitative metallographic technique. It captures electron diffraction patterns which can be used to determine grain morphology, crystallographic orientation and texture, grain boundary character, phase identity and distribution of the sample from small volumes of material in a scanning electron microscope.[83]

The fundamental diffraction on which EBSD is based was first observed by Kikuchi in 1928.[84] The coupling of electronic diffraction with scanning electron microcopy developed by Verables, Harland, and Dingley enables micrometric scale examination of a specimen that is prepared by a routine metallographic method.[84] Figure 1.5 shows the schematic diagram of the EBSD experiment.

A crystalline specimen is placed in the SEM chamber at a highly tilted angle, typically 70 degrees, toward the detector. When an incident beam from the pole piece hits the sample, the resultant backscattering electrons from the sample are collected by a phosphor screen and CCD camera, to form an electron backscatter diffraction pattern (EBSP). Each pattern consists of a set of diffraction bands termed Kikuchi bands which correspond to each of the lattice diffracting planes and are characteristics of the crystal structure. The geometrical arrangement of bands is closely related to the orientation of the diffraction lattice. For example, the angles between the bands and the width and intensity of the bands are directly related to the angles between the lattice planes and the spacing of atoms in the crystallographic planes.[86]

An overview of EBSD indexing procedure from pattern capture to crystal orientation determination is illustrated in Figure 1.6. EBSD maps are formed by moving a focused probe of electrons point by point across a grid of positions on the sample surface.[87] After the Hough transform, band determination and indexing, the phase and orientation and other microstructual-crystallographic information of the crystal specimen are achieved.[87] The spatial resolution of EBSD is related to the resolution of SEM. For modern FE-SEMs, 20 nm grains can be measured with reasonable accuracy.

Over the last two decades, EBSD techniques have been extensively used to study various inorganic crystalline materials including metals, minerals, semiconductors, and ceramics. Currently, the complementary use of EBSD with other techniques is employed to enhance material characterization by detailed microstructure characterization and better understanding of material properties, such as EBSD and AFM,[88] EBSD and EDS.[89]

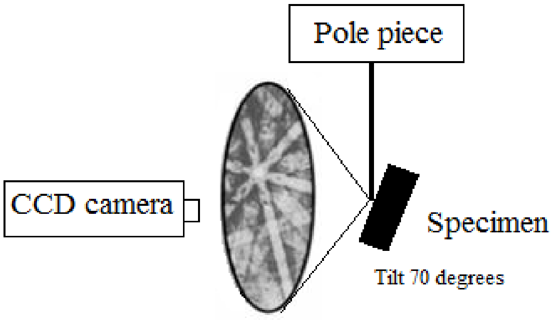

Figure 1.5 Schematic diagram of the experimental set-up for EBSD observations.[85]

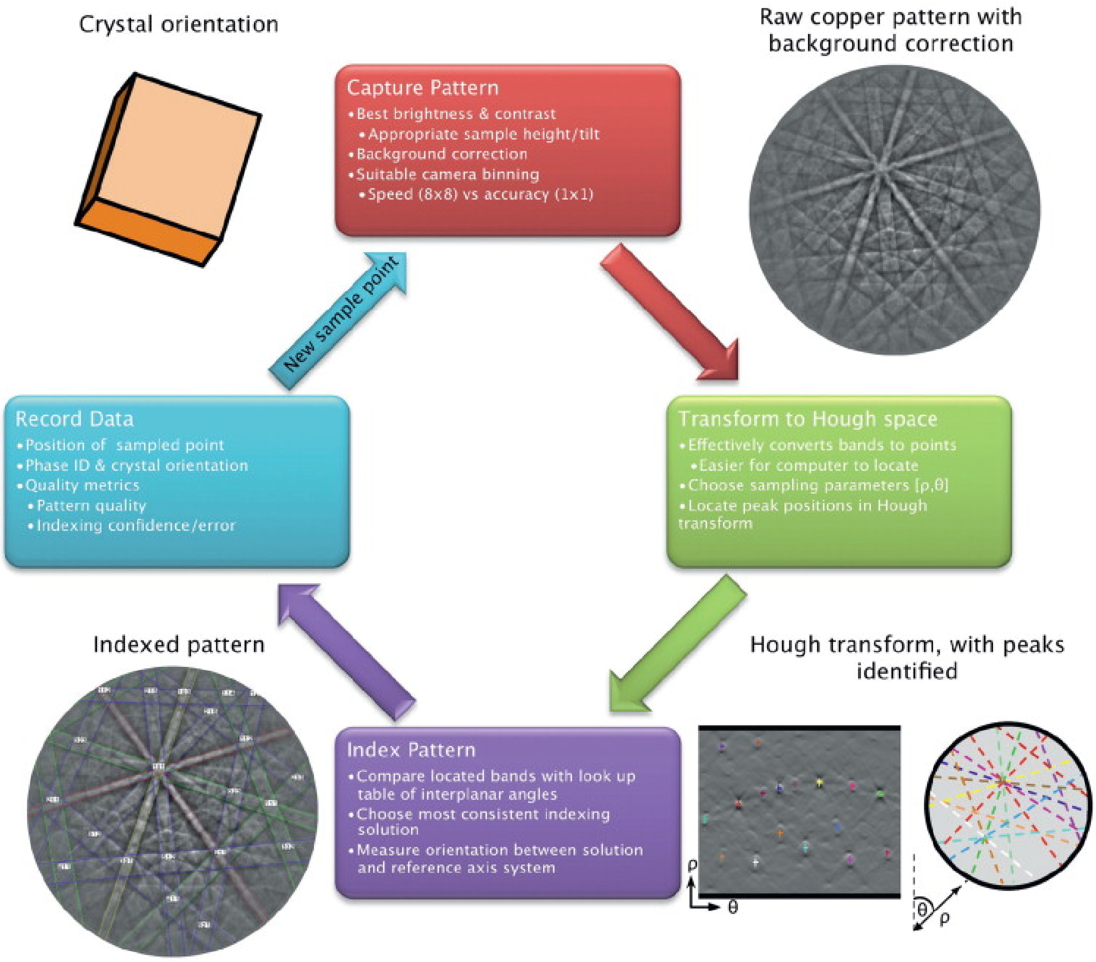

Figure 1.6 Overview of EBSD indexing procedure showing pattern capture through to determination of crystal orientation.[87] (Reprinted with permission from Ref 87. Copyright © 2012 Elsevier.)

1.6 Atomic Force Microscopy (AFM)

AFM has become one of the most versatile scanning probe microscopy (SPM) methods after it was invented in 1986 by Binnig et al. [90] It plays a crucial role in surface morphological characterization at the nanoscale. A schematic diagram of the atomic force microscope is shown in Figure 1.7. The probe in AFM consists of a very sharp tip which is attached to a force-sensing cantilever. When a sample surface is probed by AFM tip, the interaction forces between tip and sample vary as a function of tip-sample separation. The tip first feels a long range attractive force due to Van der Waals interactions, but repulsive forces dominate at closer tip-sample separation distance due to electrostatic interactions, as illustrated in Figure 1.8.[91] In the AFM imaging experiment, the tip scans across the sample surface, and the force between the tip and the sample leads to a deflection of the cantilever. The deflection is measured by the photodiode detector based on the shift in the position of the laser spot reflection on the detector. With the help of a feedback loop in the AFM system to adjust the tip-sample separation for constant height or constant force imaging, the tip follows the contour of the surface, and an AFM map is thus collected.[92-94]

There are usually three principle operation modes in AFM: contact mode, non-contact mode, and tapping mode. An illustration of the three modes is shown in Figure 1.9. In the contact mode, also known as repulsive mode, the tip is in close contact with the sample surface and repulsive interaction forces dominate between the tip and sample. As the tip scans over the surface, the forces will change abruptly since the slope of the interaction force curve is very steep in the contact regime, as shown in Figure 1.8. Accordingly, the deflection of cantilever change can be readily detected and the topographic or morphological change can be cleanly observed. Contact AFM imaging can be performed at either the constant-height or constant-force mode. In constant-height imaging, the cantilever deflection due to tip-sample interaction can be directly used to estimate the surface topography. In constant-force mode, the force between the tip and the sample is kept constant when the tip is scanned across the sample surface. A feedback loop is employed to adjust the position of cantilever to maintain the constant force. The drawbacks of this mode are the effects of friction, adhesion, and shear forces resulting from continuous contact with the sample, which can damage the sample and distort the features of the generated image.[90, 93, 95, 97]

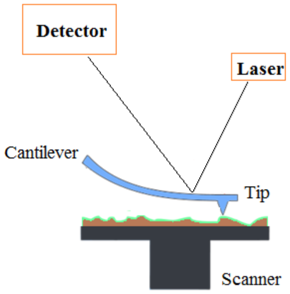

Figure 1.7 Scheme of the atomic force microscope with main components indicated.[93]

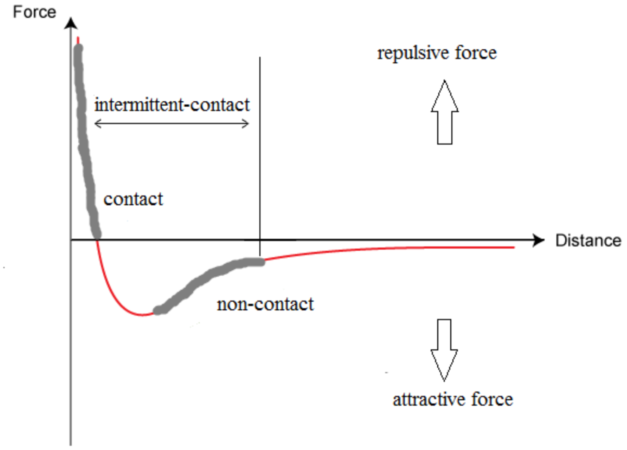

Figure 1.8 AFM interaction force curve as a function of tip and sample separation distance. [95]

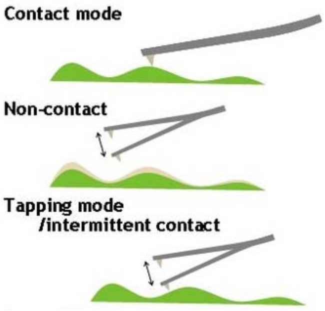

Figure 1.9 An illustration of AFM operation modes.[96]

In non-contact mode, the tip hovers above the sample surface and oscillates above its resonance frequency during the imaging scan. The change in amplitude, phase, or frequency due to the Van der Waals attractive interaction with the sample is detected by the photodetector, and the tip-sample distance is adjusted by a feedback loop to maintain a constant oscillation amplitude. Hence, the surface topography of the sample is plotted as a function of the tip's lateral position. The advantages of this mode mainly lie in imaging soft or elastic samples with little or no contact between the tip and the sample.[95]

The tapping mode, also called intermittent contact mode, combines qualities of both contact mode and non-contact mode in AFM imaging. In this mode, the tip oscillates at or near its natural resonance frequency and taps the surface for a minimal amount of time during the imaging scan. The tapping mode overcomes the difficulties the conventional contact mode has in imaging soft or fragile samples such as proteins and polymers. The tapping mode yields scan images with high resolution, and greatly minimize the possible damages to the surface by the AFM tip. For rigid samples and rough surfaces, both contact and non-contact mode can be employed for AFM imaging. Non-contact mode doesn't damage the sample surface, but the image resolution is relatively low and the imaging process can be hampered by a contaminant layer, which can interfere with oscillation.[90, 95]

Based on the type of interaction between the tip and the sample, physical morphology or topography, charge density, magnetic field, and other surface properties of the sample can be discerned and measured by AFM.[94, 98] In comparison to other optical and electronic microscopes, AFM can not only scan the X and Y direction, but also measures the information in the vertical dimension (Z direction) of the sample properties with comparable or even better magnification than electronic microscopes.[99-101]

1.7 Objectives and Outline of the Research

The focus of this research is to investigate the structure-activity relationship of pseudo-single-crystal electrode of polycrystalline platinum in two types of electrochemical reactions: an electrolytic etching reaction and an electrocatalysis reaction. The major chemical and physical methods and techniques involved in this study include metallurgical electrolytic etching, scanning electrochemical microscopy (SECM), atomic force microscopy (AFM) and electron backscatter diffraction (EBSD).

In Chapter 1, the concept of structure-activity relationship and the microstructure of platinum catalysts are introduced. Previous studies of structure-activity relationship on platinum single crystal electrodes are reviewed. The hydrogen oxidation reaction and study of electrocatalysis of the HOR on Pt catalysts are presented. The operational principles for major characterization techniques including SECM, EBSD, and AFM are described.

In Chapter 2, a metallurgical electrolytic etching method is employed to prepare pseudo-single-crystal platinum electrodes. The effects caused by the composition and concentration of etching solutions, etching time, and the nature of the Pt materials on etching and the quality of the electrode preparation are discussed.

In Chapter 3, physical and chemical properties of pseudo-single-crystal electrodes of polycrystalline platinum are studied by optical microscopy, optical profilometry, SEM, AFM, EBSD, and cyclic voltammetry. The etching rate of the surfaces of Pt pseudo-single-crystal electrodes with different crystallographic orientation in the electrolytic reaction is elucidated based on the characterization results.

In Chapter 4, electrocatalysis of the HOR is studied on platinum single crystallites of a polycrystalline electrode surface. The relationship between the kinetic activity of high-index single crystal platinum electrode surfaces for the hydrogen oxidation reaction and corresponding crystallographic orientation is investigated using SECM imaging techniques coupled with EBSD imaging.

CHAPTER II

SURFACE TREATMENT OF POLYCRYSTALLINE PLATINUM ELECTRODES BY ELECTROLYTIC ETCHING

2.1 Introduction

In order to improve the performance of fuel cells catalysts with enhanced electrocatalysis efficiency, the search for lower-cost and better alternative catalysts for fuel cells have been studied on Pt-based multicomponent catalysts,[49-50] non-platinum metallic combinations,[8-9] transition metal complexes,[12] and metal oxides[15] over the last century. It is reported that the most widely used electrocatalysts for both anodes and cathodes in fuel cells are still Pt and its alloys due to their optimum electrocatalytic behavior.[16, 102-103]

It is well known that many properties of metallic materials are directly and sensitively related to the material's microstructure. For example, the mechanical strength of many metals and alloys depends strongly on the grain size. The chemical and functional characteristics of structure-sensitive materials are dominated by the material composition and surface structure.[1, 104] One route to developing a better Pt catalyst for fuel cells is to develop an understanding of the relationship between the electrocatalytic properties of Pt metal electrodes and its microstructural features, such as grain size and grain orientation.

The study of the structure-activity relationship of Pt metal electrode has been investigated using cyclic voltammetry and rotating disk electrode voltammetry (i.e., RDE and RRDE).[105-106] These methods require the fabrication of Pt single crystal electrodes using expensive single crystal materials and requires careful handling and sophisticated procedures known as Clavilier's method and flame annealing approach.[25] In this study, a simple and distinct approach was developed to produce pseudo-single-crystal surfaces of Pt by adopting an electrolytic etching method for further structure-activity relationship study of the Pt catalyst. Numerous and unique single crystal planes are produced from a polycrystalline platinum electrode in a single step method.

In this chapter, the method used to produce single crystal surfaces from a polycrystalline platinum electrode is described. Optical micrographs of the surface of a polycrystalline Pt electrode are compared before and after the etching procedure. The effects of the etching parameters such as sample pretreatment conditions, etching solution composition and concentration, and etching time are discussed.

2.2 Experimental

2.2.1 Reagents

Hydrochloric acid (37.4%, Fisher Scientific) and sodium chloride (purity > 99%, Research Products International Corp.) were used as received. Deionized water (Nanopure, Barnstead) was used to prepare the etching solution for all experiments.

2.2.2 Electrodes and Apparatus

2.2.2.1 The Pretreatment of Pt Wires

Platinum wire (99.95 %, 500 μm diam) purchased from two different companies

(Alfa-Aesar and World Precision Instruments) were used in the electrode fabrication. The Pt wire bought from Alfa-Aesar is hard annealed, and the other type from World Precision Instruments is not. Two Pt wires supplied by World Precision Instruments were annealed at 800 °C and 1000 °C, respectively, for further etching experiments. The annealing time was 40 minutes at both temperatures. After annealing, the wire was immediately quenched in cold water for 30 min.

2.2.2.2 The Fabrication of Substrate Electrodes

The substrate electrode was prepared with 500 μm diam Pt wire embedded in epoxy resin. The Pt wire was electrically connected to Cu wire with silver epoxy. An insulating rubber tube was used to cover and secure the joint between Pt wire and the Cu 30 gauge wire, and then the two connected wires were positioned vertically in a rubber mold with the platinum electrode facing the bottom of the rubber mold with the Cu wire extending up and out of the mold cavity. The rubber mold was filled with epoxy resin (Epon^{TM} Resin 828) and 8% (by weight) triethylenetetramine (TETA) hardener mixture, left overnight, and cured at 120 °C for 4 h and at 140 °C for 2 h. After curing, the bottom was ground to expose the circular cross section of the platinum substrate wire using successive grits of 240, 400, 800, and 1200 SiC sandpaper. Then, the electrode was fine polished with 15, 5, 3, 1, and 0.05 μm alumina slurries successively on separate polishing cloths. After the final polishing step, a mirror like finish was attained. Water was used as a lubricant to wash away the removed material and keep fresh abrasive surface exposed. Ultrasonic cleaning was employed to completely clean the electrode before changing the abrasives.

The apparatus for the electrolytic etching experiment is shown in Figure 2.1. A Pt substrate electrode worked as the anode and a graphite electrode serves as a counter electrode in the etching procedure. The Pt substrate electrode and the graphite electrode were immersed in the etching solution and 6 V AC voltage was applied between the two electrodes using a variable transformer. The etching solution was prepared with HCl, NaCl, and deionized water with different chemical concentration and volume ratios.

The optical micrographs of the surfaces of polycrystalline Pt substrate electrodes were taken with an optical microscope Olympus BH-2 (Olympus Optical Co.).

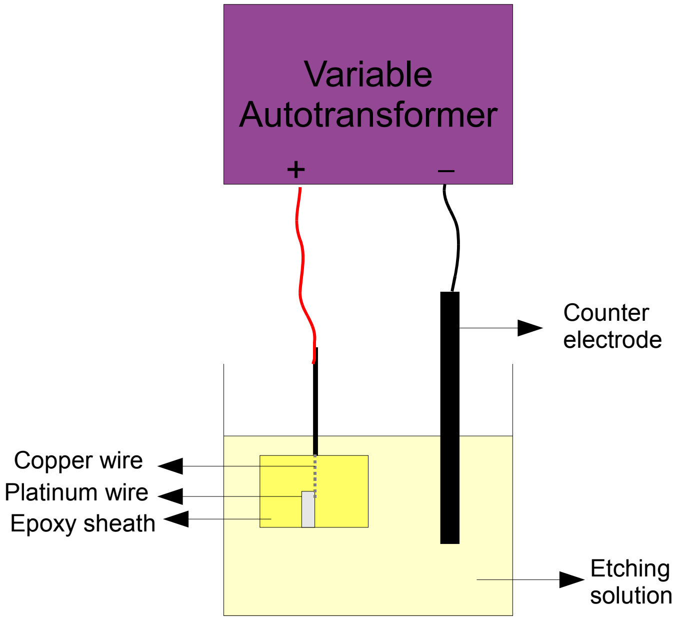

Figure 2.1 Scheme of the experimental set-up for electrolytic etching of Pt electrode in etching solution with graphite electrode as the cathode.

2.3 Results and Discussion

2.3.1 Effects of the Etching Time and the Etching Solution Composition and Concentration

In order to reveal the microstructure of the polycrystalline Pt substrate electrode surface in electrolytic etching experiments, the appropriate etching solution was screened first. Among all the available etchants for platinum and its alloy, saturated NaCl/HCl solution was chosen owing to the best etching results it produced and the facile solution preparation. It is reported that both dilute and concentrated HCl are used in electrolytic etching for platinum.[107-108] In Table 2.1, the compositions of the two etchants are shown.

Table 2.1 Electrolytic etching solution composition for use with Pt electrode

	Composition		
Etching solution	HCl (37%)	NaCl	H_2O
# 1	20 ml	25 g	65 ml
# 2	10 ml	1 g	none

Since time is a very important factor in the etching experiment and it directly affects the microstructure of the surface, a set of experiments were performed to determine the appropriate etching time in etching solution #1.[107] Before the etching procedure, optical micrographs of well polished Pt substrate surfaces were taken. As shown in Figure 2.2, the surface of 500 μm diam polycrystalline Pt substrate electrode (sub #J) was polished to a mirror finish, and no scratches can be seen on the surface.

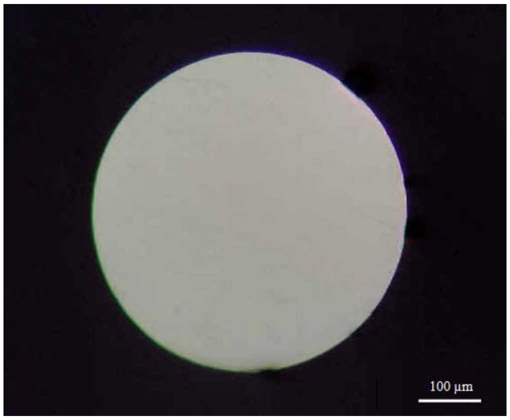

Figure 2.2 Optical micrographs of a polished polycrystalline Pt substrate surface (Sub #J).

After careful examination under the optical microscope to make sure the surface is free of scratches, the electrodes were ready for electrolytic etching.

Photographs of the etched Pt electrode surface (Sub #J) were recorded after every 10 s etching time in the solution. Figure 2.3 shows the selected etched surface images of Pt substrate #J after an etching time of 20 s, 40 s, 60 s, and 80 s in etching solution #1. The photograph of the etched Pt electrode surface (Sub #J) after 20 s etching in the solution is shown in Figure 2.3a. The microstructure of the Pt disk is slightly revealed with a few grain boundaries near the disk edge. Even though some of the grain boundaries are shown, the shape of the grains is not very clear and the grain contrast is very low. As illustrated in Figure 2.3b, after another 20 s etching, more grain boundaries are exposed on the polycrystalline Pt substrate electrode surface than in Figure 2.3a. In Figure 2.3c, most of the crystallites are distinct and distinguishable, and the grain boundaries are readily seen. Besides the grains in the center and the top regions of the Pt disk becoming visible, there is not much change in the overall microstructure of the polycrystalline Pt substrate surface after another 20 s etching as shown in Figure 2.3d. It can be seen that a couple of the grains are relatively large in size and several small grains are close to each other on the polycrystalline Pt surface.

It should be noticed that the edge of the Pt electrode was eroded away, especially the left side of the electrode in Figure 2.3. This causes the Pt disk to no longer have a

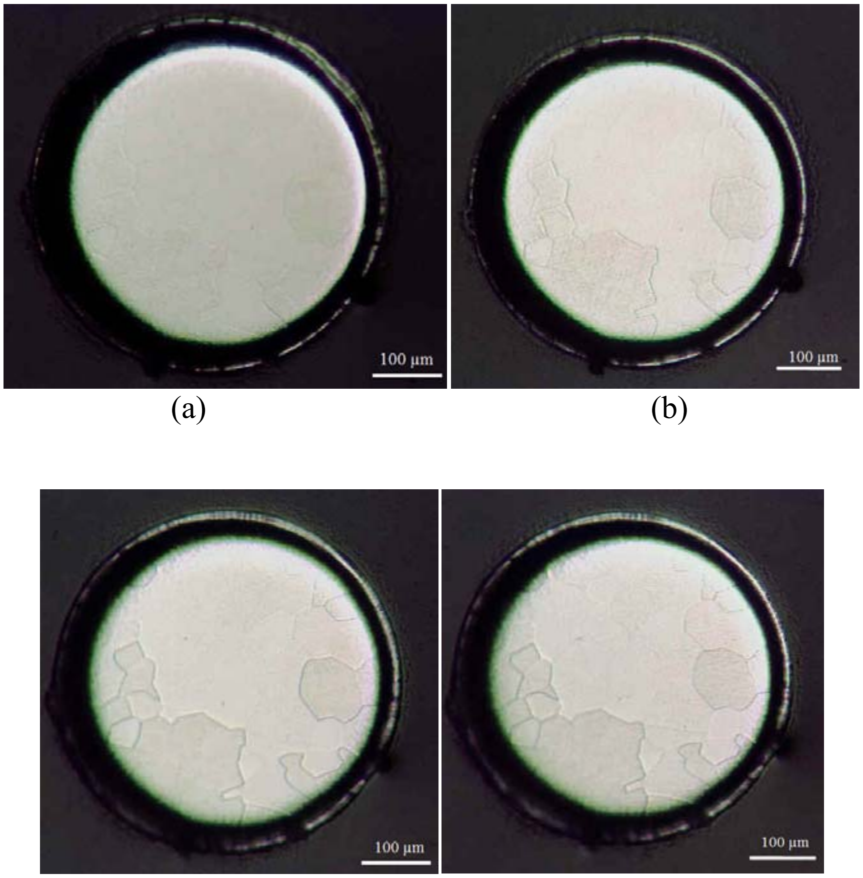

(a) (b)

(c) (d)

Figure 2.3 Optical micrographs of Pt substrate (#J) surface after an etching time of (a) 20 s, (b) 40 s, (c) 60 s, (d) 80 s in the etching solution #1.

perfectly round shape. It is elliptical if viewing the image vertically from top to bottom. A possible reason for the resulting shape of the Pt disk is that the electrical connection between the Pt wire and the Cu connection wire was made on one side of the Pt wire. It is possible the current density is not evenly distributed across the Pt wire due to the assembly as illustrated in Figure 2.1.

The etching experiment was also performed in etching solution #2 which is comprised of only concentrated HCl and NaCl. The Pt disk surface images before and after the etching procedure in solution #2 are shown in Figure 2.4. In Figure 2.4a, the surface of the well polished substrate #E is clean, smooth, and flat. Obtaining an etched surface with well-defined grains as revealed in Figure 2.4b, takes only about 15 s in etching solution #2.

To evaluate the etching effects by the two etching solutions, comparisons were made between the surface images of Pt substrates etched in solution #1 and #2, respectively. Figure 2.5a shows the surface of the Pt substrate electrode #J etched with solution #1, and Figure 2.5b is the etched surface of the polycrystalline Pt substrate electrode #E in etching solution #2. The etching time for achieving well etched surfaces of the Pt substrate electrodes is 80 s for Figure 2.5a, and 15 s for Figure 2.5b. It indicates that the etching efficiency can be greatly enhanced (about 70%) by using etching solution #2. Besides reducing the etching time in solution #2, the Pt disk electrode retained a rounder shape compared to the elliptical shape in solution #1. Moreover, the grains on the etched Pt substrate electrode surface shown in Figure 2.5b are clearly more distinct than the ones in Figure 2.5a. Thus, etching solution #2 is preferred for the etching experiment.

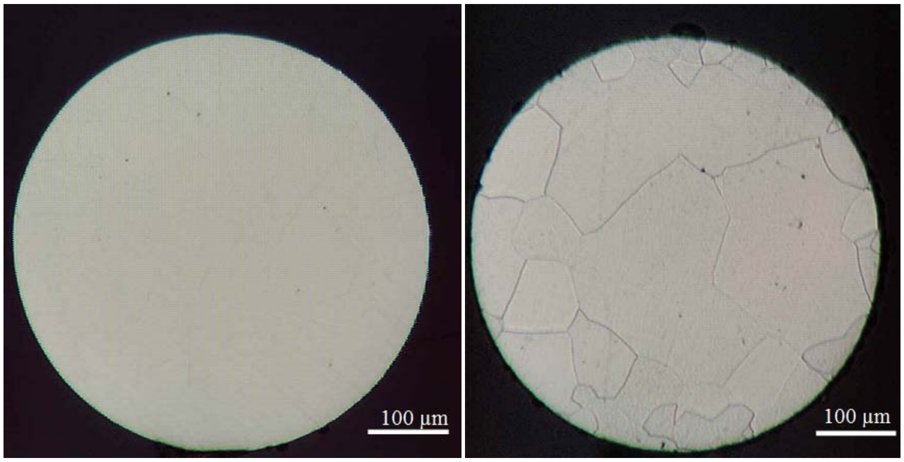

(a) (b)

Figure 2.4 Optical micrographs of the surfaces of polycrystalline Pt substrate electrode (Sub #E) before (a) and after an etching time of 15 s (b) in etching solution #2.

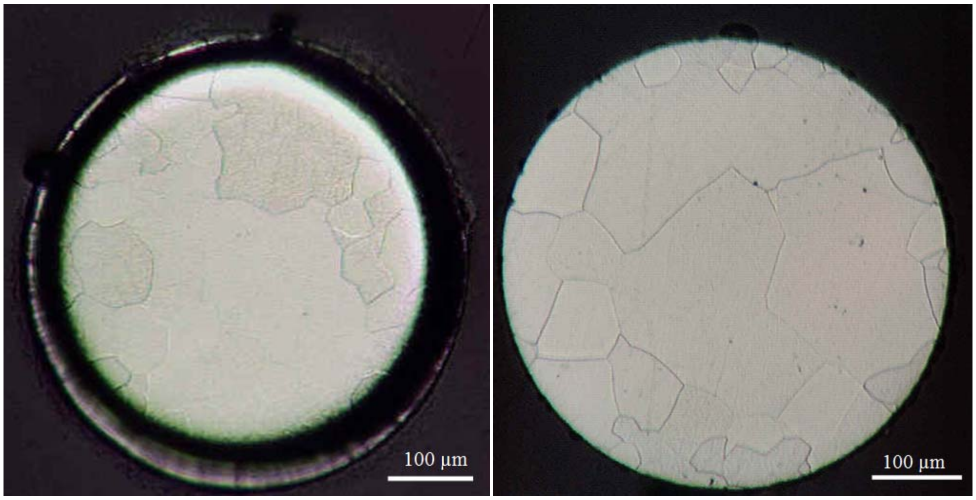

(a) (b)

Figure 2.5 Optical micrographs of the etched surfaces of polycrystalline Pt substrate electrodes. (a) Sub #J, (b) Sub #E.

To have a complete understanding of the effect of etching time on the surface etching result, a longer etching time was applied in the etching experiments in both etchant #1 and #2.

As can be seen from Figure 2.6b, longer etching in solution #1 eroded away the fringe material of the Pt wire and revealed some underlying scratches on the surface of the Pt substrate electrode compared to Figure 2.6a. The optical micrograph in Figure 2.6c shows the peripheral Pt substrate material was severely etched away, leaving a large gap between the remaining Pt disk electrode and the surrounding epoxy. As the etching time increases, the grain boundaries on the surface become more evident. Since grain boundaries are defects in the crystal structure, the erosion is prone to take place at these sites.[109] Though the grain boundaries are deepened by longer etching time, the shape of the grains generally remain the same. Moreover, the appearance of the Pt substrate electrode has slightly changed after 440 s of etching as shown in Figure 2.6c. Pits appeared on certain grains but not on the whole substrate surface, suggesting differences in behavior of various crystalline grains under long etching time conditions.

On the other hand, the results of a poorly polished Pt substrate under a long etching time in etchant #2 are shown in Figure 2.7. Rather than retain the shape and the appearance of the crystallite domains, severe damage can be observed on the substrate surface in Figure 2.7b and c. In Figure 2.7c, the whole surface is almost etched away after 220 s electrolytic etching. The experimental results indicate the etching rate is extremely fast and more homogeneous over the whole polycrystalline Pt electrode surface with solution #2.

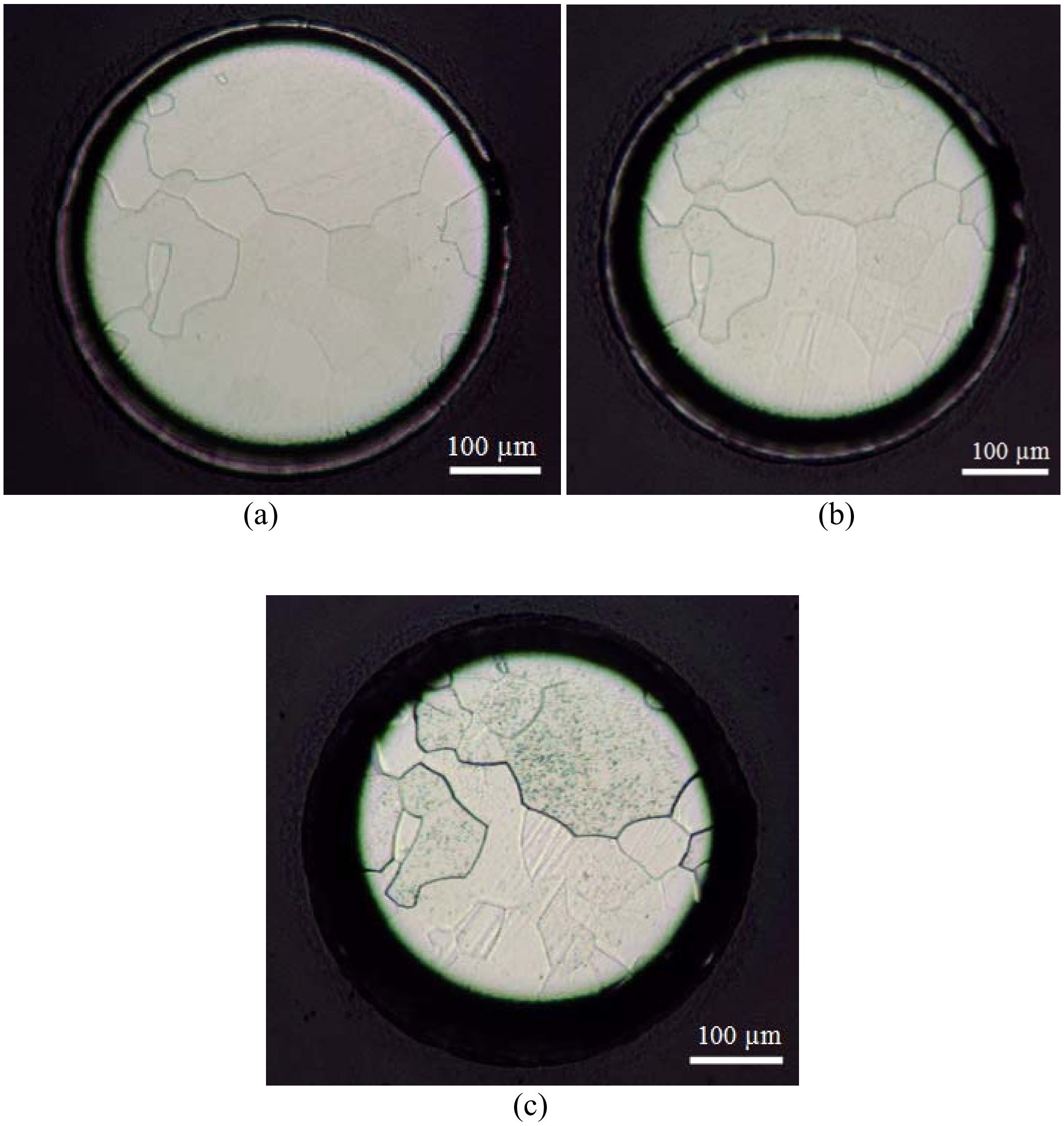

(a) (b)

(c)

Figure 2.6 Optical micrographs of a poorly polished polycrystalline Pt substrate surface after an etching time of (a) 80 s, (b) 140 s, and (c) 440 s in etching solution #1.

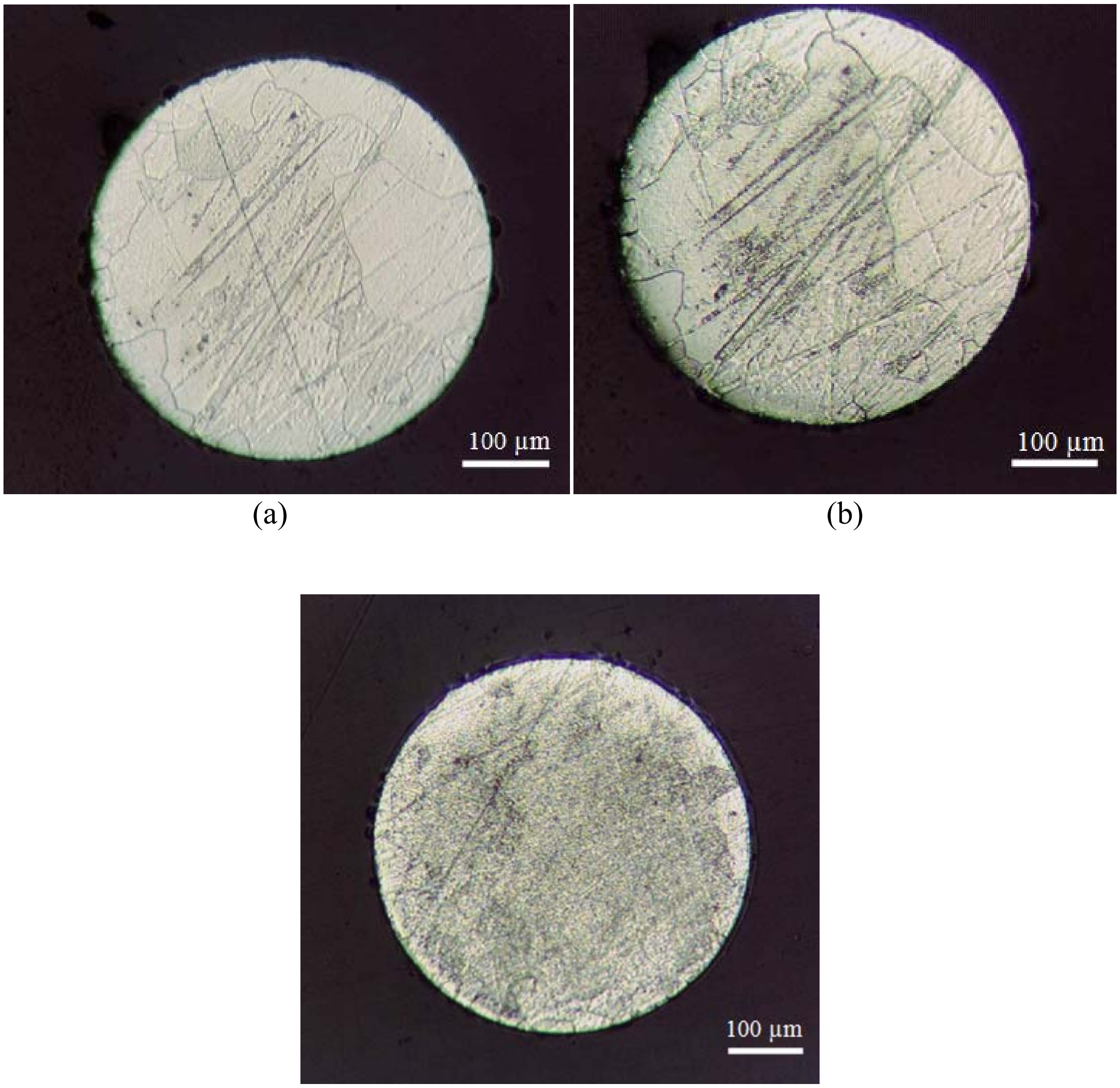

(a) (b)

(c)

Figure 2.7 Optical micrographs of a poorly polished polycrystalline Pt substrate surface after an etching time of (a) 30 s, (b) 90 s, and (c) 220 s in etching solution #2.

Based on the results shown above, the optimum etching conditions are determined to be 15 s etching time in solution #2 and 80 s in solution #1.

2.3.2 Pretreatment of Sample Surfaces

Another type of Pt wire material (unannealed platinum) was used as received in the etching experiments. A Pt substrate electrode made with unannealed platinum wire was polished to a mirror finish in preparation for etching. As illustrated in Figure 2.8, most of the grain boundaries are missing or quite faint. The reasons for the resulting etching feature of the microstructure shown here are possibly due to the crystallographic structure and defects of the polycrystalline Pt materials used.

To prepare different materials for etching experiments and better reveal distinct grain boundaries, heat treatment of the specimen was used before the polishing step. Metal annealing has three stages: recovery, recrystallization, grain growth. By heating a metal above its critical point, maintaining it at a suitable temperature, and cooling or quenching it in a medium, the properties of metal material can be altered.[1, 109]

Since the grain size can be altered by annealing,[1,109] and the effect of metallurgic annealing for platinum is evident at temperature over 900 °C[110], two temperatures (800 °C and 1000 °C) were chosen for the Pt specimen pretreatment experiments. Figure 2.9a shows a photograph of the surface of the etched platinum substrate of Pt substrate #W after annealing at 800 °C for 40 min. The size of the grains (in Figure 2.9a) is slightly increased compared to that of the one shown in Figure 2.8. However, most of the grain boundaries are still faint. The same electrode was repolished and annealed at 1000 °C for 40 min. Then it only took 30 s to achieve the etched surface illustrated in Figure 2.9b in etching solution #1.

Figure 2.8 An optical micrograph of unannealed Pt substrate #W electrode after 75 s electrolytic etching in etching solution #1.

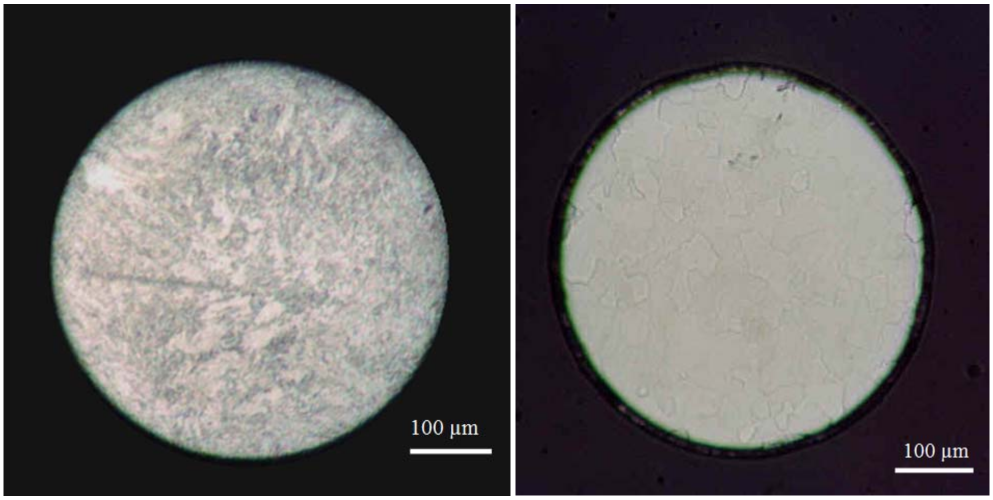

(a) (b)

Figure 2.9 Optical micrographs of the etched surfaces of polycrystalline Pt substrate electrodes #W (100×) in etching solution #2 after annealing at (a) 800 °C, and (b) 1000 °C.

The grain boundaries of the polycrystalline Pt substrate electrode #W etched in etching solution #2 after the annealing at 1000 °C (Figure 2.9b) are very distinguishable and the grain size is apparently the larger than the ones shown in Figure 2.8 and Figure 2.9a, but still smaller than those for Pt substrate #J and #E (Figure 2.5).

It can be clearly seen that the microstructures of the grains of etched polycrystalline Pt substrate electrode #W are different before and after the heat treatment. Without annealing, discrimination cannot be made between grains because the grain boundaries are barely discernable. After Pt substrate electrode #W was annealed at the proper temperature (1000 °C), grain boundaries are distinct and the shape of the crystallites is well defined.

Since Pt substrate #B, #E, and #J were made with annealed Pt wire as received from the manufacturer, no further heat treatment was made to these electrodes. Thus, this heat pretreatment is only applied to the substrate electrode made with unannealed Pt wire.

2.3.3 Mechanism of the Etching Process

The electrochemical etching process is a process which reveals the microstructure of the electrode by selective anodic dissolution in the etching solution. The extent of the reaction is determined by the standard electrode potentials. In addition, the microstructure of the anode such as electrode compositions, phases or orientations also influences the dissolution rates of the electrode material by the etch attack.[22, 107] Thus, electrochemical etching may contrast different microstructural features, and the etching time may vary depending on the conditions of the substrate electrode and etching solutions.

Despite the complexity of the etching process, a mechanism has been proposed for the electrochemical etching of Pt in acidic solution.[107] The etching process at the anode and cathode electrodes is:

- Anodic reaction: The applied potential forces the Pt anode material to undergo oxidative dissolution at the liquid-solid interface;

$$\mathrm{Pt} \rightarrow \mathrm{Pt^{2+}} + 2\mathrm{e^-} \tag{2.1}$$

- Cathodic reaction: The applied potential causes hydrogen evolution in acidic solution.

$$2\mathrm{H^+} + 2\mathrm{e^-} \rightarrow \mathrm{H_2} \tag{2.2}$$

The Pt ion discharged from the polycrystalline Pt substrate surface can combine with Cl^- in the etching solution to form $[PtCl_6]^{4-}$ or $[PtCl_6]^{2-}$ complex ions in the following pathways:[22,111-113]

$$4\mathrm{Cl^-} + \mathrm{Pt} \rightarrow [\mathrm{PtCl_4}]^{2-} + 2\mathrm{e^-} \tag{2.3}$$

$$6\mathrm{Cl^-} + \mathrm{Pt} \rightarrow [\mathrm{PtCl_6}]^{2-} + 4\mathrm{e^-} \tag{2.4}$$

In the solution, the oxygen absorption and oxide film formation at the electrode surface will inhibit the electrochemical reaction by blocking the active sites of the electrode crystal lattice. Therefore, AC current is used to overcome this effect by applying alternating current between anodic and cathodic electrolytic processes.[113-114] Moreover, gas bubbles possibly from hydrogen and chloride evolution can be observed at both the Pt and carbon electrodes.[112-113]

2.4 Conclusions

In this chapter, an electrochemical method to reveal Pt single crystal surfaces has been introduced. The Pt single crystal grains on the polycrystalline platinum electrode could serve as Pt pseudo-single-crystal electrodes for further structure-activity relationship study which will be demonstrated in the following chapters.

The polycrystalline platinum electrode was prepared by embedding the Pt wire in an epoxy cylindrical sheath. It has been successfully demonstrated that single-crystal domains can be produced by electrolytic etching the surface of a polycrystalline platinum electrode in a very convenient way. Compared with the fabrication process of single-crystal electrodes which requires expensive single-crystal materials and careful handling, this preparation method is relatively simple and inexpensive. In addition, the methods used to prepare single-crystal electrodes are sophisticated, and only a single surface orientation is prepared each time.[25] Using the electrolytic etching method described in this chapter, multiple single-crystal domains are produced in a single etching experiment which greatly enhanced the efficiency in electrode preparation.

The work in this chapter shows that the electrolytic etching time closely depends on the composition and concentration of the etching solution, and the conditions of the electrode. Etching solution #2, which is comprised of concentrated HCl and NaCl, exhibits high etching efficiency with short etching time. Moreover, the resulting etched surface of the Pt electrode in solution #2 was free from edge erosion. Therefore, etching solution #2 is preferred in etching experiments. The appropriate etching time is determined in both etching solutions: it only takes 15 s to achieve an etched electrode surface with well-defined grain structures in solution #2, while 80 s is required in solution #1. Slight discrepancies may be noted in deciding the proper etching time for different Pt electrodes based on the actual electrode conditions. It has also been demonstrated in this study that etching times longer than optimum will result in the exposure of underlying mechanical polishing traces/scratches. In the worst case, excessive etching will erode away the whole flat and smooth surface, causing severe damage to the microstructure of the Pt electrode surface.

The applicability of the electrolytic etching approach has been tested on a substrate electrode made with another type of Pt material, which is unannealed Pt wire. A comparison between the etching results for electrodes made with original unannealed Pt material and annealed Pt wire after heat treatment was made and shows that the heat treatment can effectively alter the microstructure of the Pt material. The grain boundaries become distinct and the grains are distinguishable after annealing the original Pt wire at 1000 °C.

The mechanism of the etching process is proposed as Pt electrode undergoes dissolution at the anode and hydrogen evolution is driven at the cathode. The Pt ion exists in the form of $[PtCl_6]^{2-}$ and $[PtCl_6]^{4-}$complex in the etching solution. Both hydrogen and chloride evolution are the possible reactions for gas bubble formation.

The resulting microstructural contrast displayed on the etched Pt electrode surface is most likely due to the different microstructure differences in crystallographic orientation. Physical and chemical characterization of the single crystal electrodes produced by the electrolytic etching method demonstrated in this chapter will be the subject of the next chapter.

CHAPTER III

SURFACE CHARACTERIZATION OF POLYCRYSTALLINE PLATINUM ELECTRODES

3.1 Introduction

Chapter 2 introduced a convenient and effective method of revealing single crystal domains on a polycrystalline Pt electrode by a metallurgical electrolytic etching approach. The smooth, flat, and scratch-free surface of the polycrystalline Pt substrate electrode was etched to expose the underlying well-defined single crystal microstructure. Individual grains can serve as pseudo-single-crystal electrodes in the structure-activity relationship study for different electrochemical reactions.

In order to develop an understanding of the influence of the surface structure on the electrochemical properties of the polycrystalline Pt substrate electrode and elucidate the correlation between the surface structure (in particular, the crystallographic orientation) and the electrochemical activity of platinum (etching rate in this case) in the electrolytic etching process, chemical, and physical methods are used to characterize the microstructural features of the polycrystalline Pt electrode surface. The techniques employed to perform the surface characterization include cyclic voltammetry, optical microscopy, optical profilometry, atomic force microscopy (AFM), scanning electron microscopy (SEM), and electron backscatter diffraction (EBSD).

Optical microscopy is the basic technique used to examine the polycrystalline platinum electrode surface and discern the grain boundaries between crystallites. Because of the limited resolution of optical microscopy, SEM was employed to obtain images with high magnification and also provide a general overview of the surface topographic differences. Optical profilometry and AFM were used to measure the surface roughness and height differences among different single crystal domains to estimate their corresponding etching rate. The crystallographic orientation of the exposed grains was investigated by EBSD.

3.2 Experimental

3.2.1 Electrodes

Substrate electrodes were prepared by the procedure described in Chapter 2. Surface activation was performed by cycling the electrode between −0.8 V and +0.8 V versus Hg/Hg_2SO_4 reference electrode (referred as MSE in the following) in 1 M H_2SO_4 solution at a scan rate of 100 mV/s with a BAS 100 B/W electrochemical workstation (BAS, West Lafayette, IN).

3.3 Apparatus and Method

Surfaces of polycrystalline Pt substrate were visually examined with an optical microscope Olympus BH-2 (Olympus Optical Co.) at 100× and 500× magnification.

Atomic force microscopy (AFM) experiments were carried out on a Dimension Icon AFM instrument (Bruker). ScanAsyst mode was employed for topographic characterization o the polycrystalline Pt substrate surface. The tip used in AFM scans was a commercial NCHV model with a normal spring constant of 42 N/m at a resonance frequency of about 320 kHz (Bruker).

The step height of the surface was determined by optical profilometer (WYKO NT1100 optical profiling system) with vertical shift interference (VSI) mode.

For SEM analysis, the Pt substrate electrode was glued onto a flat metal disk, and covered all over except the Pt disk area with silver paint (SPI supplies, West Chester, PA). A small amount of graphite conductive paint or carbon tape was used to make the electrical connection between the substrate electrode and the mounting disk. The FE-SEM images were collected with a Zeiss Supra 40 field-emission-gun scanning electron microscope. The operating voltage was 10 kV, and the working distance was 9 mm.

Electron backscattering diffraction (EBSD) scanning was conducted to obtain crystallographic orientation information on the polycrystalline Pt substrate. EBSD scan images were taken with an EDAX Hikari EBSD detection system connected to the Zeiss Supra 40 FE-SEM. Indexing of diffraction patterns and data processing were done using TSL OIM Analysis software (AMETEK).

3.4 Results and Discussion

3.4.1 Surface Characterization by Optical Microscopy and Scanning Electron Microscopy (SEM)

Optical microscopy has been demonstrated to be a useful technique to evaluate the effect of certain parameters, such as etching time and the concentration of the etching solution, on the microstructure of the polycrystalline electrode in the etching procedure as illustrated in Chapter 2. A number of optical micrographs of the well-polished and etched surfaces of the Pt substrate electrode are shown in Chapter 2.

The photograph of the whole surface of the polycrystalline Pt disk (substrate #J) electrode after 80 s etching in etching solution #1 is shown in Figure 3.1a. Even though most of the grains are revealed on the optical micrograph, the grains are not easily distinguished from one another. Two possible ways to resolve this problem are to etch the surface for a longer time, or to use a higher optical magnification. Since the edge of the Pt electrode has already been eroded away after 80 s etching in etchant #1, a longer etching time would result in more erosion of the edge and deeper exposure of underlying scratches beneath the top layer of the electrode surface. Moreover, it is better to retain the well etched surface of the Pt electrode and protect it from surface damage for other characterization and future use. Thus, longer etching time is not an ideal option for this purpose. On the other hand, a high magnification would be a very convenient way to examine the surface microstructure.

The image shown in Figure 3.1b is the square region marked (inside the blue line) in Figure 3.1a at a 5× higher magnification. Individual Pt grain surfaces in Figure 3.1b can be easily discerned. However, the whole surface cannot be completely displayed at 500× magnification due to the capability limitation of the optical microscope used. In addition, it was noticed that good focus could not be obtained over the imaged region. This is attributed to the different depths of field in optical microscopy due to a difference in vertical height resulted from the uneven surface after etching.

Even though discrimination of single crystalline domains was achieved, comparison of step height among grains across the surface could not be made due to the differences in depth of field across the surface. Scanning electron microscopy, an imaging technique

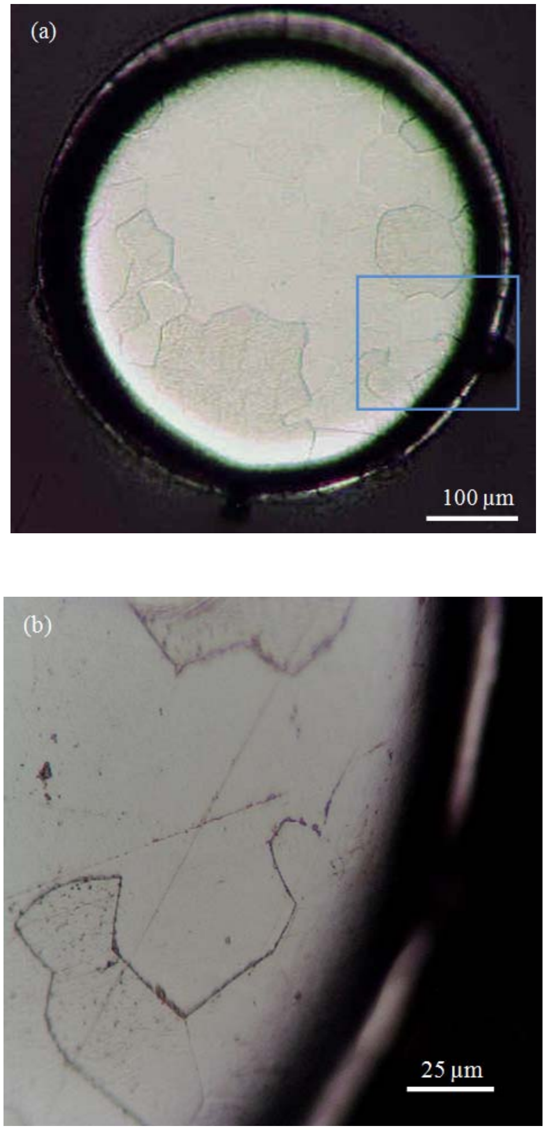

Figure 3.1 Optical micrographs of the etched surfaces of the polycrystalline Pt substrate electrode (substrate #J) after an etching time of 80 s in etching solution #1 at (a) 100×, (b) 500× magnification.

with higher resolution and larger depth of field, is utilized in an attempt to overcome this limitation and exhibit the whole surface at an appropriate magnification.

Figure 3.2 shows the image of polycrystalline Pt substrate electrode #J taken with SEM. Different grains can be effortlessly identified and distinguished from one another based on gray-level color contrast. Compared to the optical micrographs shown in Figure 3.1, the SEM micrograph displays a significantly clearer and less blurred surface owing to its capability of achieving a large depth of focus. In the high magnification SEM image (459×), details of the grain structures can be seen clearly. For example, the grains near the center and top region of the Pt disk electrode surface that cannot be easily discerned by the optical microscope (as shown in the Figure 3.1), are clearly shown in the SEM image. Moreover, topographic contrasts are observed in the image, as indicated with blue and yellow circles, respectively. The grain marked with the yellow circle is apparently recessed compared to the neighboring grain with the blue circle on the surface. There are also other contiguous grains with clear topographic differences shown in the image. Even though certain contiguous grains seem to exhibit no noticeable topographic differences, such as the grains marked with red square and green squares, respectively, they can be differentiated from the color contrast in the SEM micrograph.

3.4.2 Surface Characterization by AFM and Optical Profilometry

Figure 3.3 shows video captures from the AFM video system of the surface of the polycrystalline Pt substrate electrode #J at different focus planes. Even though the images shown here are clearer than the optical micrographs shown in Figure 3.1, it’s very hard to tell which image is at the proper focus to reflect the true topographic information, and it’s very likely that one of the images is incorrectly focused. Note that features appear alternately protruding or recessed depending on the focus. This same problem occurs when taking photographs with the optical microscope. The SEM image does reveal most of the grain boundaries and topographic information of the crystallites, such as protruding or recessed features resulted from the electrolytic etching procedure However, there are still certain regions in the SEM image which do not show noticeable grain boundaries. An advantage of AFM is that its resolution in Z direction is usually higher than horizontal X-Y planes and can provide more detailed topographic information of the sample surface. As mentioned in Chapter 1, there are generally three operation modes in AFM: contact, non-contact, and tapping mode. The advantages and disadvantages of the three modes were described earlier.

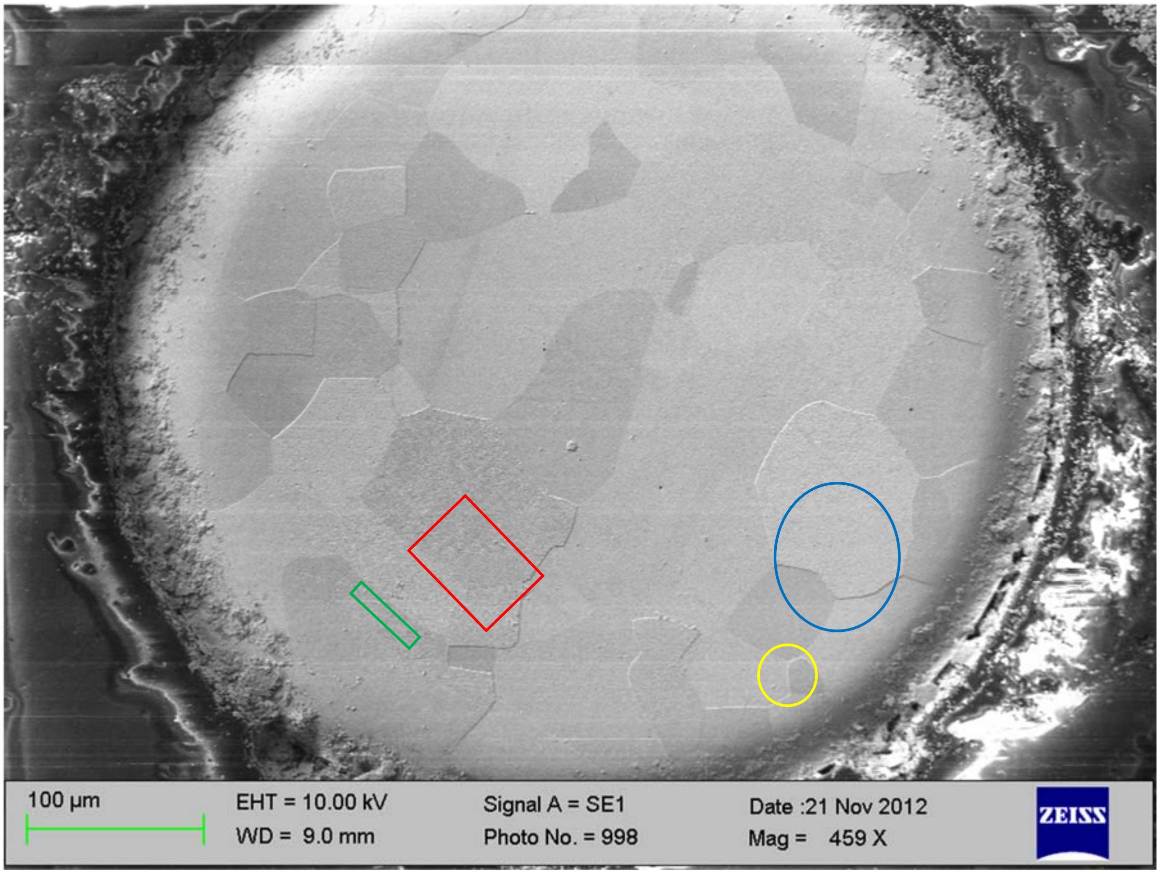

Figure 3.2 SEM image of the surface of etched polycrystalline Pt substrate electrode # J with topographic differences (indicated with blue and yellow circles), and crystallites' microstructure differences (indicated with red and green squares).

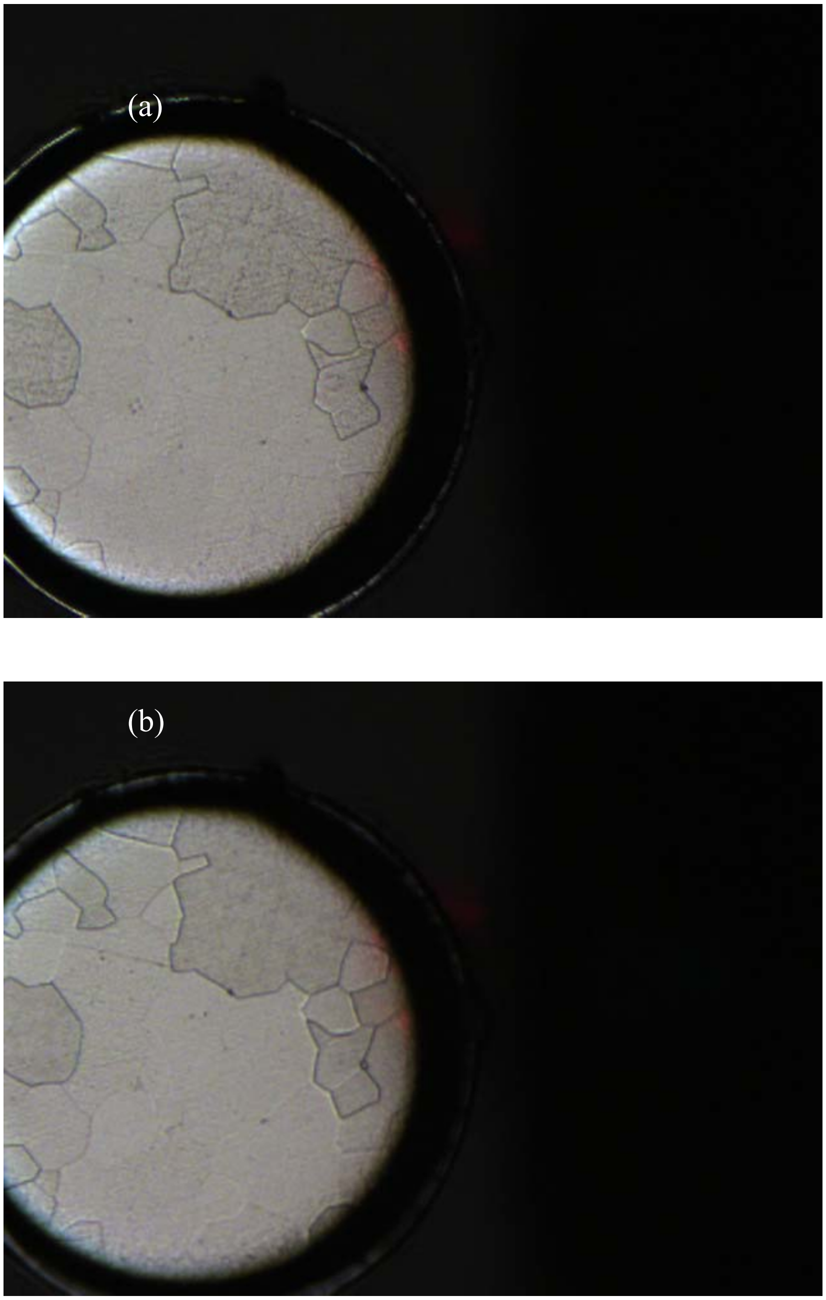

Figure 3.3 Video captures of polycrystalline Pt substrate electrode #J from the AFM video system with different depths of field.

Bruker has a proprietary image optimization mode (called ScanAsyst) based on Veeco’s peak-force tapping mode. In this mode, a fast force curve is performed at every pixel in the image, and the recorded peak force is used in the feedback loop to adjust the tip position over the sample surface. The advantages of this mode are that it can operate the scan at even lower force than required in the tapping mode, the ScanAsyst imaging mode is employed to characterize the surface topography of polycrystalline Pt substrate electrodes and obtain information concerning its surface roughness, step height differences, and three-dimensional topographic information at a nanometer scale.

Figure 3.4 highlights the surface regions that were scanned by AFM with colored squares on an optical micrograph. The corresponding 2D and 3D AFM height images of the scanned surface regions of polycrystalline Pt substrate electrode #J are shown in Figure 3.5. The area scanned in the AFM images shown in Figure 3.5 is 90 µm × 90 µm, which is the maximum scan area allowed with this AFM instrument, except for Figure 3.5c, which is 50 µm × 50 µm. The scale bar displays the height information with color contrast, where the pink color stands for the highest point in the image, and dark brown for the lowest point. In general, the height differences among the grains on the polycrystalline Pt substrate surface range from a few tens of nm to a couple of µm as illustrated by the colored scale bar in Figure 3.5. The areas highlighted by orange and blue squares in Figure 3.4 correspond to regions a and b in Figure 3.5. In Figures 3.5a and b, the overall height scale is within 100 nm as indicated by the scale. The Rq (root mean square roughness) of this image is 26.2 nm as calculated by the NanoScope analysis software. The two 2D AFM images reveal that the height differences between the grains in these two regions are less than 100 nm, which demonstrates the scanned regions on the surface are very flat and smooth. It also explains the reason for the difficulty in discriminating these topographic features by optical microscope: the smooth surface will cause the incident light in the optical microscope to be uniformly reflected, and the small differences in reflectivity cannot be recognized by human eyes. The two 2D AFM images clearly display the Pt substrate's surface topographic characteristics and are superior to optical micrographs and SEM images owing to its high vertical resolution. The 3D AFM images of regions a and b (in Figure 3.5) seem like noisy, rough surfaces. This is possibly due to the small differences in height across the two imaged regions.

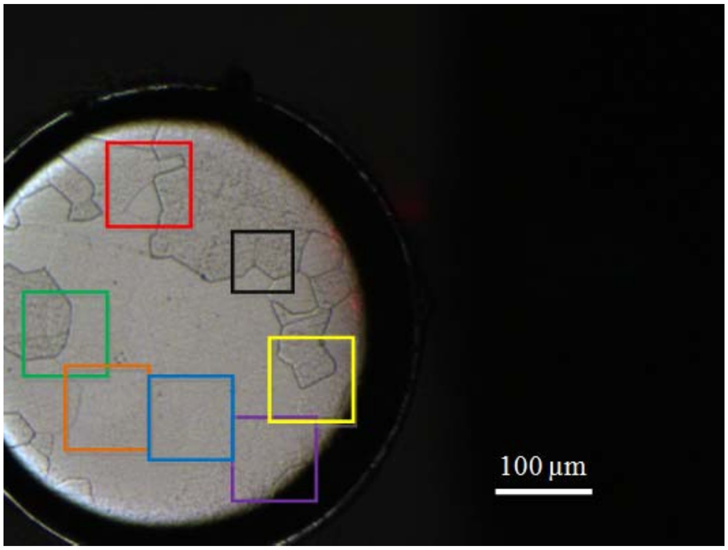

Figure 3.4 Optical micrograph of the surface of etched polycrystalline Pt substrate electrode #J.

Note: The squares correspond to the regions scanned by AFM as shown in Figure 3.5 are marked by the following colored squares: (a) orange, (b) blue, (c) green, (d) black, (e) red, (f) yellow, (g) purple.

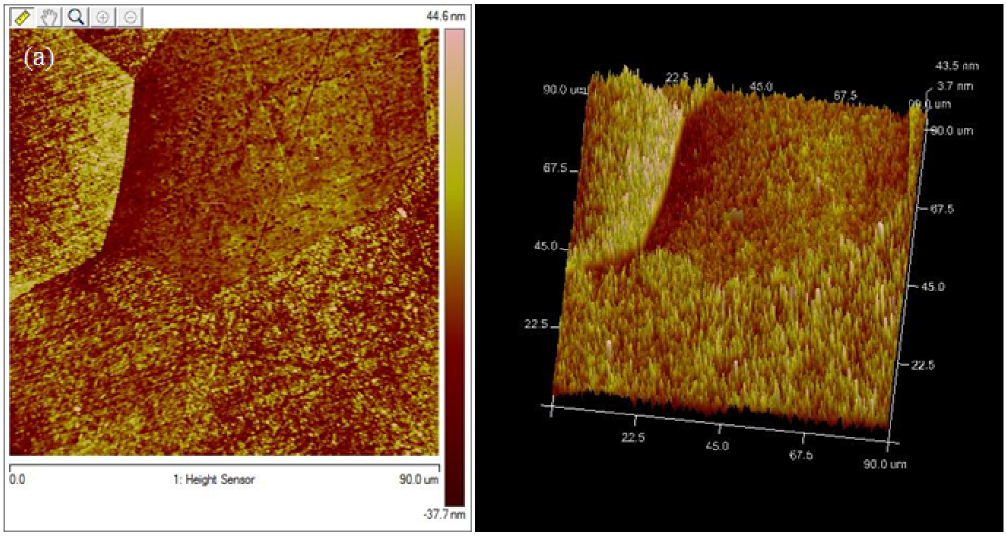

Figure 3.5 2D (left) and 3D (right) AFM height images of the surface regions of Pt Sub #J marked by colored squares in Figure 3.4.

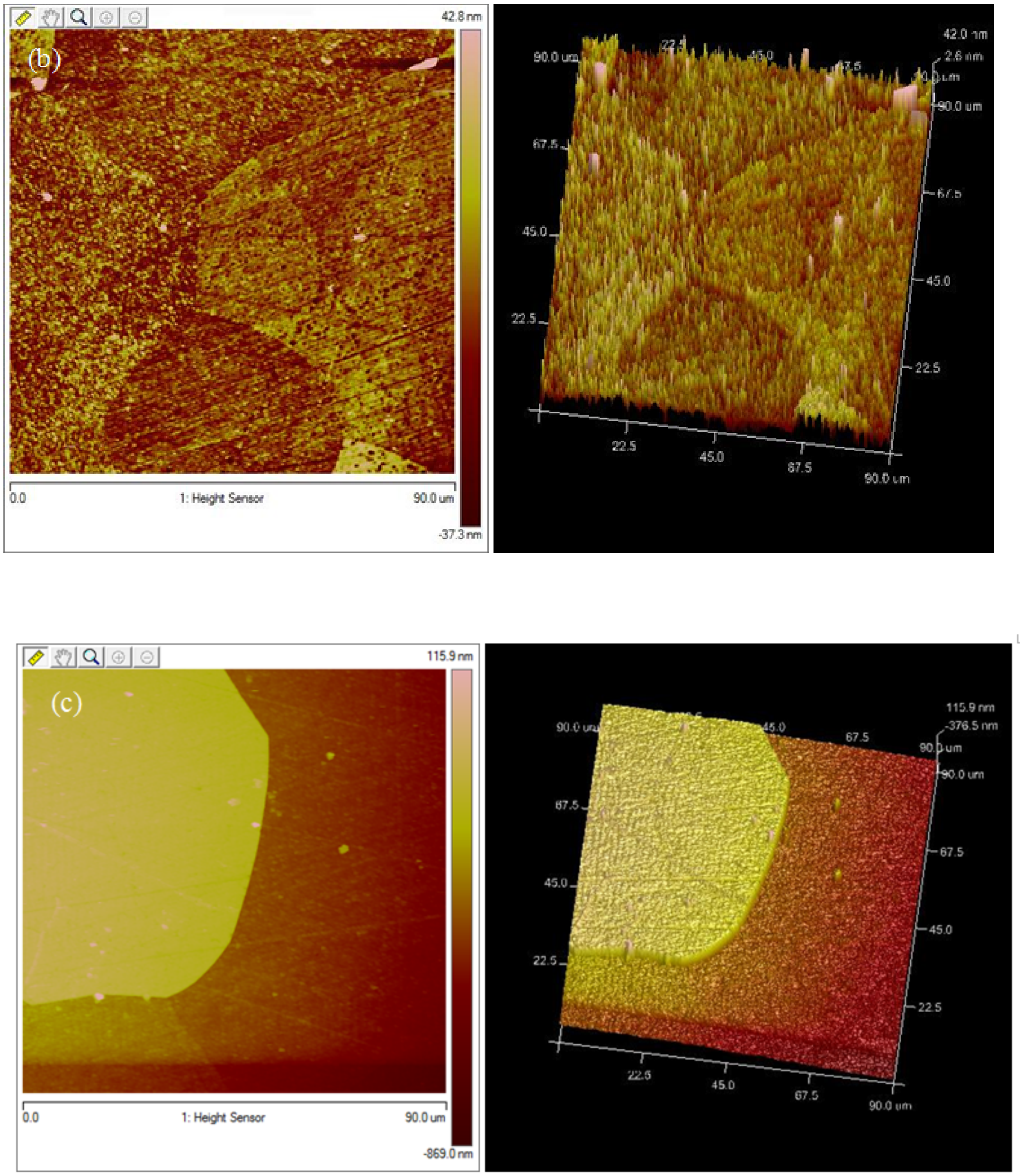

Figure 3.5 Continued

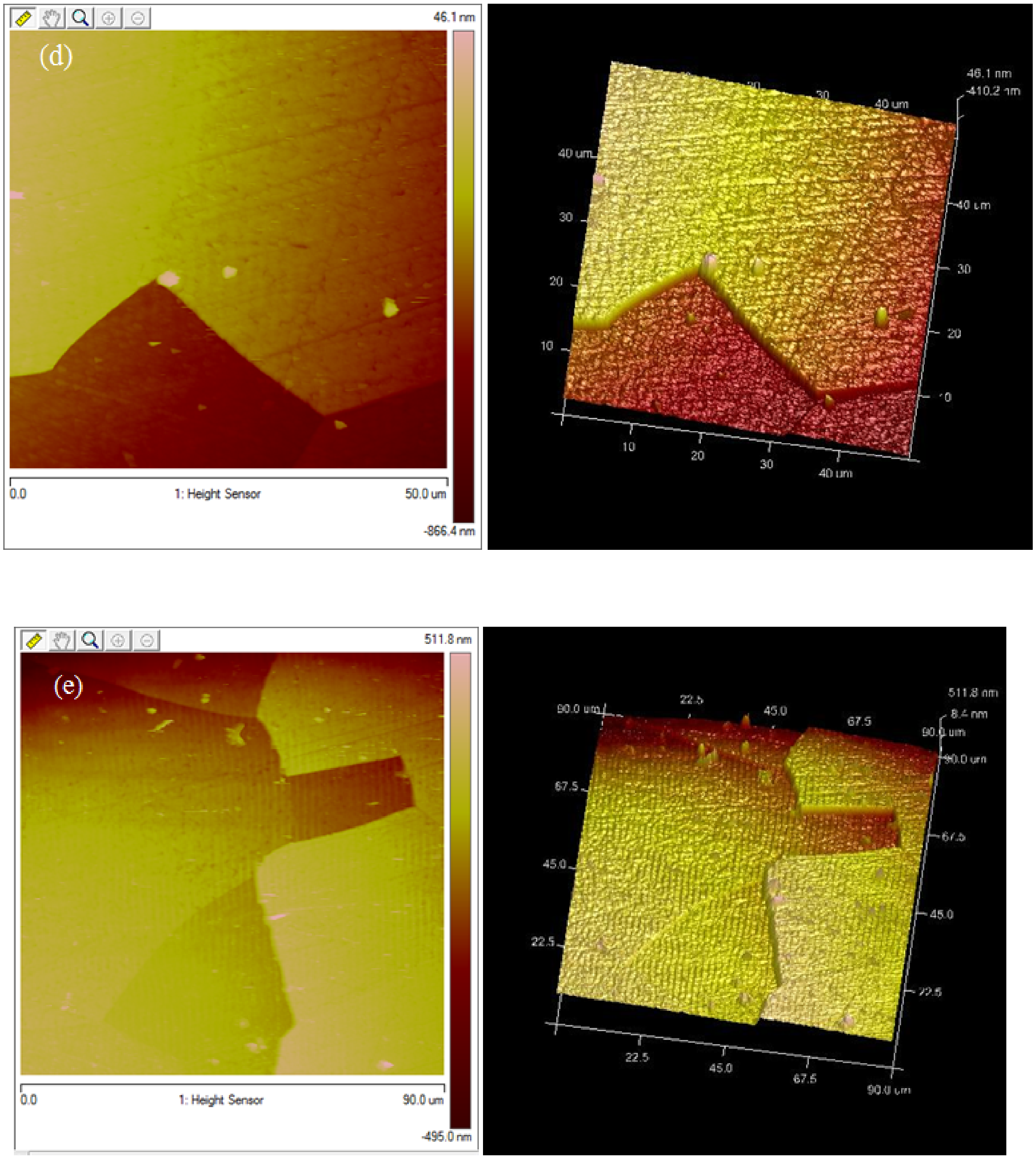

Figure 3.5 Continued

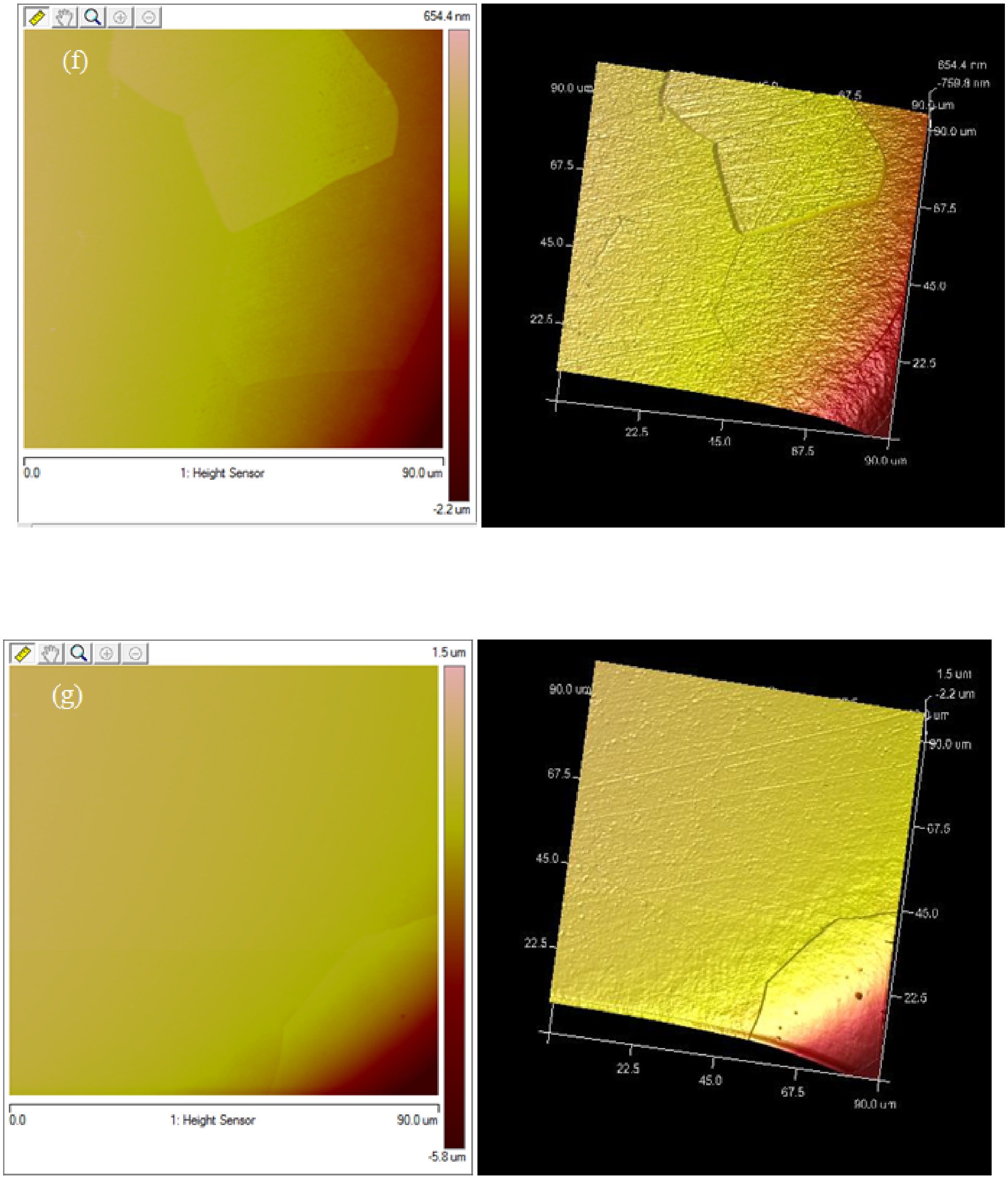

Figure 3.5 Continued

Figures 3.5c and d are AFM images of the regions marked by black and green squares in Figure 3.4. The topographic features are clearly apparent in the AFM height images, especially in the 3D images. The protruding grains are emphasized by a yellow color, and the relatively recessed grains are in brown. The overall surface height variation in Figures 3.5c and d is less than 1 μm, which is larger than in Figures 3.5a and b. The grains inside the black and green squares exhibit distinct topographic differences compared with the ones in the orange and blue squares. By comparing AFM height images (Figures 3.5a, b, c, and d), it can be found that the grain size varies. The grains in Figures 3.5a and b are smaller than the ones in Figures 3.5c and d. Figures 3.5e, f, and g are AFM height images close to the edge of the polycrystalline Pt disk. Figure 3.5e shows the scanned region near the top margin of the whole Pt disk (marked by the red square in Figure 3.4), and Figures 3.5f and g show the ones in the vicinity of the bottom right edge of the Pt substrate electrode (the area inside the yellow and purple squares in Figure 3.5). It can be seen in both the optical micrograph (Figure 3.4 red square area) and AFM height image (Figure 3.5e) that the region comprises several grains. It is worth noticing that the AFM height image in Figure 3.5 reveals that certain grains are not completely flat. For example, the upper right side of the cowbell shaped grain is recessed as shown in Figure 3.5e according to the colored legend. While, the left side of this grain is slightly protruding since it is color coded in yellow. However, all these details cannot be discerned in the optical micrograph shown in Figure 3.4. The reason for the slight height difference within one grain may be because the upper part of the grain is close to the disk edge where the peripheral grains are deeply etched away. In Figure 3.5f, the image shows the grains located near the top of the image are the ones higher in height than the ones in the surrounding area of the image. The region color coded in red brown at the right bottom of the image is the lowest area in the image (Figure 3.5f), which is depressed approximately 2.2 μm compared to the other regions. As the scan approaches the surface edge, the height variation is more obvious as indicated by the color in the 2D AFM image, and the actual topography is clearly represented by the 3D AFM height image. The polycrystalline Pt electrode surface inside the purple square in Figure 3.4 shows only one clear grain in the image with no obviously discernible grains in other parts of the area. The right bottom area in Figure 3.5g is deeply recessed as depicted in the 3D AFM image. The depression of this region is about 5.8 μm compared to the surroundings as indicated by the colored legend. By comparing the purple and yellow regions marked in the optical micrograph in Figure 3.4, it is clear that the purple region contains more of the recessed gap between the Pt disk and the resin sheath than the area marked by the yellow square. This explains the larger depression depth detected in Figure 3.5g than the one found in Figure 3.5f.

In order to have a clearer idea of the surface topography and examine the degree of height change between the crystallites, AFM line profile analysis is employed. Line profile information was collected at three representative places on the polycrystalline Pt electrode surface, and is shown in Figures 3.6, 3.7, and 3.8. The white line in Figure 3.6a emphasizes the place where the profile line is drawn. The two blue crosses highlighted in the AFM height image correspond to the two perpendicular dashed lines in Figure 3.6b. In Figure 3.6a, the overall height variation is estimated to be about 80 nm based on the color scale change. Using the AFM line profile, the height difference at the grain boundary (near the left blue cross) is near 40 nm as shown in Figure 3.6b. At the other blue cross, the depth of the surface scratch is about 30 nm. As can be seen in Figure 3.6, the line profile drawn in Figure 3.6a shows height variation within one grain is very small (ca. 20 nm), which is consistent with the image Rq (26.2 nm) calculated from the roughness analysis. In addition, the line profile shows that the surface of a single grain has a very small height variation. The left grain crossed by the line shows a slight surface tilt: the surface near the grain boundary is slightly protruding, as shown in Figure 3.6b. The line profile also indicates the other grain is relatively recessed especially the region near the grain boundary.

The AFM height line profile shows the step depth between the two grains is approximate 250 nm at the place marked by the blue cross in the center of the AFM image in Figure 3.7. The entire large grain on the left of the image is apparently protruding with a slight tilt. In Figure 3.8, the height variation is very large, and the whole surface is tilted. Nevertheless, it still can be distinguished that the step depth near the grain boundary is around 200 nm. The surface tilt shown in Figure 3.8 could be mainly due to the etching result, which is the Pt disk edge is greatly etched away and recessed.

Overall, the AFM characterization of the etched polycrystalline surface provides accurate and detailed surface topographic information at a nanometer scale. Compared with optical micrograph and SEM images, the height differences are very distinct and clear in 2D and 3D AFM images. The AFM height line profile is employed to obtain the absolute step depth near the grain boundaries. All the AFM results will be further used in conjunction with other surface characterization for application to Pt single crystal etching rate comparison.

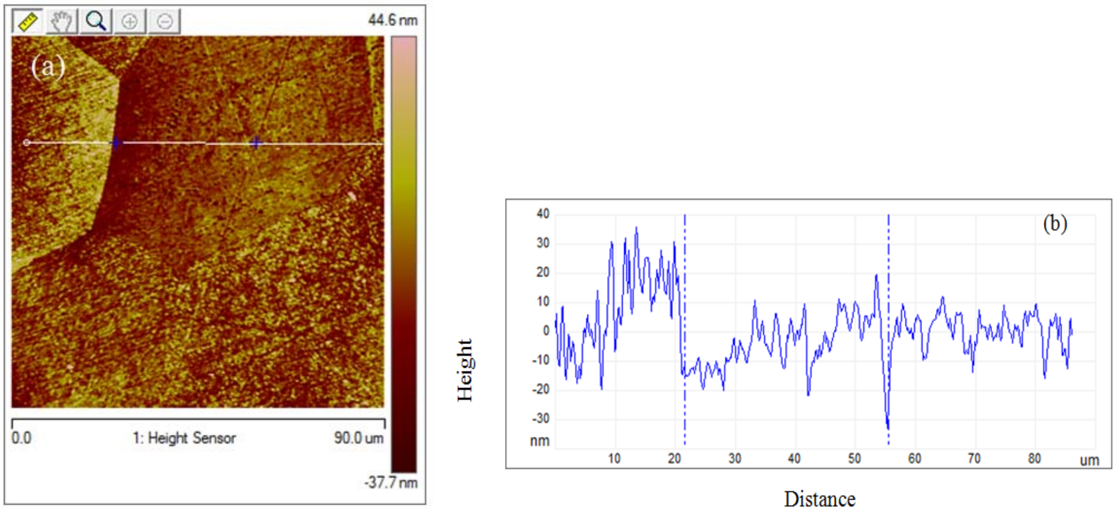

Figure 3.6 AFM height image (a) of the area marked by an orange square in Figure 3.5 and height line profile (b) across the surface.

Note: The two dashed lines in (b) correspond to the two blue crosses in (a).

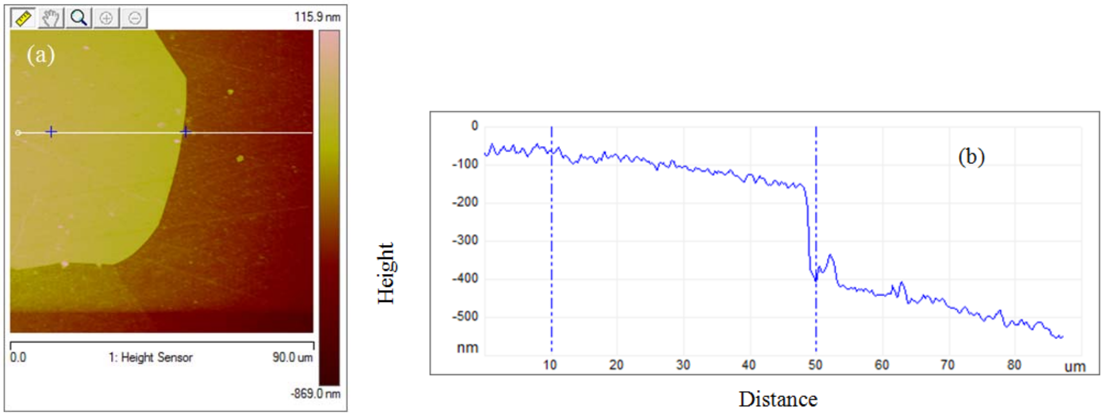

Figure 3.7 AFM height image (a) of the area marked by a green square in Figure 3.5 and height line profile (b) across the surface.

Note: The two dashed lines in (b) correspond to the two blue crosses in (a).

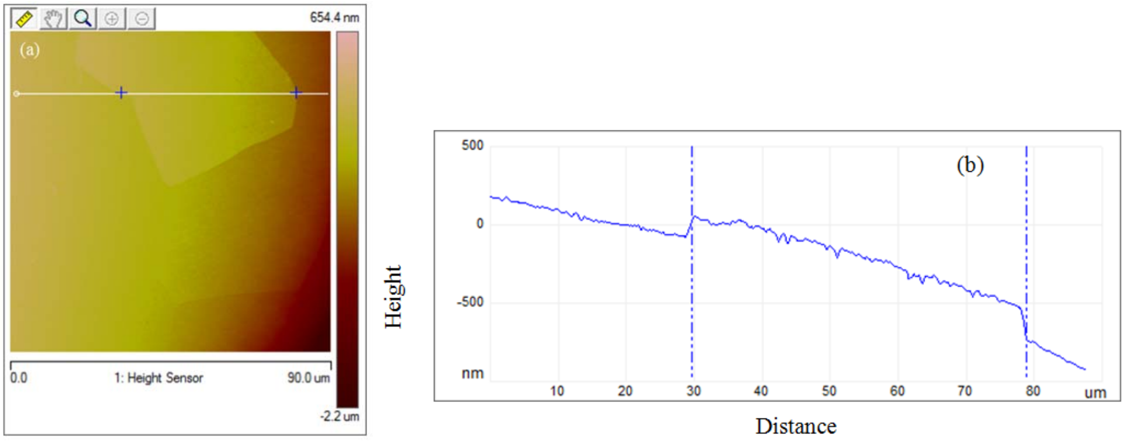

Figure 3.8 AFM height image (a) of the area marked by a yellow square in Figure 3.5 and height line profile (b) across the surface.

Note: The two dashed lines in (b) correspond to the two blue crosses in (a).

Optical profilometry provides three dimensional surface profile measurements without contact. It can be used to measure a wide range of surface heights on clean and dry surfaces. Therefore, it may be a useful tool to examine the surface heights of the entire Pt specimen surface.

The principle of optical profilometry is based on interferometry, in which the light reflected from a reference mirror combines with the light reflected from the sample surface, and the difference in the optical path is detected and converted to the height information. When the best-contrast interference fringes appear, it indicates the optical profiler is at its best focus.

There are two modes of surface profiler systems: phase shift interferometry (PSI) mode and vertical step interferometry (VSI) mode. Generally, PSI mode is used to measure small steps and smooth surfaces, and VSI mode can be used to measure steps up to one millimeter high and rough surfaces. After comparing the limits of the dynamic range (which is the greatest vertical distance the profiler can accurately measure) of the two modes, the VSI mode was selected for Pt electrode surface profile measurement.

The optical micrograph of Sub #E at a magnification of 500× is shown in Figure 3.9. The optical profilometry of Sub #E is displayed in Figure 3.10. Figure 3.10 shows a 2D plot with color-coded step height contour information. As seen in the plot, the resulting surface-height difference of the polycrystalline Pt electrode after the etching procedure is depicted in color. The blue color region indicates the recessed surface, and the red color represents a protruding region of the sample surface. The maximum height of the sample surface in this image as determined by optical profilometer is about 0.70 μm, which is larger than the surface step height results from AFM. As seen in the image, the surface height detected by the optical profilometry is not uniform within one grain. In addition, it is well known that optical profilometry suffers from artifacts at the step edge when the step heights of the surfaces are less than the coherence length of the light. The optical profilometer is useful for step height characterization of the entire sample surface, but it produces fringe skewing effects due to its design and the light source in use. Therefore, it was not further employed in the surface characterization of polycrystalline Pt substrate electrodes.

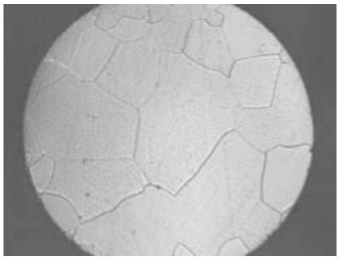

Figure 3.9 Optical micrograph of Pt Sub #E (500×) from optical profilometer.

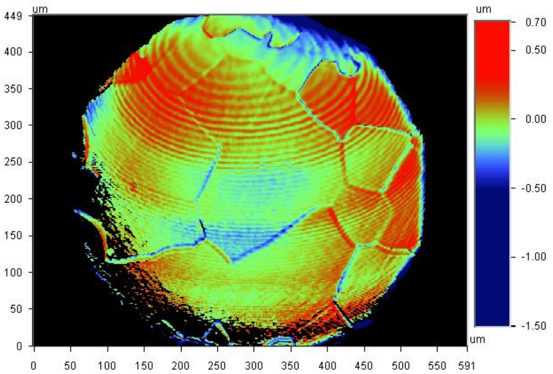

Figure 3.10 Optical profiler image of Pt substrate #E.

3.4.3 Surface Characterization by EBSD

Different single crystal domains were produced in the etching step as described in Chapter 2. As mentioned in Chapter 1, EBSD is a powerful quantitative imaging technique that can provide crystal type, crystallographic orientation, grain boundary character, and phase distribution information from single and polyphase crystalline materials.[83] Therefore, it is employed to obtain the crystallographic orientation of the platinum single crystallites. Based on the crystallographic orientation information coupled with the surface step height information from AFM results, the correlation between the crystallographic orientation and the etching rate of single crystallites can be determined. Moreover, valuable crystallographic orientation information will be used in the relationship of structure-activity study for other electrochemical reactions.

For the polycrystalline Pt substrate examined here, the disk surface was scanned at a step size of 1 μm in approximately 4 h. Figure 3.11 displays a SEM image of the Pt substrate electrode that was mapped with EBSD.

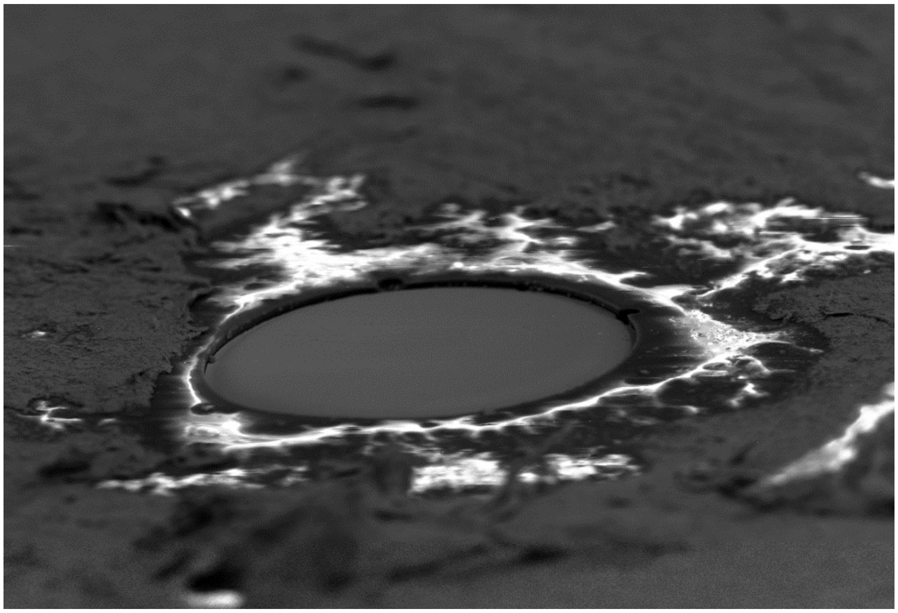

Figure 3.11 SEM image of Pt Sub #J.

Note: The disk is the Pt wire, and surrounding white areas are epoxy resin. The black material near the border of the image is silver paint painted around the whole substrate surface to make it conducive for SEM imaging.

The EBSD inverse pole figure (IPF) map is shown in Figure 3.12a. Because the sample was tilted at 70 degrees from horizontal towards the phosphorous screen in the EBSD measurement, the resultant EBSD IPF map of the Pt disk is elliptically distorted. The IPF map color gives an indication of the crystal direction aligned with the surface normal. In general, the points colored red have <100> directions aligned with the sample normal, the points in green are <110> oriented, the points on the sample with a <111> axis parallel to the surface normal are in blue, and the intermediate orientations have intermediate colors. In Figure 3.12a, pure red, green, and blue colors are assigned to <100>‖ND, <110>‖ND, and <111>‖ND grains, respectively. The variety of the colors in the contoured IPF map implies the grains on the sample surface have a variety of different orientations. A limitation of EBSD IPF map is that the coloring of pixels is based on the projection-parallel axis and is independent of the rotation about the axes. Therefore, grains with the same color code may have different orientations. In spite of this drawback, the IPF-based orientation maps are most useful for understanding the preferred orientation parallel to a sample direction of interest. In this case, the interested sample direction is the surface normal direction. In addition, the corresponding orthogonal plane information can be obtained owing to the face-centered cubic (fcc) crystal structure of platinum.

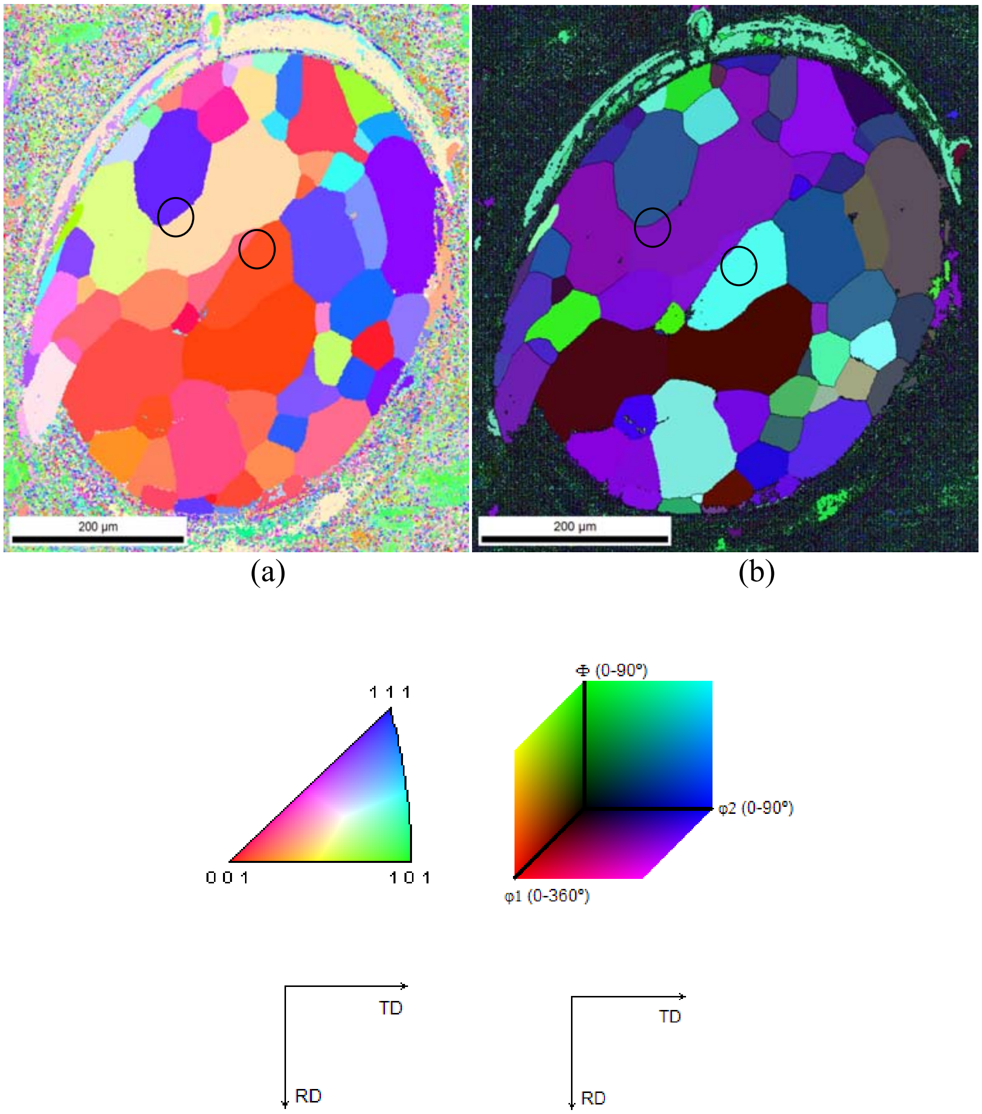

(a) (b)

Figure 3.12 EBSD IPF and Euler angle map.

Note: (a) EBSD IPF map of the polycrystalline Pt substrate electrode (Sub #J). The typical color triangle represents the normal direction (ND). (b) EBSD Euler angle map of Pt Sub #J. The color legend represents the three Euler angles φ1, Φ, φ2. The grains marked by circles are used to emphasize different crystallographic orientations in both IPF and Euler angle maps.

An EBSD Euler angle map was also produced and is shown in Figure 3.12b. This map is based on Euler angles, φ1, Φ, φ2, which are three angles used to describe the crystallographic orientation of the crystal relative to a reference coordinate system (usually defined by the primary SEM stage axis). The value of each Euler angle is individually set to a color scale. As depicted in the legend in Figure 3.15b, red color represents φ1, green for Φ, and blue for φ2. The combined color of the three angles is a single RGB color standing for a defined orientation. Therefore, similar orientations will have similar colors, and different colors indicate different crystallographic orientations.

By comparing the two orientation maps, as depicted in Figure 3.12, most of the grains are coded in different colors in both Figure 3.12a and b. For example, the grains marked by circles that have different colors in IPF map also have different color contrasts in Euler angle map, which indicates the trend of variation in orientation in both IPF and Euler angle maps is the same. Therefore, the general crystallographic orientations of the platinum single crystallites are readily observed in the IPF map, and the exact crystallographic orientations with three Euler angles are achieved with the Euler angle map.

From the EBSD Euler map, a specific orientation of interest can be highlighted by coloring the pixels on the map relative to the misorientation between the orientation at that point and the ideal orientation. Figure 3.13 highlights the three low-index planes with red, green, and blue indicating (100) (Figure 3.13a), (110) (Figure 3.13b), and (111) (Figure 3.13c) planes, respectively. The intensity of the color bar is associated with the misorientation angle. The more intense color indicates a smaller misorientation angle.

The overall range of misorientation is from 0 to 30 °, where 30 ° is the maximum misorientation angle chosen for the EBSD orientation map analysis.

Comparing each of the highlighted planes of interest map in Figure 3.13 and the IPF map in Figure 3.12a, the grain orientations are very well matched in two maps. For example, the <100> grains in IPF map (colored red grains) have a (100) low-index plane (as depicted in Figure 3.13a). The results confirm that well-defined and orientated single crystal planes are produced at the polycrystalline Pt substrate electrode surface.

The grain size distribution of the single crystal grains at the polycrystalline Pt substrate electrode surface is presented in Figure 3.14. The area fraction and its corresponding diameter are also listed. As can be seen in the chart, most of the surface area is occupied by medium (~50 µm) and large (~100 µm) size grains. Relatively small grains (< 50 µm) are randomly distributed across the surface with very small fractions. The grain size information obtained in EBSD is consistent with the AFM results.

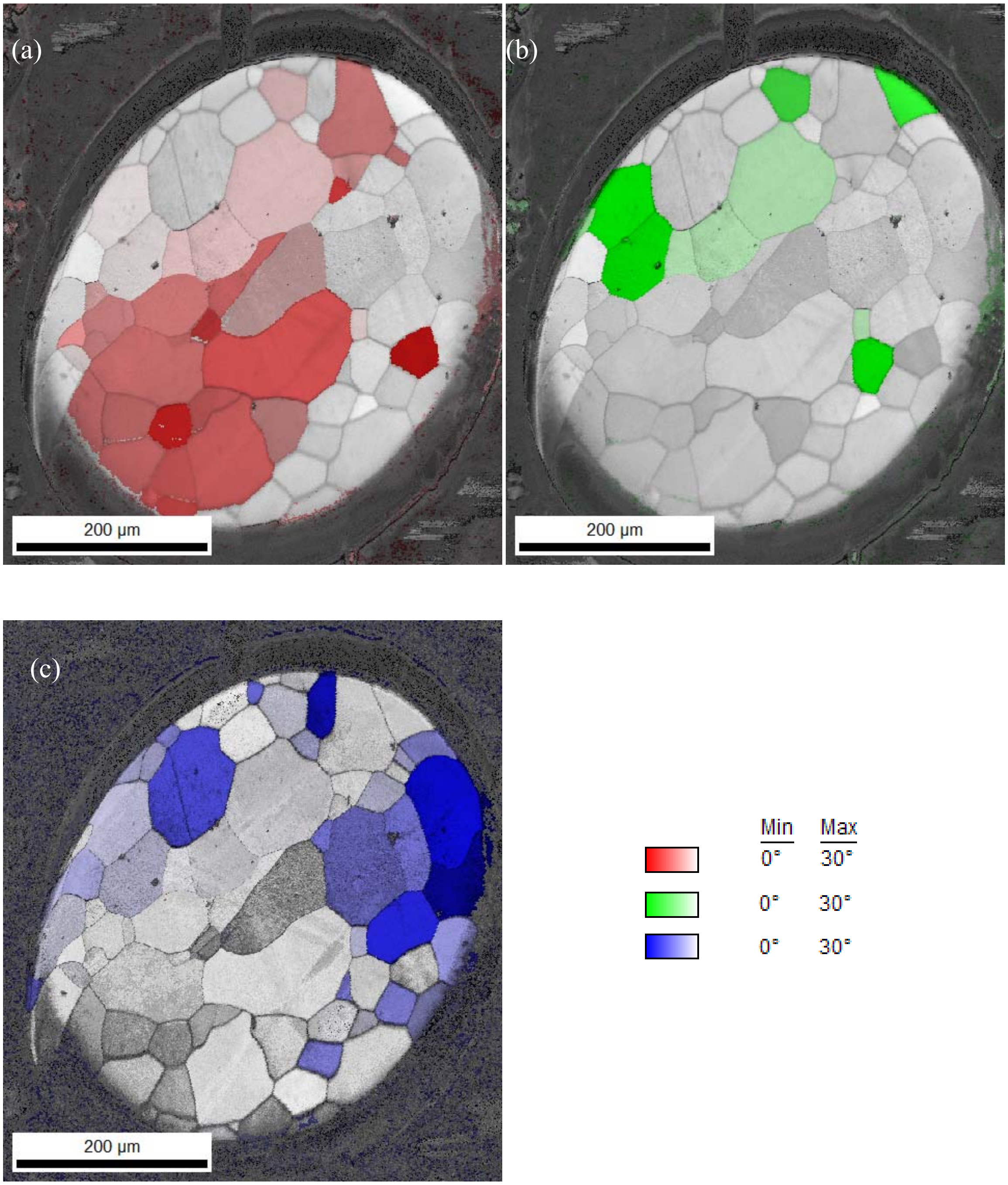

Figure 3.13 EBSD highlighted low-index planes (100) in red color (a), (110) in green color (b), and (111) in blue color (c). The color legend illustrates the degree of misorientation angle based on the intensity of the coded color.

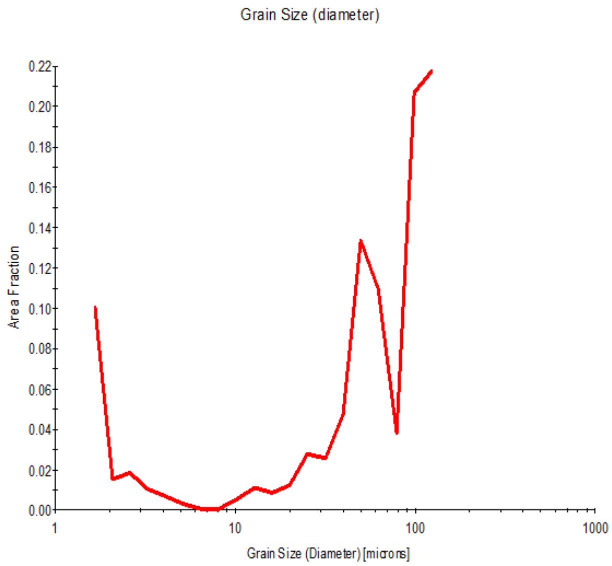

Chart: Grain Size (diameter)

Edge grains included in analysis

Diameter [microns]	Area Fraction
1.66331	0.100357
2.08665	0.0152701
2.61774	0.018217
3.28399	0.0105974
4.11982	0.00674903
5.16838	0.0029161
6.48381	0.000427592
8.13404	0.000874446
10.2043	0.00577057
12.8014	0.0108786
16.0596	0.00868282
20.147	0.0126005
25.2747	0.027493
31.7076	0.0257904
39.7776	0.0475437
49.9017	0.133663
62.6025	0.109737
78.5358	0.0381135
98.5244	0.207066
123.6	0.217252
Average	
Number	1.98871
Area	68.9077

Figure 3.14 Grain size distribution of the polycrystalline Pt substrate electrode from the EBSD scans in Figure 3.12.

Note: The diameter of the grains and the corresponding area fraction are shown on the right side.

3.4.4 Electrochemical Characterization of Pt substrate Electrode Surface by Cyclic Voltammetry (CV)

CV is performed to electrochemically clean and activate the surface of Pt substrates for electrochemical reactions. It also allows one to distinguish the potential regions corresponding to the double-layer charging and oxide growth.[115]

The cyclic voltammgram of Pt Sub #Z in 1 M H_2SO_4 solution is shown in Figure 3.15. The potential region of −0.4 V to 0 V vs. MSE is the double-layer region, where the current flows to charge the double layer. When the potential goes more positive, the formation of adsorbed oxygen or platinum oxide occurs. The cathodic current peak at 0 V is attributed to the reduction of surface platinum oxide. The two symmetric peaks between −0.45 V and −0.65 V vs. MSE are due to hydrogen atom adsorption and desorption at platinum surface.[78]

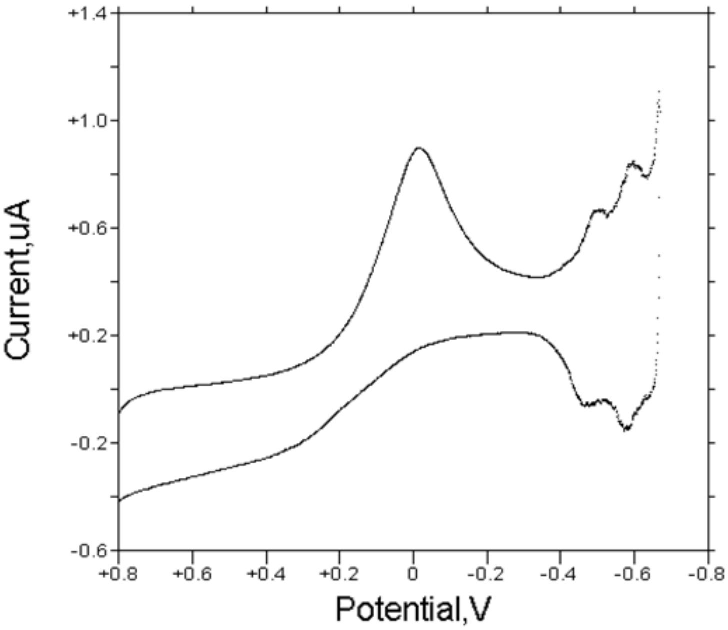

Figure 3.15 Cyclic voltammogram of 500 µm diamr Pt Sub #Z in 1 M H_2SO_4 solution at 100 mV/s scan rate. The potentials are given with respect to MSE.

Figure 3.16 shows the CV of Pt Sub #J in 1 M H_2SO_4 solution before and after the etching procedure. It can be seen in the plots that the magnitude of the platinum oxide reduction peak and the hydrogen adsorption and desorption peaks are less after etching compared to that of peaks before etching. It is believed that the current decrease between the two CVs is due to the decrease in the available sites for hydrogen or oxygen adsorption on the electrode surface after the etching procedure. In addition, it can be observed that the bulk oxygen evolution starts at a potential above +1.3 V vs. Ag/AgCl, and the bulk hydrogen evolution begins at −0.3 V.

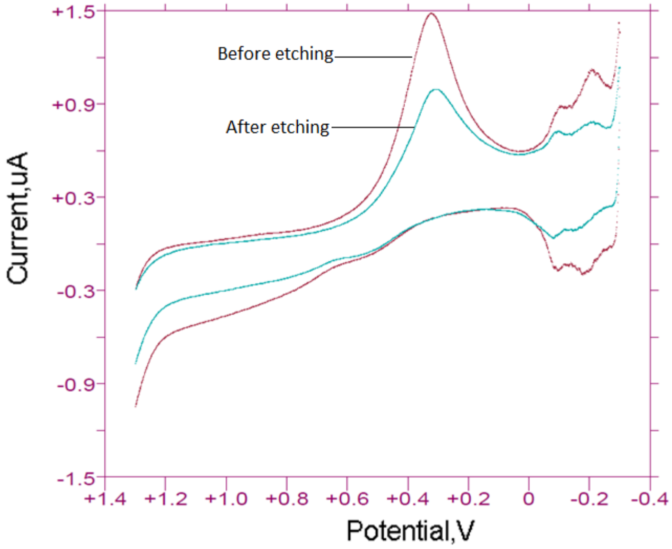

Figure 3.16 Cyclic voltammogram of 500 µm diam Pt Sub #J in 1 M H_2SO_4 solution at 100 mV/s scan rate. The potentials are given with respect to Ag/AgCl.

3.4.5 Structure-Activity Relationship of Pt Single Crystallites in an Electrolytic Etching Reaction

To examine the structure-activity relationship of the of Pt single crystallites in the electrolytic etching experiments, the crystallographic orientation and the corresponding etching rate are correlated with SEM and EBSD results. Figure 3.17 shows a transparent overlay of an EBSD IPF map on an SEM image.

In Figure 3.17a, the SEM image of polycrystalline Pt substrate electrode (Sub #J) displays the surface topographic features, clearly distinguishing protruding and recessed regions. Figure 3.17b shows the overlay of the EBSD IPF map on the SEM image of the Pt substrate #J, and as seen from the overlay picture, the shape of the grains in SEM image matches well with that of the grains in the EBSD IPF map. The protruding regions in the SEM image imply that they are the least etched, and the recessed regions are the most etched during the etching process. In Figure 3.17b, the planes coded in blue on the

EBSD IPF map are exactly superimposed on the protruding regions in SEM image.As discussed previously in Figure 3.12 and Figure 3.13, these grains have a crystal orientation of (111). These results indicate that the (111) planes (blue color) have the slowest etching rate of the three low-index planes in the surface electrolytic etching treatment. In contrast, the recessed grains, which are colored either in red or green on the EBSD map, are (100) and (110) planes.

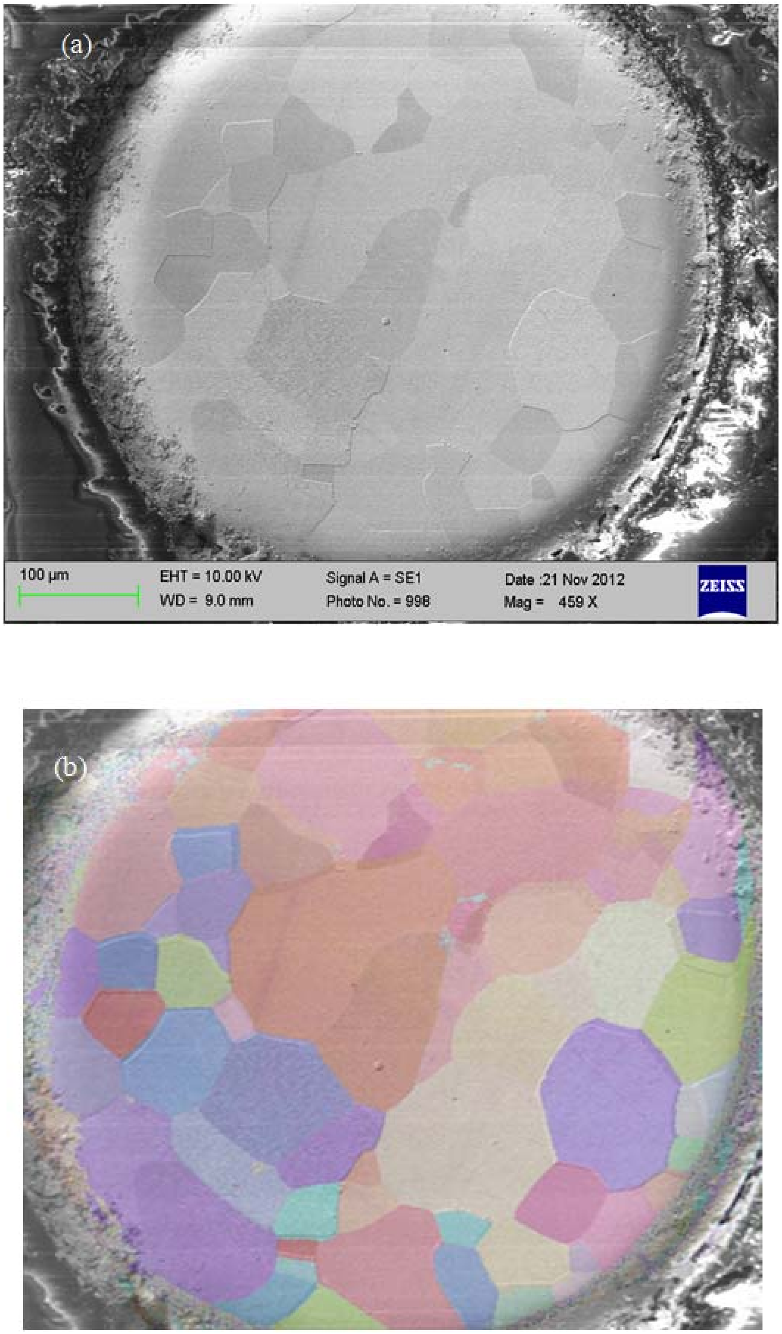

Figure 3.17 SEM image of polycrystalline Pt substrate electrode (Sub #J) (a) and an overlay of the EBSD IPF map on the SEM image (b).

Note: The images are rotated and adjusted for the overlay.

AFM results were employed to estimate the etching rate of Pt single crystallites having different crystallographic orientations during the electrolytic etching process. The delimited regions on the EBSD IPF map shown in Figure 3.18 illustrate the areas that were scanned on polycrystalline platinum by AFM. The corresponding AFM scan images and line profiles are shown in Figure 3.19.

Comparing the EBSD map and AFM results, it can be seen that the step height near the grain boundary varies with grain orientation. The AFM line profile shows the vertical distance is approximately 160 nm between (111) and (110) regions, and it is about 150 nm between (111) and (100). It can be inferred that the height difference between (100) and (110) is about 10 nm. Therefore, the general etching rate is in the order of (111) < (100) < (110).

To further evaluate the etching rate of different Pt single crystallites in the electrolytic reaction, the Pt substrate electrode was etched in 15 s increment and characterized by AFM after each etching experiment. The average step depth between the boundaries of two grains with different crystallographic orientations is obtained from multiple AFM line profile analysis ($n > 5$), and is shown in Table 3.1.

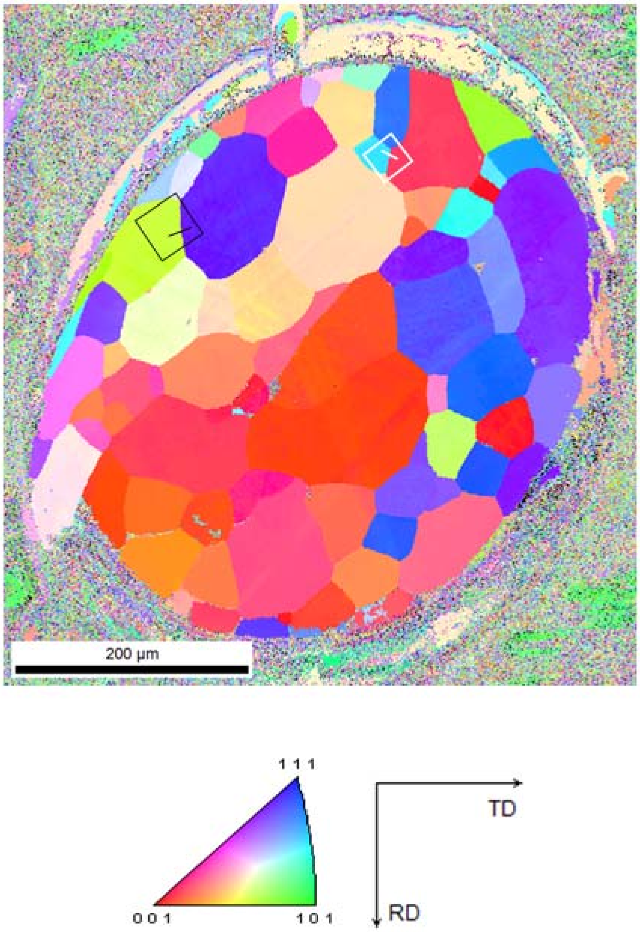

Figure 3.18 EBSD IPF map of Pt Sub #J.

Note: The regions marked by black and white squares are scanned by AFM. The lines drawn on the map across the grain boundaries correspond to the places where AFM line profiles are obtained.

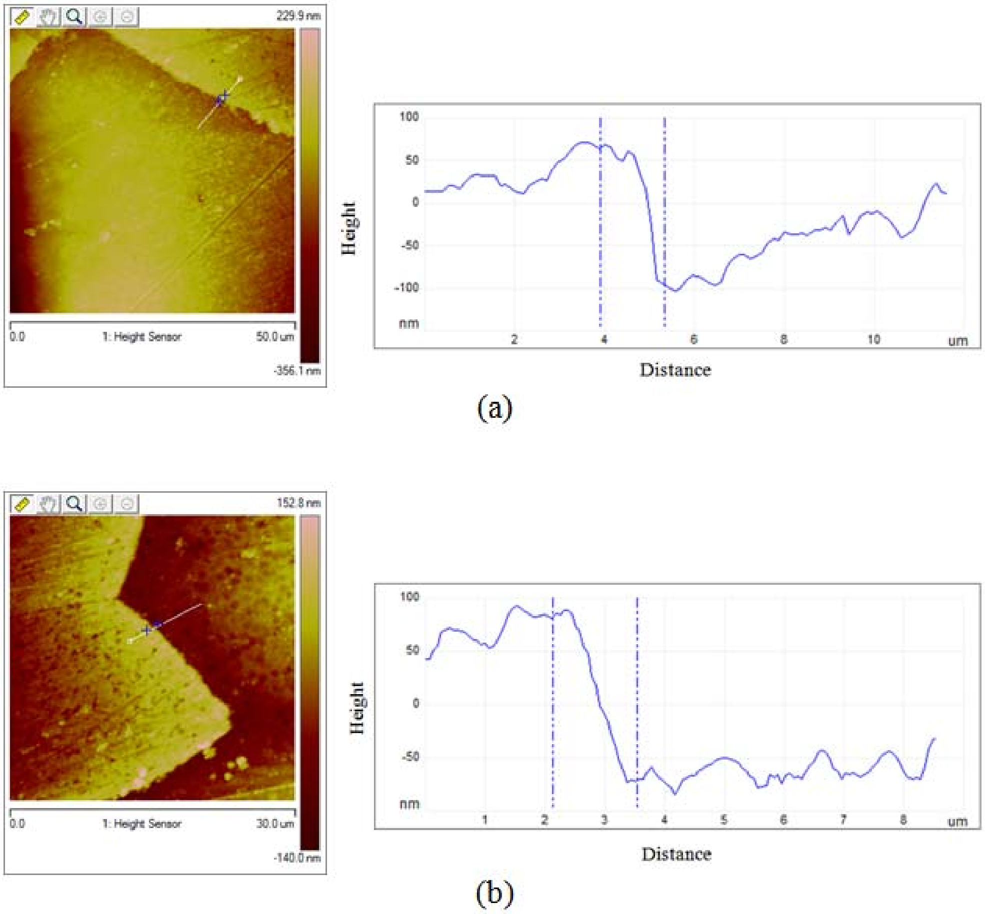

Figure 3.19 AFM height images and line profiles correspond to the regions marked by the black (a) and white square (b) in Figure 3.18.

Note: The two dashed lines correspond to the two blue crosses highlighted in AFM images.

Table 3.1 Step height between grain boundaries of Pt single crystallites with different crystallographic orientations

Overall Etching Time (s)	**$d_{(111)\text{-}(110)}$ (nm)**	**$d_{(111)\text{-}(100)}$ (nm)**
80	159 ± 6	146 ± 6
95	199 ± 8	176 ± 6
110	239 ± 6	205 ± 6
125	279 ± 9	234 ± 8

It is evident that the vertical distance between both (111) and (110) grains and (111) and (100) grains increases with etching time. The height difference between (110) and (100) can be calculated by subtracting $d_{(111)-(100)}$ from $d_{(111)-(110)}$. The step height among (111), (110), and (100) regions is plotted as a function of the overall etching time in Figure 3.20. The slopes of 2.67 nm/s for (110) grain (black line), 1.95 nm/s for (100) grain (red line) are obtained relative to the etching rate of (111), which is assumed to have a constant value. The etching rate of (100) plane relative to (110) plane is calculated by subtracting the slope of (111)-(100) from that of (111)-(110), which is 0.72 nm/s. Assuming the absolute etching rate of (111) plane is x nm/s, then the etching rate for the (100) plane is $(0.72 + x)$ nm/s.

Efforts have been made to estimate the etching rate for Pt substrate surface relative to the surrounding epoxy resin in order to have an insight in the etching rate of (111) plane. In Figure 3.21, an AFM height image was obtained by scanning across the border between the Pt disk and the surrounding epoxy resin on Pt Sub #B. As shown in the AFM line profile, the height difference between the overall Pt disk surface and surrounding epoxy resin is approximate 1.16 ± 0.12 μm.

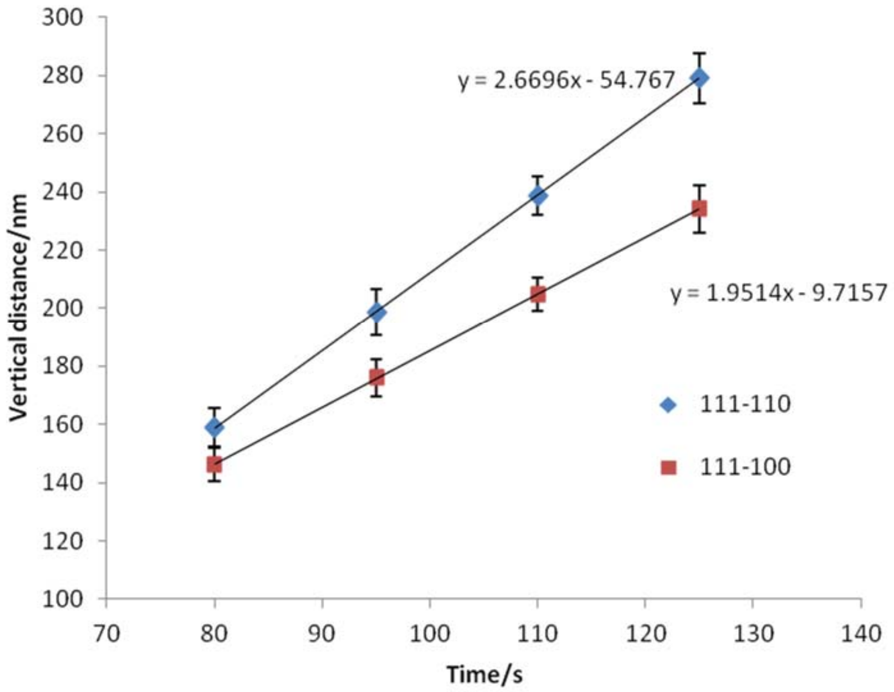

Figure 3.20 Average vertical distance ± standard deviation between Pt single crystal grains from AFM line profile analysis with different etching time.

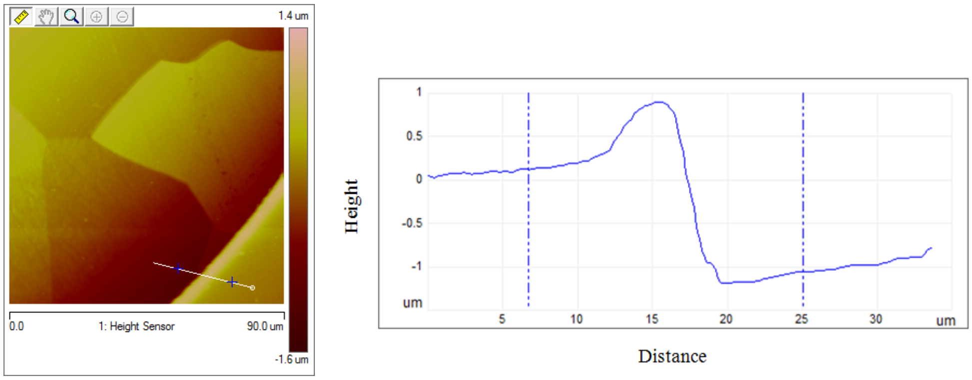

Figure 3.21 AFM height image and line profile of Pt Sub #B near the Pt disk edge.

Note: The two dashed lines correspond to the two blue crosses highlighted in the AFM image.

Given that Pt Sub #B was etched for 80 s before the AFM scan, the etching rate of the entire Pt surface relative to epoxy resin is calculated to be 14 nm/s—provided the Pt disk has the same surface height as the epoxy resin before etching. Based on this result, the etching rate of the (111) grain is estimated to be between the limit of a pure (110) surface and pure (111), i.e. 11-14 nm/s.

Several etched Pt substrate electrodes have been characterized by optical microscopy, AFM, SEM, EBSD, and CV. All the topographic information gathered by these methods essentially agree, except for the extent of the surface height changes due to various etching conditions.

The etching results demonstrated that the rate of electrolytic reaction on Pt single crystallites is evidently grain-dependent, which is closely related to the crystallographic orientation of the single crystallites. The relationship of the etching rate and the grain orientation is determined by coupling AFM surface step height measurements with EBSD characterization, and the etching rate was found to increase in the order of (111) < (100) < (110). The findings in the structure-activity relationship study in the electrolytic etching reaction are most possibly due to the differences in surface energy (γ) of different crystalline planes of a fcc metal which are known to have an order of $\gamma(111) < \gamma(100) < \gamma(110)$.[116]

3.5 Conclusions

The electrolytic etched polycrystalline metal electrode surface was characterized by optical microscopy, optical profilometry, SEM, AFM, EBSD, and CV, and the impact of structure of Pt single crystallites on the rate of electrolytic reaction in acidic etching solution is investigated.

The Pt electrode surface was examined by optical microscopy, and grain boundaries and the surface topography differences between Pt single crystal planes were observed. However, since optical techniques require a precise focus on the surface, the photographic images may not reflect the actual topography, depending on the focus condition. For this reason, SEM was employed to obtain images with high magnification and provide a better insight on the surface topography, particularly by distinguishing the protruding and recessed grains.

To provide quantitative surface height information, optical profilometry, and AFM are used. The optical profilometer is a great technology for the step height characterization of the whole sample surface. However, the artifacts near step edges impeded its further use in the surface height measurement of the polycrystalline Pt substrate electrode. More accurate surface height differences among different single crystal planes across the surface are collected from 2D and 3D AFM maps and AFM line profiles. The examined step change between two grains varies from tens of nanometers to several hundreds of nanometers, and it can reach up to a couple of micrometers near the electrode disk edge. Surface topography, such as grains with protruding and floor features, are clearly shown in AFM 3D map. In addition, slight surface tilts are discerned in AFM height line profiles. Despite the differences in grain surface height, the whole Pt electrode surface is essentially flat.

Crystallographic information for polycrystalline Pt crystal planes exposed after etching was investigated by EBSD, including the grain size, grain boundaries, crystal orientation, and crystal misorientation angle. EBSD IPF map and Euler angle maps are used to determine the crystallographic orientation of each single crystal plane on the Pt electrode surface based on the resulting map color contrast. In the EBSD IPF map, the coded color of the grain is associated with the degree of alignment between the crystal surface normal direction and the designated orientation. The actual crystal orientations are illustrated in color in the EBSD Euler angle map. The three low-index single crystal planes are highlighted in red, green and blue to represent corresponding (100) planes, (110) planes, and (111) planes of the Pt pseudo-single-crystal electrodes, respectively.

By comparing the EBSD crystallographic orientation results with the surface topography information from an SEM image, it is found that the protruding regions on the polycrystalline Pt electrode surface, which are the regions that are least etched in the surface etching procedure, are determined to be (111) planes. The recessed regions (the more etched grains) on the surface are (100) and (110) planes.

The basic electrochemical behavior of the Pt substrate electrode as a function of substrate potential was obtained by CV, and the results also reflect the surface topographic change due to electrolytic etching.

The structure-activity relation in the electrolytic reaction was further investigated by EBSD complemented with AFM line profile analysis, and the etching rate was explored as a function of etching time. The results show that the etching rate of Pt single crystallites is closed related to grain structure. It is found that the relative surface height of the (110) plane is slightly lower than that of the (100) plane from the AFM results. The relative electrolytic reaction rate is obtained from the slope of the plot of the vertical distance differences between grains verses etching time. The etching rate for the (110) grain is 2.67 nm/s faster than that of the (111) grain, and it is 1.95 nm/s faster than that of (111) grain for (100) grain. The etching rate for the Pt substrate surface relative to surrounding epoxy resin (no etching reaction occurs at the resin surface) is approximate 14 nm/s. The absolute etching rate for (111) grain is estimated in the range between 11 nm/s and 14 nm/s.

Overall, the electrolytic reaction is demonstrated to be structure-dependent, and the structure-activity relationship of Pt single crystallites is determined, which is that the reaction rate is in the order of (111) < (100) < (110).

Note, the three low-index single crystal surfaces (111), (100), and (110) determined by EBSD on the polycrystalline Pt substrate electrode are with a certain misorientation angle. Actually, the Pt single crystal domains revealed after etching are not true low-index planes, but are high-index surfaces with contributions of all three low-index grains. Detailed information of grain structure of Pt crystallite surfaces and the effect of the crystallographic orientation of high-index surfaces on the reaction rate is investigated in the electrocatalysis of HOR in the following chapter.

CHAPTER IV

STUDY OF THE HYDROGEN OXIDATION REACTION ON PLATINUM BY SCANNING ELECTROCHEMICAL MICROSCOPY

4.1 Introduction

The great importance of hydrogen oxidation reaction (HOR) lies in its crucial role as the fundamental electrocatalytic reaction in electrochemistry and its application in energy conversion devices (a fuel cell anode reaction). The catalytic activity of HOR on platinum catalyst materials has been studied to understand its kinetics, reactivity, and mechanism in different electrolyte systems by several techniques, such as CV, RDE, RRDE, and recently, SECM.[23,41,46] Much effort has been devoted to understanding the influence of surface structure and crystallographic orientation of Pt-based electrocatalysts on reactivity in an attempt to search for lower-cost and more efficient electrocatalysts for HOR with applications in fuel cells and many other electrochemical applications. For example, the electrochemical behavior of hydrogen adsorption on Pt low- and high-index planes has been examined by cyclic voltammetry in acid and alkali solutions.[7] It was found that the electrochemical features of Pt single crystal electrodes vary systematically with the surface structure and the pH of the solution.[106] Marković's group studied the relationships between the atomic-scale structure and electrocatalytic activity in HOR electrocatalysis using (111), (100), and (110) single crystal electrodes in acid and alkali solutions, and discussed their temperature-dependent surface electroactivity.[46,53-54] The effect of chloride ion in HOR catalysis was also investigated on Pt single crystals. It was found that the HOR has faster kinetics on Pt(111) than Pt(100) in the presence of Cl^-.[23]

Most of these investigations were performed with CV, RDE, and RRDE using single-crystal electrodes. The traditional single-crystal electrode preparation is tedious and repetitive and involves a complicated fabrication for only a single crystal surface orientation at a time. Moreover, quantitative information concerning reaction pathway, and interfacial chemistry may be absent in these methods. SECM is a powerful technique to probe electrocatalytic and electrode processes. It has been used to measure the kinetics of heterogeneous and homogeneous reactions, and visualize electrochemical activity on various sample surfaces owing to its high spatial resolution.[77,59] Approach-curve and imaging methods in SECM have been used to study the kinetics and reaction mechanism of HOR in acid solutions.[66] However, to the author's best knowledge, no previous work has visualized the HOR activity on Pt single-crystal electrodes in acid media by SECM imaging techniques or investigated the relationship between the electrocatalytic activity and crystallographic orientation of a single crystal platinum catalyst in the electrocatalysis of HOR. In addition, it is well known that the high-index facets are extremely difficult to prepare and maintain as macroscopic single crystals due to their large surface energy. It is also very challenging in probing the electrochemistry and surface structures at high index surfaces.[7]

With the electrolytic etching method described in Chapter 2, high-index surfaces can be readily revealed on a polycrystalline platinum surface. (More details regarding high-index surfaces will be given in this chapter). In this study, an approach was developed to study the electrocatalytic activity of platinum toward the HOR on high-index single crystal surfaces in acidic media using scanning electrochemical microscopic imaging techniques. With the help of SECM techniques, the heterogeneity of the electrocatalytic activity of different Pt pseudo-single-crystal electrodes can be examined readily in a single scan experiment and displayed in color contrast.

However, a disadvantage of this etching method when using SECM imaging in the constant height mode is the topographic variability from the etching procedure. A schematic diagram of imaging with SECM constant height mode is illustrated in Figure 4.1. The uneven surface of the polycrystalline platinum substrate electrode may cause variation of tip current as the tip scans over the substrate electrode surface at a constant height.[117]

The influence of the topographic discrepancy on the study of the electrocatalytic activity of Pt single crystal surfaces on polycrystalline platinum substrate is evaluated by employing a $DMAFC^{+}/DMAFC^{2+}$ redox couple with fast kinetics as a topography probe. The correlation between the electrochemical activity and crystallographic orientations of Pt high-index pseudo-single-crystal electrodes is determined by coupling the SECM imaging scan results with EBSD IPF map. Moreover, kinetic and mechanistic information for HOR on Pt high-index pseudo-single-crystal electrodes is evaluated.

4.2 Experimental

4.2.1 Reagents

(Dimethylamino)methylferrocene (96%, Sigma-Aldrich Co.), potassium sulfate (ACS reagent, ≥ 99.0%, Sigma-Aldrich Co.), sulfuric acid (TraceMetal™ grade, 93%-98%, Fisher Scientific), and sodium borate (ACS grade, 99.7%, Fisher Scientific) were used as received. All solutions were prepared from 18 MΩ-cm deionized water (Nanopure, Barnstead). Two redox mediator solutions were prepared fresh immediately prior to these experiments: 1.25 mM $DMAFc^+$ + 10 mM sodium borate solution (buffered to pH = 8.5 with 0.5 M boric acid), and 10 mM H_2SO_4 + 0.1 M K_2SO_4 solution (pH = 2.8).

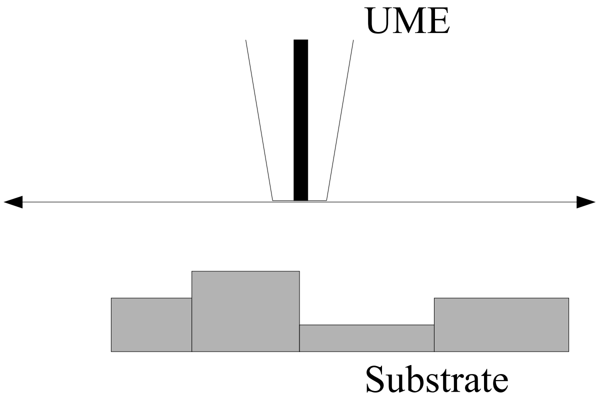

Figure 4.1 Schematic diagram of UME moving over the etched polycrystalline platinum substrate electrode surface in SECM constant height mode.

4.2.2 Electrodes

Tip preparation. 5 μm and 10 μm diam Pt wires (Goodfellow Metals, Ltd., Cambridge, U.K.) were used to build imaging ultramicroelectrode (UME) tips for SECM measurements. The procedure was similar to a previously described method.[118,119] Pt wire about 1 cm long was placed into one end of a flint glass capillary, o.d./i.d = 2.0/1.0 mm (FHC Corp., Brunswick, ME), which was then sealed at this end using a propane flame. The wire was then heat-sealed in the glass by applying vacuum to the capillary and melting the closed end of the capillary with an electrically heated nichrome coil, leaving approximately 0.3 cm of the wire protruding into the capillary. The sealed end of the electrode was examined under a microscope to make sure the wire was completely sealed at the tip and no air bubble trapped near the wire surface. An electrical connection between the unsealed end of the Pt wire and a 30 ga Cu wire (for external connection) was made with silver epoxy (EPO-TEK H2OE, Epoxy Technologies, Billerica, MA). A small amount of fast drying epoxy (DECVON, Riviera Beach, FL) plugged the open end of the glass capillary. After this, the sealed end with the Pt wire was cut to expose the Pt wire disk. Wet grinding was done to the cross section of the Pt wire disk with successive grades of 400, 800, and 1200 grit silicon carbide paper. The Pt electrode surface was successively polished with 15 μm, 5 μm, 3 μm, 1 μm, and 0.05 μm alumina slurries until a mirror-like finish was achieved. The glass sheath surrounding the Pt wire was conically sharpened until the RG value (the ratio of the diameter of disk electrode to the diameter of the Pt wire) is less than or equal to 10 .[120]

Substrate preparation. The construction of the Pt substrate electrode was described in Chapter 2.

Saturated mercury sulfate reference electrode (MSE) (Hg/Hg_2SO_4, 0.640 V vs. NHE) was used in sulfuric acid solution, and a silver/silver chloride reference electrode (Ag/AgCl, 3M KCl, 0.241 V vs. NHE) was used in $DMAFC^+$ solution to avoid a discoloration of the MSE reference junction that occurred in this solution. A Pt wire was used as the auxiliary electrode.

4.2.3 Instrumentation

SECM experiments were performed with our home-built SECM instrument. The schematic diagram is shown in Figure 4.2. As described previously[121,117], the basic SECM apparatus consisted of three major components: a positioning and control system, the data acquisition system, and the electrochemical cell setup. A three dimensional piezoelectric and motorized positioner controls the tip movement in X, Y, and Z orthogonal axes via a piezoelectric inchworm controller (Burleigh Instruments, Fishers, NY). A bipotentiostat (EI 400 Ensman instrumentation, Bloomington, IN) was used to apply potentials and measure current at the tip and substrate at the same time. The electrochemical signal data were collected from the potentiostat with custom LabView software in conjunction with a data acquisition and I/O board (National Instrument). The electrochemical cell was placed on a tilt-adjustable stage to reduce sample tilt. In the electrochemical cell, the working electrode, the reference electrode, and the auxiliary electrode were situated vertically in about 10 mL electrolyte solution as illustrated in Figure 4.2. The substrate electrode was positioned at the bottom of the cell with the polished substrate surface facing up the solution. To monitor the tip position when the tip was approaching the substrate surface and to locate the tip over features of interest on the substrate, a video microscope monitored the tip or the substrate through an optical window. The whole SECM instrument was located on a vibration isolation workstation to minimize the vibrational noise from the surroundings.

All voltammetry experiments were carried out with a BAS 100 B/W electrochemical workstation (BAS, West Lafayette, IN).

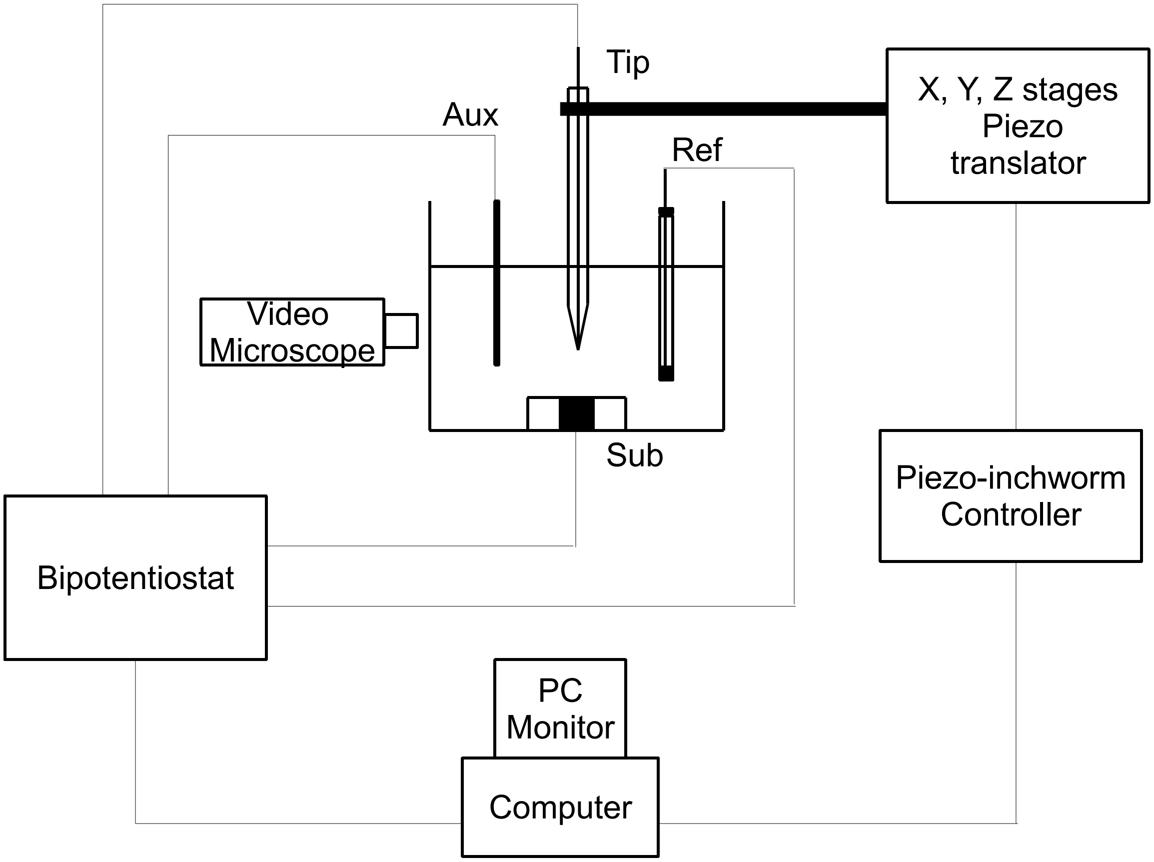

Figure 4.2 Schematic diagram of SECM instrument.

4.2.4 Method

In routine SECM experiments, it is very important to consider the electrochemical characterization of the probe and the substrate as the first step before performing further quality and quantity characterization experiments in the SECM electrochemical cell. Therefore, cyclic voltammetry tests were used to verify the electrode was working properly before running SECM experiments. CV experiments were done by scanning between +0.8 V and 0 V (vs. MSE) in 1 mM $DMAFc^+$ + 10 mM sodium borate solution or between −0.6 V and −1.6 V in 10 mM H_2SO_4 + 0.1 M K_2SO_4 solution at a scan rate of 100 mV/s. For surface cleaning and catalytic activation, the Pt tip and substrate were cycled between +0.8 V and −0.8 V (vs. MSE) at a scan rate of 100 mV/s in 1 M H_2SO_4 solution until reproducible cyclic voltammograms were obtained.[122]

In SECM experiments, the tip movement is controlled by the piezo-translator in X, Y, and Z axes. The X, Y plane is defined as the plane of the polished flat Pt substrate electrode surface, and the Z axis is defined as normal to the substrate electrode surface. Approach curves were conducted to determine the distance between the tip and the substrate using conventional SECM feedback mode in $DMAFc^+$ solution. [59] A negative-feedback-mode approach curve was performed first over the insulating epoxy resin since it conveniently helped to bring the tip close to the substrate due to its sole blocking effect at small tip-sample separation distance. The tip was moved toward the substrate surface with 1 µm increment at a maximum speed of 5 µm/s along the Z axis. The tip current was recorded at each step when the tip was approaching the substrate. When the tip-substrate separation reached about 10 µm, the approach was stopped. Then line scans were carried out in the X and Y directions at a scan rate of 100 µm/s to position the tip at a known location over the substrate. After this initial positioning, an area of 200 μm × 200 μm was scanned on the substrate at scan rates ranging from 50 to 100 μm/s. The tip-substrate separation distance ranged from 1 to 10 μm in SECM imaging experiments.

After SECM imaging scans in $DMAFc^+$ solution, the solution was changed to the H_2SO_4 solution in order to interrogate the catalytic activity of Pt single crystal planes towards the HOR. The SECM imaging scans were performed over the same area using the same experimental parameters as the $DMAFc^+$ oxidation imaging scans.

All the SECM experiments of HOR were conducted in 10 mM H_2SO_4 + 0.1 M K_2SO_4 solution using feedback mode. In both approach curve and SECM scan imaging experiments, the tip potential was held at −1.5 V (vs. MSE) at which hydrogen gas was generated, and the diffusion-limiting tip current was reached for the H^+ reduction reaction. The substrate potential was varied in SECM imaging experiments to investigate the potential dependence of the HOR on Pt catalysts. The initial scans were performed with the substrate at open circuit potential (OCP). After the imaging scans, approach curves were obtained at several interesting spots across the Pt substrate electrode surface with the substrate potential set at different values. All electrochemical measurements were carried out at room temperature.

4.3 Results and Discussion

4.3.1 Characterization of Pt Tip and Substrate Electrode

The disk surface of the Pt tip and substrate electrodes were visually examined with an optical microscope to ensure the RG value (the ration of the radius of the disk electrode to the radius of the metal wire) of the sharpened UME was less than 10. The electrochemical characterization of the SECM UME tip and Pt substrate electrode was carried out by recording the CVs in 1 mM DMAFc$^+$ + 10 mM sodium borate solution (buffered to pH = 8.5 with 0.5 M boric acid). The cyclic voltammogram displays a typical sigmoidal shape and plateau-limiting current response that are characteristic of diffusion-controlled behavior of an UME, as shown in Figure 4.3a. It can be seen that DMAFc$^+$ oxidation occurred at the Pt tip above +0.4 V, and the diffusion limited current for the DMAFC$^+$ oxidation reaction (DMAFc$^+$ - e$^-$ $\rightleftharpoons$ DMAFc^{2+}) is approximately 1.0 nA in the potential range between +0.4 V and +0.8 V. In both SECM imaging and approach curve experiments, the tip is held at +0.7 V at which DMAFC$^+$ is oxidized to DMAFC^{2+} and the current is limited by the mass transport rate. Figure 4.3b shows the current response of a Pt substrate electrode in DMAFc$^+$ solution during potential cycling. The cathodic response for DMAFC$^+$ reduction can be seen between potentials +0.3 V and 0 V. The Pt substrate potential is therefore set at +0.1 V vs. Ag/AgCl.

The CVs of the Pt UME tip and substrate in 10 mM H_2SO_4 + 0.1 M K_2SO_4 solution are shown in Figure 4.4. The cathodic current attributable to the proton reduction at the Pt tip is observed in the potential region negative of −0.85 V, and the diffusion limited current for the proton reduction reaction ($2H^+ + 2e^- \rightleftharpoons H_2$) is approximately −130 nA between potentials of −1.2 V and −1.6 V (vs. MSE), as illustrated in Figure 4.4a. Figure 4.4b shows the CV of Pt substrate cycled between 0 V and −1.4 V (vs. MSE). The cathodic peak around −0.9 V is from proton reduction, and the anodic peak around −0.75 V is due to hydrogen oxidation. Therefore, the substrate potential (E_{sub}) is initially set at −0.75 V vs. MSE in SECM imaging experiments, and the tip potential (E_{tip}) is held at

−1.5 V in both SECM approach curves and imaging experiments. The substrate potential were varied in the Pt electrocatalytic activity study for the hydrogen oxidation reaction.

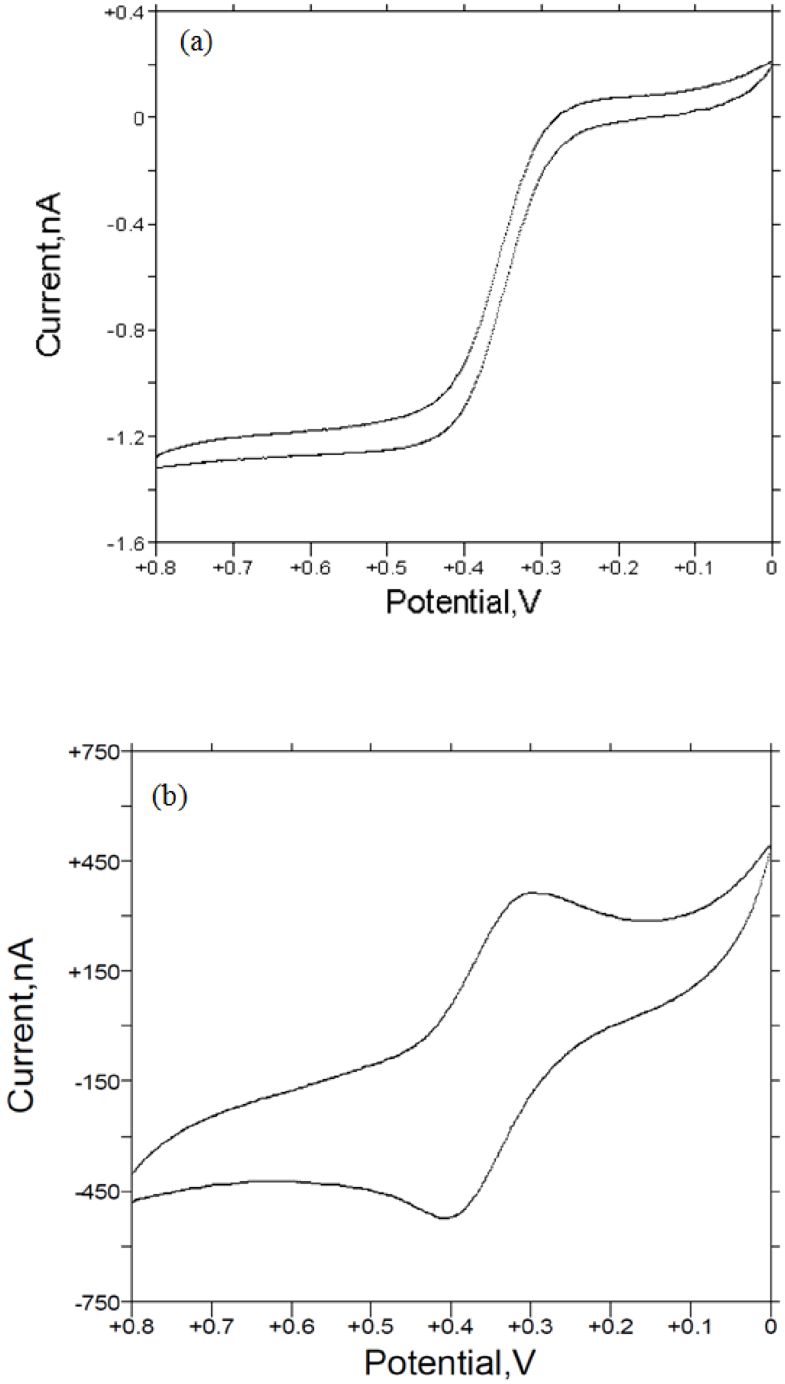

Figure 4.3 CV of (a) a 10 µm diameter Pt tip and (b) a Pt substrate electrode in 1 mM DMAFC$^+$ + 10 mM sodium borate solution at 100 mV/s scan rate.

Note: The potentials are given with respect to Ag/AgCl.

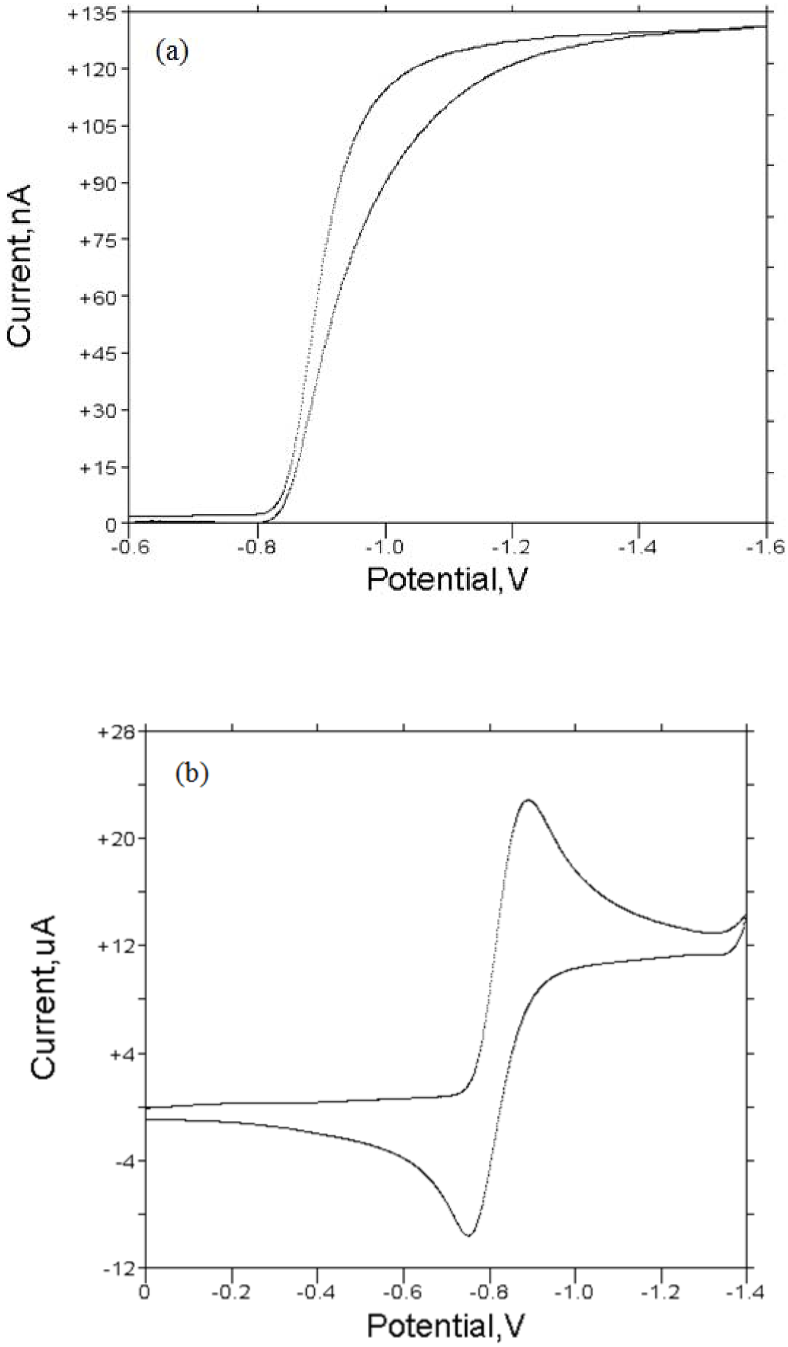

Figure 4.4 CVs of (a) a 10 μm diameter Pt tip and (b) a Pt substrate electrode in 10 mM H_2SO_4 + 0.1 M K_2SO_4 solution at 100 mV/s scan rate.

Note: The potentials are given with respect to MSE.

The cyclic voltammograms above were used to determine the diffusion-limited potentials for cathodic and anodic responses of the SECM tip and substrate in different solutions. Another important requirement for SECM tip characterization are SECM approach curves, in which the tip current changes as a function of tip-substrate separation distance towards a surface. Illustrations of the feedback behavior of $DMAFc^{+}$/ $DMAFc^{2+}$ and H^{+}/H_2 redox couples at the polycrystalline platinum surface and insulating epoxy sheath in the SECM cell are given in Figure 4.5.

When the tip is held at a diffusion-limited potential and is positioned far above the substrate, the tip current can be expressed by Equation 4.1:[120]

$$i_{T,\infty} = 4nFDca \tag{4.1}$$

Where *n* is the electron transfer number, *F* is the Faraday constant, *c* is the concentration of the redox species, and *a* is the Pt tip radius. When the Pt UME approaches the substrate surface, the steady-state tip current is perturbed by the presence close proximity of the substrate. If the substrate is active towards the redox process (such as the platinum electrode surface), the tip current increases as the tip-substrate distance decreases as a result of the regeneration of the redox mediator at the substrate/solution interface (positive feedback). When the tip approaches an electrochemically insulating region of the surface, a negative feedback behavior is expected. The blocking of diffusion of the redox species to the tip at the insulating surface with a close tip-substrate separation distance results in the decrease of the tip current SECM approach curves are the best way to estimate the tip-substrate distance in SECM. Moreover, the analysis of approach curves provides useful information about the nature and reactivity of the substrate.[59, 123] Figure 4.6 shows the results of approach curves acquired at the polycrystalline platinum substrate in $DMAFc^+$ and H_2SO_4 solution, respectively. These curves plot the normalized current (expressed as $i_{T,d}/i_{T,\infty}$, where $i_{T,d}$ is the tip current at *d*, and $i_{T,\infty}$ is the UME steady-state current at infinite separation) as a function of normalized distance (expressed as *d/a*, where *d* is the tip-substrate separation, and *a* is the tip radius). Figure 4.6a shows approach curves obtained in $DMAFc^+$ solution towards Pt disk electrode and surrounding epoxy sheath surfaces with the UME held at +0.7 V and the substrate at +0.1 V. The two experimental approach curves (blue squares and green triangles) follow the positive and negative feedback theoretical curves (black line and red line) quite well as shown in Figure 4.6a. These results confirm the fast electron transfer kinetics for $DMAFc^+$ oxidation, and also validate the use of $DMAFc^+/DMAFc^{2+}$ redox couple as a topographical probe to determine tip-substrate separation.

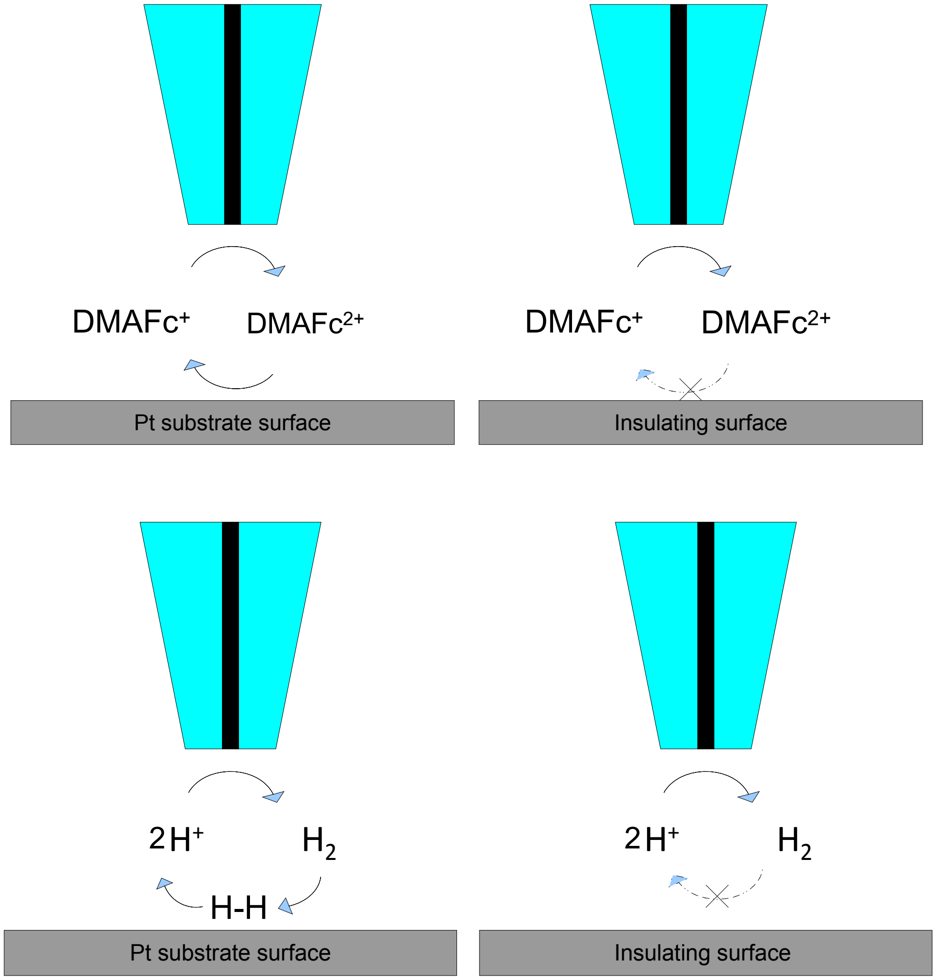

Figure 4.5 Illustration of SECM feedback modes of $DMAFc^+/DMAFc^{2+}$ and H^+/H_2 redox couples at Pt substrate surface (left) and insulating surface (right) in SECM cell.

In H_2SO_4 solution, with $E_{sub} = -0.75$ V, hydrogen is formed at the tip by hydrogen ion reduction. These ions can be regenerated at a closely spaced polycrystalline platinum substrate due to the catalytic hydrogen oxidation reaction (as illustrated in Figure 4.5), which occurs at the catalytic Pt surface through coupled dissociation, chemisorption, and electron transfer steps as follows:

$$\mathrm{H_2 + 2Pt \rightarrow 2Pt(H)} \tag{4.2}$$

$$\mathrm{2Pt(H) \rightarrow 2Pt + 2H^+ + 2e^-} \tag{4.3}$$

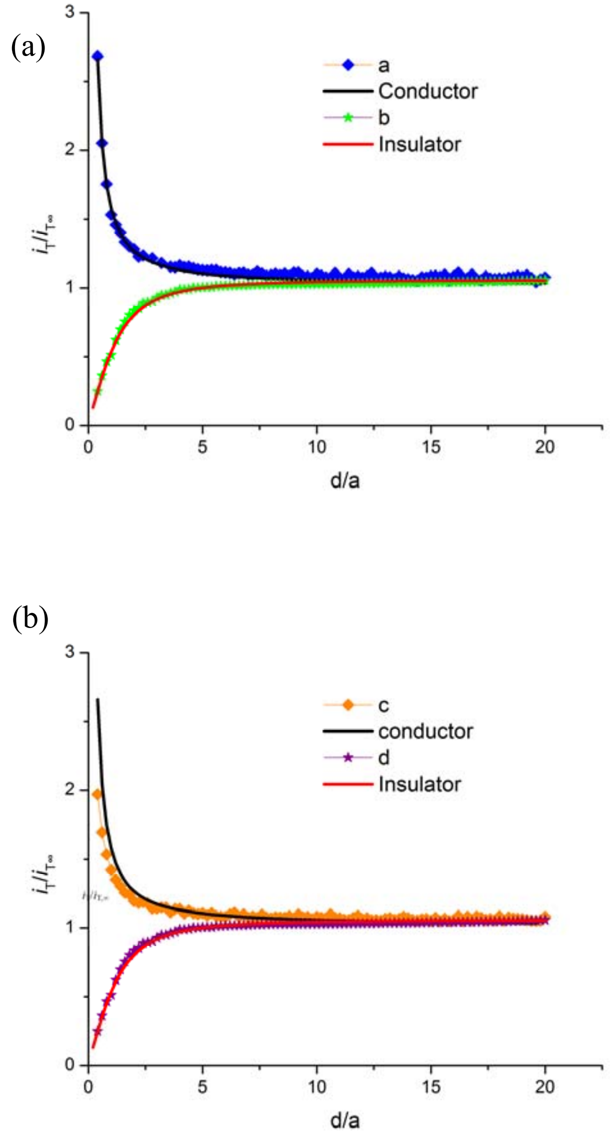

Figure 4.6 Experimental SECM approach curves (solid symbols) obtained in feedback mode at a Pt substrate surface (a, c) and surrounding insulating epoxy surface (b, d), and corresponding theoretical curves (solid lines).

Note: 10 µm diam Pt UME is used in (a) 1.25 mM $DMAFc^+$ + 10 mM sodium borate solution (E_{tip} =+0.7 V, E_{sub} = +0.1 V vs. Ag/AgCl), and (b) 10 mM H_2SO_4 + 0.1 M K_2SO_4 solution (E_{tip} = −1.5 V, E_{sub} = −0.75 V vs. MSE). The approach rate is 0.5 µm/s.

It has been reported that the HOR requires catalytic surfaces with strong H atom adsorption capability, and that Pt, Pd, Ru, and Ir are the only metals with significant adsorption ability.[124] Therefore, the Pt disk electrode exhibits a positive feedback approach curve response with the HOR as shown in Figure 4.6b (orange diamonds). On the other hand, negative approach curves are expected on non-catalytic surfaces, just as the curve shown in Figure 4.6b (purple stars). It's evident that the degree of positive and negative feedback from the approach curves obtained in the two solutions are similar, indicating both the $DMAFc^+$ oxidation reaction and HOR are facile at the Pt surface, but not at the insulating epoxy sheath of the substrate. This easily allows discrimination between catalytic surfaces and non-catalytic surfaces. The slight differences in the experimental approach curve (curve c) and the theoretical one (conductor curve) shown in Figure 4.6b suggest the kinetics of the HOR is not as fast as the $DMAFc^+$ oxidation. The reaction rate for heterogeneous electron transfer of the HOR on a Pt substrate can be extracted by fitting the experimental approach curves with the theoretical ones, which will be discussed further in the kinetic study of the HOR

4.3.2 SECM Imaging

Although the differences in electrocatalytic activity between a conducting Pt disk and insulating epoxy surface can be demonstrated by SECM approach curves, it would be more enlightening to distinguish these differences if they can be visualized in SECM images. SECM imaging has been widely used in identifying local variations in electrochemical activity on an electrode surface and studying kinetics and mechanisms of reactions associated with electrode processes.[59] However, to the author's best knowledge, no work has been done in the application of SECM imaging techniques so far to characterize the electrocatalytic activity of Pt single crystal electrodes for the hydrogen oxidation reaction (HOR) in acid media and investigate the relationship between the kinetic activity of single-crystal platinum catalysts in HOR and its corresponding crystallographic orientation. Therefore, in this part, SECM imaging is used to study the structure-activity relationship of Pt pseudo-single-crystal electrodes for the electrocatalysis of the HOR on a polycrystalline Pt substrate.

4.3.2.1 Effect of Tip-Substrate Distance

Preliminary SECM imaging experiments were performed on an etched polycrystalline Pt substrate electrode surface (Sub #J) in 5 mM H_2SO_4 and 0.1 M K_2SO_4 solution with a 10 μm diameter Pt tip. The optical micrographic image of Sub #J is shown in Figure 4.7. Figure 4.8 displays an SECM scan at constant height over the Pt substrate surface at a large tip-substrate separation distance. The tip current shown in Figure 4.8 is very close to steady-state limiting proton reduction current ($i_{T,\infty} = -65$ nA). The slight variation in the tip current is probably due to the surface topography. The reason for the featureless DC-SECM image is that the tip current is at diffusion-controlled conditions, and there is no additional amperometric feedback current at the probe when the separation distance between the tip and the substrate is very large.

Figure 4.9a is an optical micrograph of a 500 μm diam Pt substrate (Sub #A) after electrolytic etching, and Figure 4.9b is a constant height DC-SECM scan image obtained on Pt Sub #A. The shapes of Pt single-crystal grains can be roughly discerned on the round disk region in the optical image. The higher tip current (red color) regions in the DC-SECM image corresponds to the scratched surface shown in Figure 4.9c. Even though part of the substrate surface is damaged by the scratches that were caused by the tip movement in the SECM scan, a very nice overlay can be seen between micrometer-sized features over the intact region in the optical and electrochemical images as shown in Figure 4.9d.

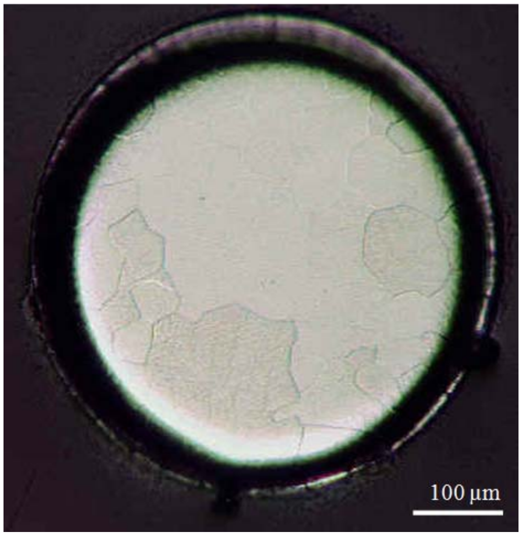

Figure 4.7 Optical micrograph of an etched polycrystalline Pt substrate (Sub #J).

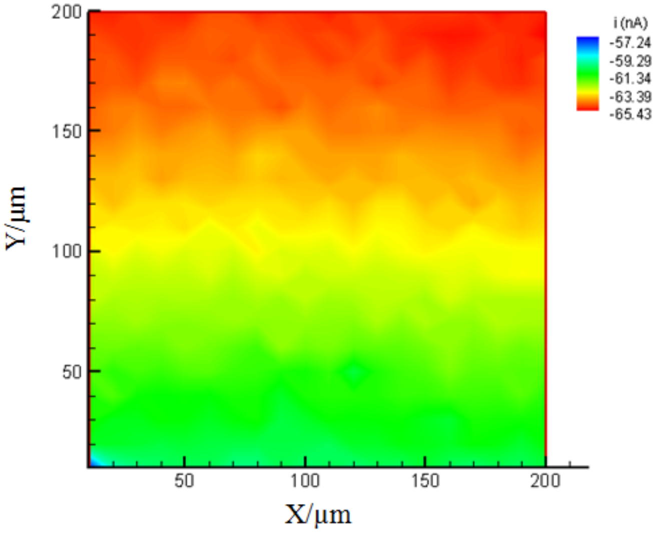

Figure 4.8 A SECM image obtained on Pt Sub #J surface with a 10 μm diam Pt tip in 5 mM H_2SO_4 and 0.1 M K_2SO_4 solution.

Note: E_{tip} = –1.5 V, E_{sub} = −0.75 V. The scan rate of 100 μm/s. The tip-substrate separation is about 50 μm.

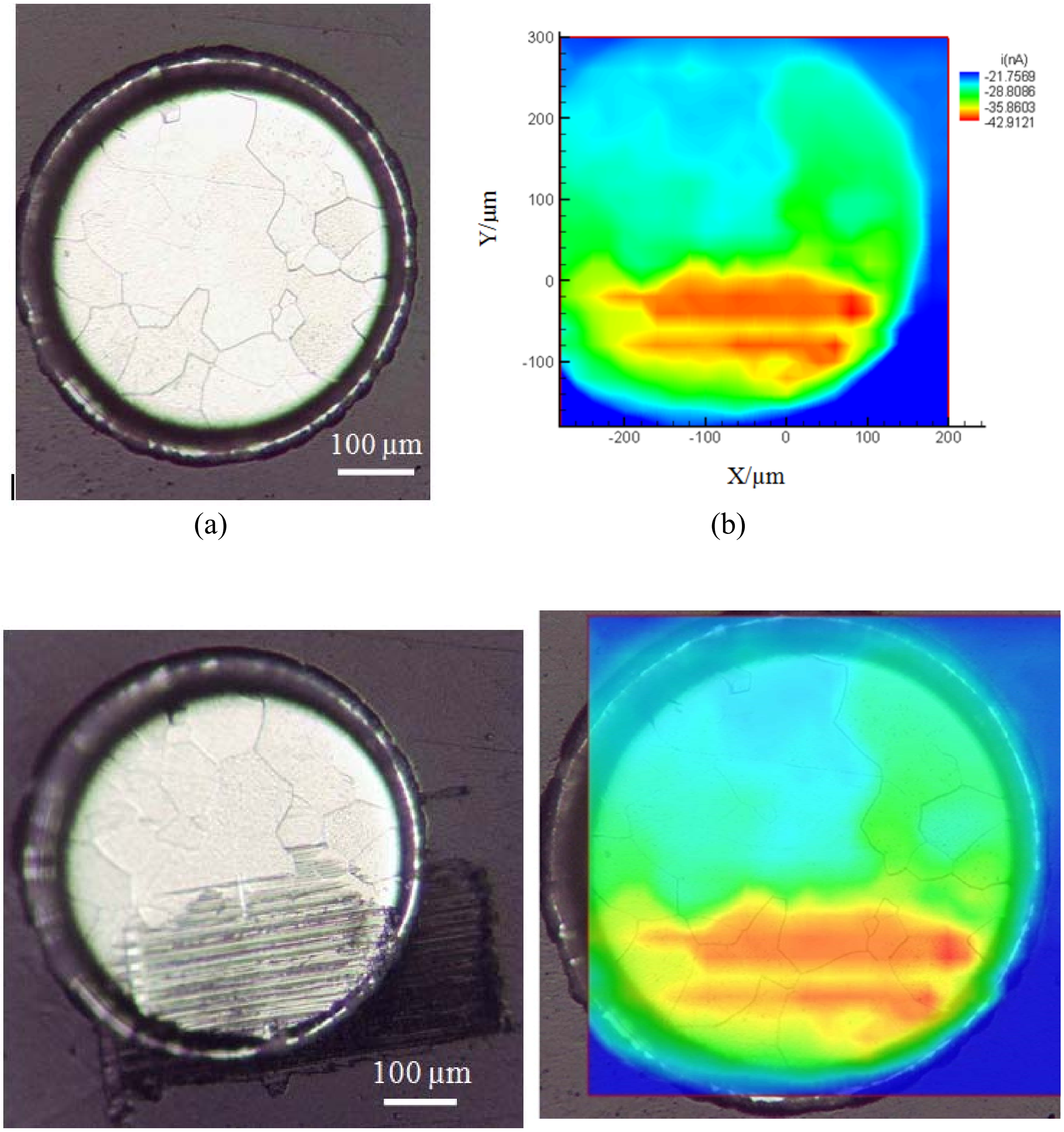

(a) (b)

(c) (d)

Figure 4.9 Optical micrographs and SECM images of Pt Sub #A.

Note: (a) Optical micrograph of Pt Sub #A before SECM imaging experiment. (b) SECM scan image of Pt Sub #A in 5 mM H2SO4 and 0.1 M K2SO4 solution with a 5 µm diam Pt tip. Etip = −1.5 V, Esub = −0.75 V. The tip-substrate separation is approximately 2.5 µm. (c) Optical micrograph of Pt Sub #A after SECM imaging experiment. (d) Composite image showing a transparent overlay of the semitransparent DC-SECM shaded contour image on the optical micrograph.

As can be seen in Figure 4.8 and Figure 4.9, SECM imaging scan of the whole surface would either lose contrast resolution when the tip-to-sample separation distance is large or accidentally damage the surface due to surface tilt when tip-to-sample separation distance is small. In order to avoid these problems and enhance the image resolution, a smaller region of the surface is scanned rather than the whole surface. This allows an appropriate tip-substrate separation distance for SECM imaging experiments without serious difficulties from substrate tilt.

Figure 4.10b shows a 250 μm × 250 μm region of Pt sub #C (the region delimited by the black rectangle in Figure 4.10a) scanned in 5 mM H_2SO_4 and 0.1 M K_2SO_4 solution with a 10 μm diam Pt tip. The resolution and contrast are greatly enhanced in this SECM image compared to the ones shown in Figure 4.8 and 4.9. A transparent overlay of the semitransparent SECM shaded contour image on the optical micrograph is shown in Figure 4.10c. The pattern (i.e., the shape of the crystalline grains) of the scanned areas produced by SECM is in accordance with that in the optical micrographic image. The variations in electrocatalytic activity for individual grains are successfully visualized with SECM.

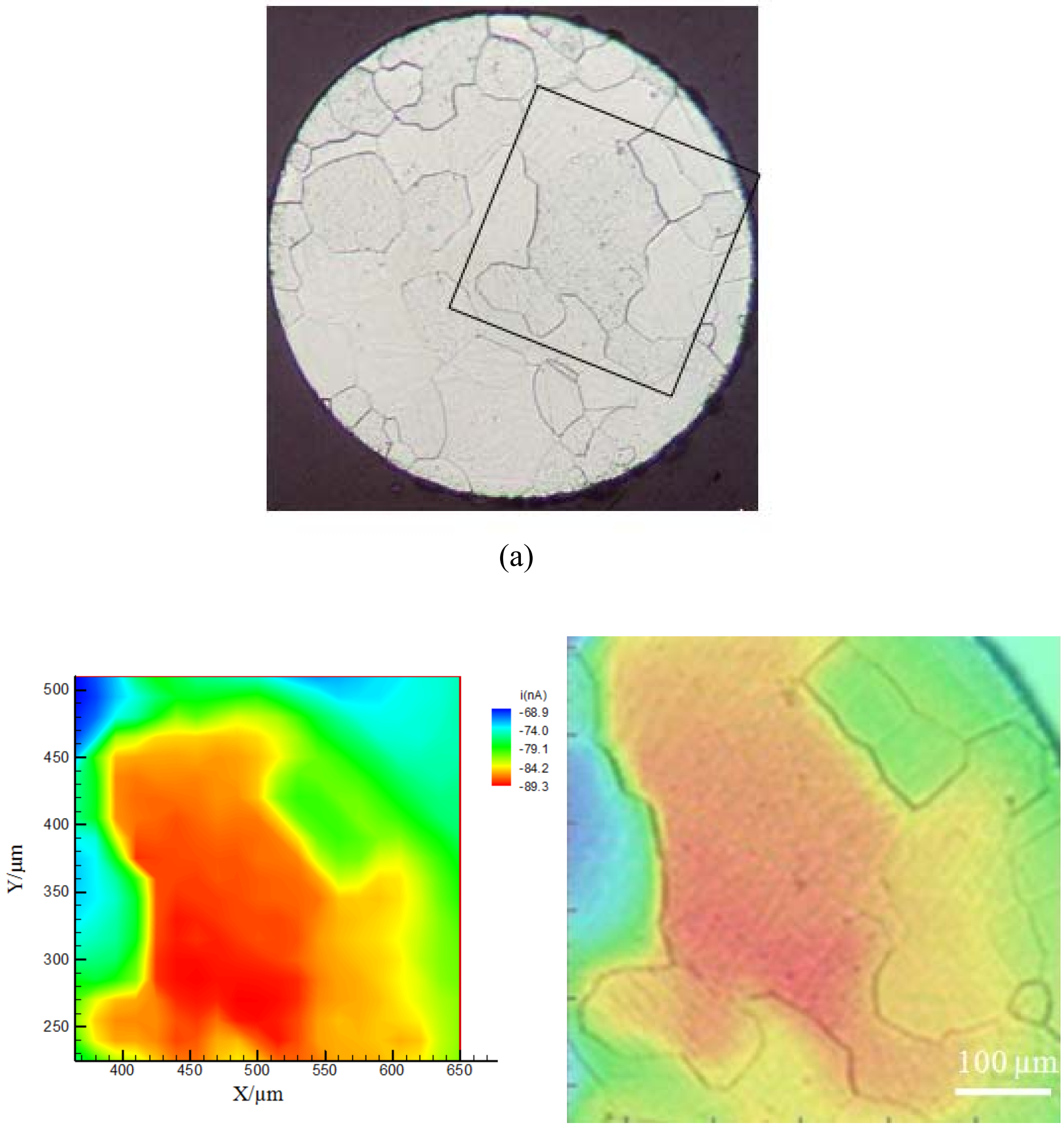

(a)

(b)

(c)

Figure 4.10 Optical micrographs and SECM images of Pt Sub #C.

Note: (a) Optical micrograph of Pt Sub #C (b) SECM scan image of a 250 µm × 250 µm scan area delimited by the black square in panel (a). The SECM image was obtained in 5 mM H_2SO_4 and 0.1 M K_2SO_4 solution with a 10 µm diam Pt tip at about 5 µm tip-substrate separation distance. $E_{tip} = -1.5$ V, $E_{sub} = -0.75$ V. (c) An overlay of semitransparent SECM image on optical image. Both pictures were rotated to the same orientation.

In SECM feedback mode, regions with high positive feedback currents should correspond to more electrocatalytically active Pt crystalline grains. However, since the Pt surface is electrolytically etched to expose Pt single crystals, the surface is uneven in height, and the current response under these conditions in DC-SECM could be influenced by these topographic effects. In other words, both the uneven surface of the Pt single-crystal electrodes and the difference in electrocatalytic activity may result in the contribution to the variation of tip current as the tip scans over the substrate electrode surface at a constant height. In order to improve the measurement of Pt electrode catalytic activity, the degree of topographic influence on the DC-SECM current map must be evaluated.

4.3.3 Effect of Substrate Topography

To investigate the topographic effect on the SECM current map, the $DMAFC^{+}/DMAFC^{2+}$ redox couple is used owing to its fast electron-transfer reaction kinetics.[55, 125] A given region of the Pt substrate surface was scanned twice in SECM imaging experiments. The first scan was in a $DMAFC^{+}$ solution with the $DMAFC^{+}$ oxidation at the probe and $DMAFC^{2+}$ reduction at the substrate. The second scan was in sulfuric acid solution with the proton reduction at the tip and hydrogen oxidation at the substrate. Since the variation of the tip current in $DMAFC^{+}$ solution is based on the positive feedback effect and the kinetic effects are minimal, the resulting current map gives a measure of topography alone. An improved measure of catalytic activity of Pt substrate toward the HOR can be achieved by decoupling the topographic contribution and the catalytic activity contribution in the SECM map obtained in the second SECM imaging scan.

Figure 4.11a and b show SECM current maps of a 250 µm × 250 µm region on Pt Sub #N using DMAFC$^+$ oxidation and proton reduction at the Pt tip, respectively. AFM 3D and 2D height images, and AFM line profile are displayed in Figure 4.11c, d, and e. According to SECM approach curve theory, the higher positive feedback current in DMAFC$^+$ solution (red color in Figure 4.11a) is associated with protruding area on platinum substrate electrode surface. Nonconductive epoxy resin region is represented by low DC current (blue color). This image suggests the surface is slightly tilted by the current change occurring in the diagonal direction across the DMAFC$^+$/DMAFC^{2+} current map over the platinum surface. Figure 4.11b shows the DC-SECM current map generated in sulfuric acid. The significant heterogeneity of the electrocatalytic activity of different Pt crystallite domains is displayed by the large variation in tip current as shown in the SECM contour image. Comparing the DMAFC$^+$/DMAFC^{2+} current map and the HOR map, it seems that the topography doesn’t exert a dominating influence on the HOR image because no features correspond to the shape of the grains are observed. In addition, the AFM results in Figure 4.11c, d and e can be used to confirm this. The maximum surface height difference between the characterized Pt crystallite domains by AFM is about 300 nm. However, as indicated by the AFM line profile (red line), the largest height difference occurs near a single spot, which is most likely an impurity particle attached to the Pt substrate surface. The blue line in the AFM line profile shows the step at the grain boundary is approximate 120 nm, suggesting the height differences between Pt single crystal domains are very small, the substrate surface is very flat, and further suggests the topographic effects are minimal under the conditions here.

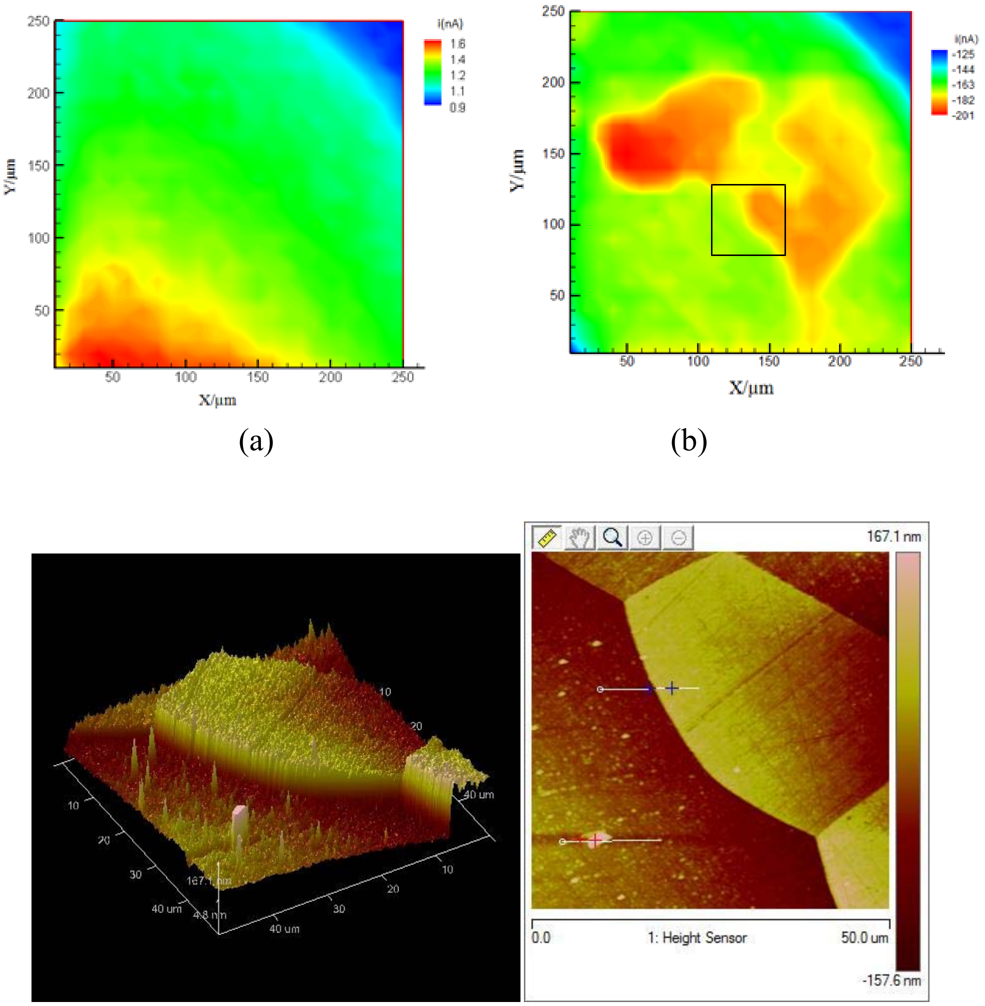

(a) (b)

(c) (d)

Figure 4.11 SECM images, AFM heigh images and AFM height line profile of Pt Sub #N.

Note: (a) SECM image obtained by feedback mode on Pt Sub #N in aqueous 1.25 mM DMAFc$^+$/10 mM sodium borate solution. E_{tip} = +0.7 V, E_{sub} = +0.1V (vs. Ag/AgCl). (b) SECM image obtained over the same region as (a) in 10 mM H_2SO_4/0.1 M K_2SO_4 solution. E_{tip} = −1.5 V, E_{Sub} = −0.75 V (vs. MSE). A 10 µm diam Pt tip is used for both images. Tip-substrate separation is about 5 µm. Scan rate is 100 µm/s. (c) and (d) are 2D and 3D AFM height images of black square marked area in panel (b), respectively. (e) AFM height line profile across the surface. The dashed lines in panel (e) are corresponding to the crosses highlighted in panel (d).

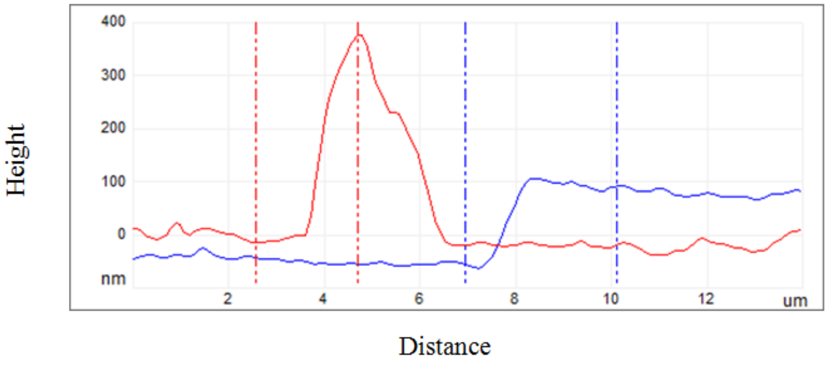

(e)

Figure 4.11 Continued

Figure 4.12b shows a SECM image scanned over an etched Pt substrate surface (Sub #W) using the DMAFC^{+}/DMAFC^{2+} redox couple at a tip-substrate separation of 1 µm. It can be seen in Figure 4.12b that the topography was imaged with DMAFC^{+}/DMAFC^{2+}, and the SECM map correlates well with the crystalline grains of the photographic image as shown in Figure 4.12c. The featureless regions on the bottom half in the SECM current map is probably due to the surface tilt. Overall, the topographic effect can only be visualized with the DMAFC^{+}/DMAFC^{2+} redox couple at a very close tip-substrate separation ($\leqslant$ 1µm). However, the SECM imaging experiments performed on Pt Sub #N toward the HOR has a tip-substrate separation of 5 µm. At this tip-substrate separation distance, the topographic effect is not apparent and dominant, as demonstrated by the featureless image shown in Figure 4.11a. Therefore, it is further confirmed the influence of surface topography on the electrocatalytic activity map of Pt pseudo-single-crystal electrodes toward HOR is negligible.

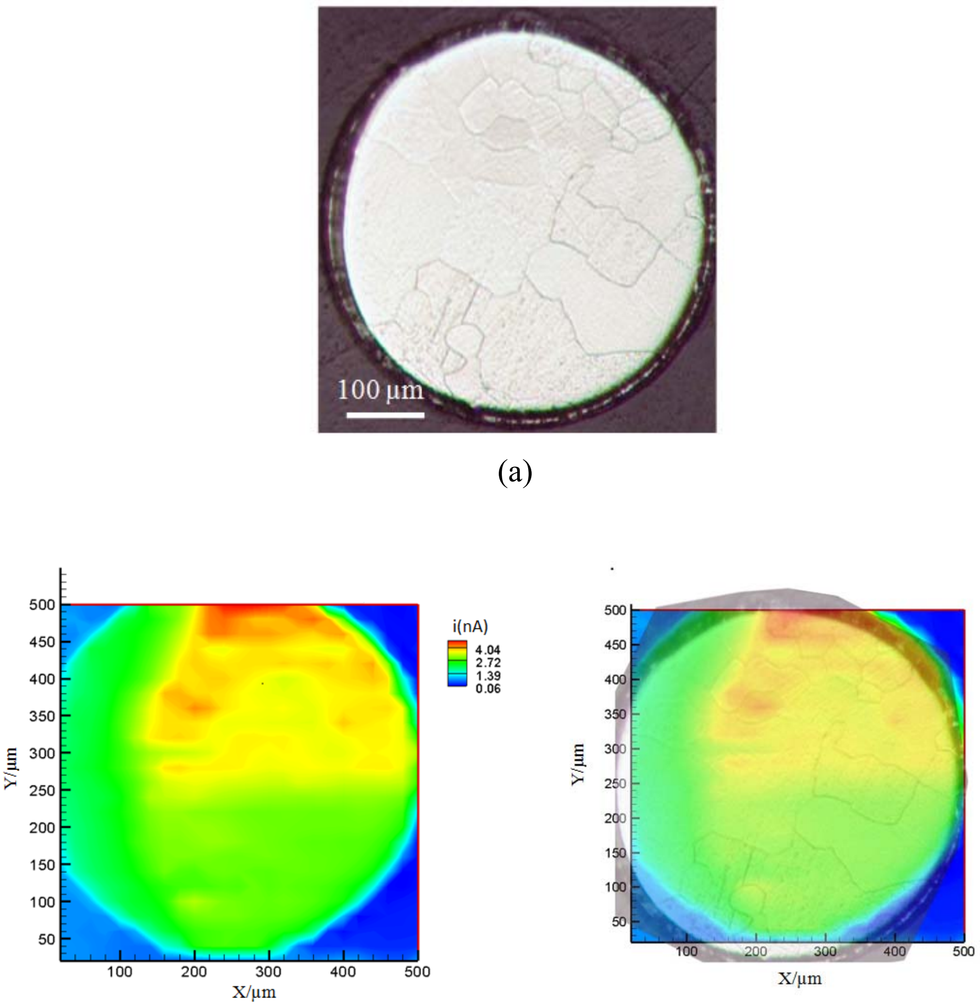

(a)

(b) (c)

Figure 4.12 Optical micrographs and SECM images of Pt Sub #W.

Note: (a) Optical micrograph of Pt Sub #W. (b) SECM image obtained in 1.25 mM $DMAFc^+$ + 10 mM sodium borate solution with a 10 µm diam Pt tip at a tip-substrate separation of 1 µm. E_{tip} = +0.7 V, E_{sub} = +0.1 V vs. Ag/AgCl. The scan rate is 100 µm/s. (c) An overlay of semitransparent SECM image on optical image. Both pictures were rotated to the same orientation.

4.3.3.2 Correlation between the Structure and Reactivity of Pt Single-Crystal Catalysts

Figure 4.13a shows an optical micrograph of Pt Sub #N. The area scanned by SECM on the Pt substrate surface is marked by the black square. The overlay of the semitransparent SECM image on the optical image in Figure 4.13c indicates that the electrochemical features in Figure 4.13b are closely correlated with the platinum crystallite domains.

An EBSD IPF map of Pt Sub #N is shown in Figure 4.14 with red, green, and blue colors assigned to <100>‖ND, <110>‖ND, and <111>‖ND grains, where the grain orientation is parallel to the surface normal direction. As described in Chapter 1, all the grains on the polycrystalline platinum substrate can be ascribed to three types based on their coded color in the IPF map; with red, green, and blue colors representing (100), (110), and (111) orientations plus a misorientation tolerance.

The images shown in Figure 4.15 clearly indicate the association between the surface catalytic activity of the HOR (from SECM current map) and crystallographic orientations (from EBSD image) of the Pt substrate surface. Figure 4.15a shows the pattern of electrocatalytic activity of Pt pseudo-single-crystal electrodes at the Pt substrate surface. Figure 4.15b exhibits the corresponding crystallographic orientation of each platinum crystallite domain in the same scanned area as the one shown in Figure 4.15a. Comparing Figure 4.15a and b, it is evident that the high catalytic activity regions towards the HOR are Pt(111) and Pt(110) planes, while Pt(100) planes show relatively low electrocatalytic activity. These results are not exactly consistent with the order of activity in HOR obtained by other researchers using low-index single-crystal electrodes. Marković et al. discovered that the order of the low-index single-crystal electrode increased in the sequence (111) < (100) < (110) for HOR in both alkaline and acid solution. Conway et al. derived the order of HOR activity to be (100) < (111) < (110).[23-24, 42,56-57,126-128]

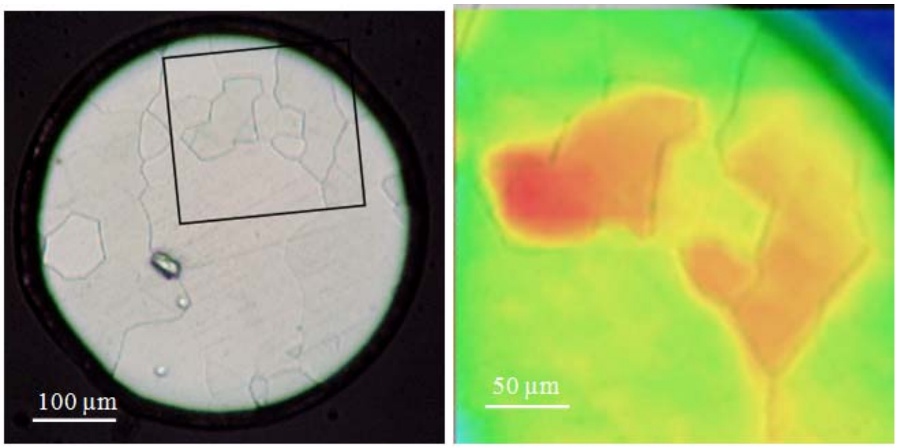

(a) (b)

Figure 4.13 Optical micrograph (a) of Pt Sub #N and the overlay (b) of HOR image (from Figure 4.11b) on the optical image of the area marked by the black square in panel (a).

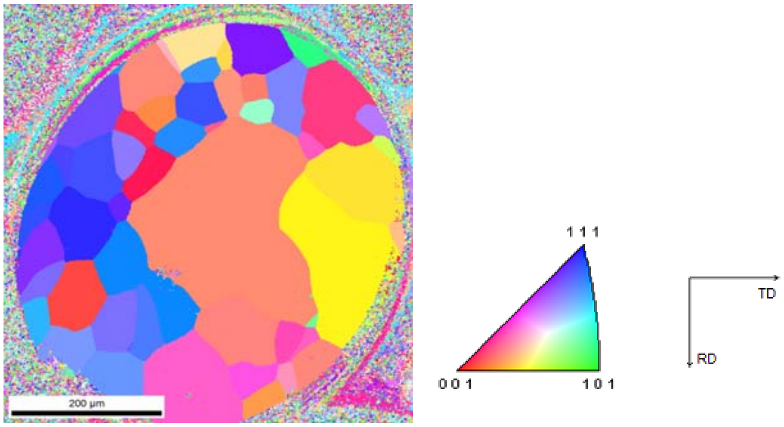

Figure 4.14 EBSD inverse pole figure (IPF) map of Pt substrate #N.

Note: The typical color triangle represents the normal direction (ND). EBSD step size is 1 µm.

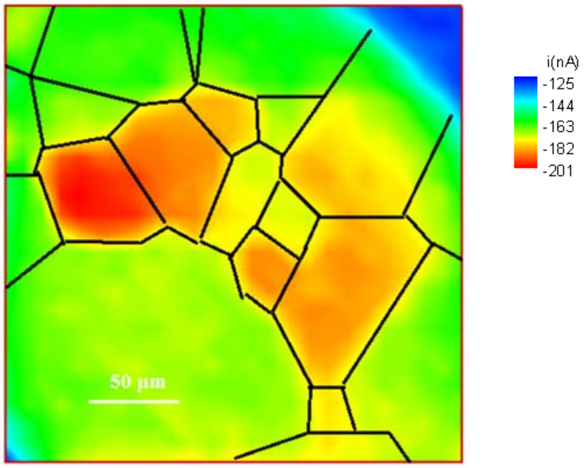

(a)

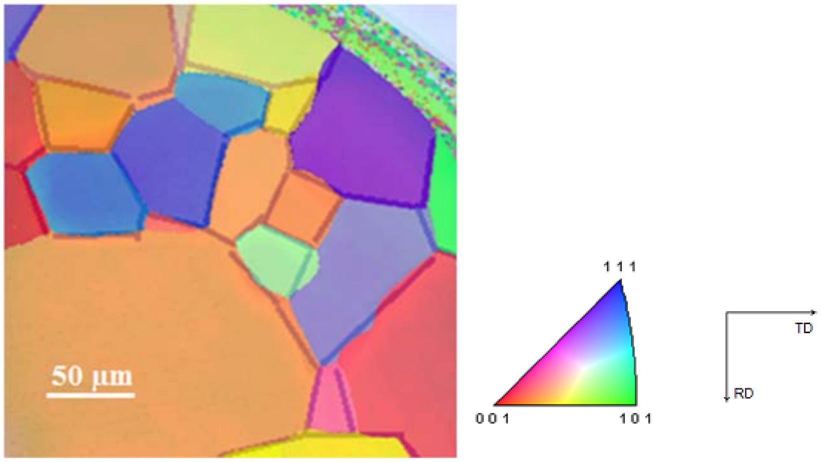

(b)

Figure 4.15 SECM current map (a) of polycrystalline Pt Sub #N for HOR with grain boundaries drawn (data from Figure 4.13a) and a composite image (b) showing a transparent overlay of the semitransparent EBSD map on the SECM current map in panel (a).

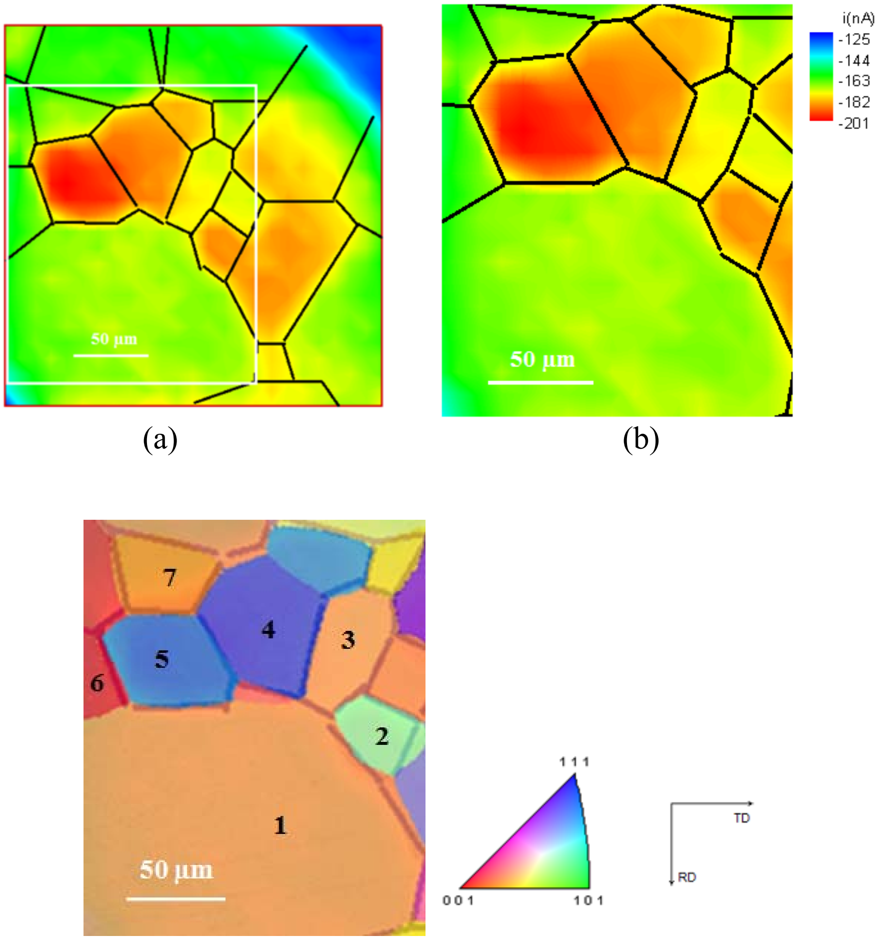

(a)

(b)

(c)

Figure 4.16 SECM current maps and EBSD IPF map of Pt Sub #N.

Note: (a) SECM image with grain boundaries drawn. (b) SECM image of selected area marked by the white square in panel (a). (c) An overlay of the semitransparent EBSD map on the SECM current map.

To explain the difference between our results and the reported findings, the structure-activity relationship of several selected Pt single-crystal domains was investigated. Figure 4.16a shows a SECM current map of one area of the polycrystalline platinum surface scanned at −0.75V vs. MSE. The SECM current map of the delimited area for further structure-activity relationship investigation is shown in Figure 4.16b, and the corresponding overlay of the EBSD image and SECM images in Figure 4.16c. Seven grains with different activity for the HOR in the SECM current map are labeled in Figure 4.16c. The relative catalytic activity of these platinum crystallites is in the order of grain #5 > #4 > #2 > #3 > #1 > #7 > #6 based on the magnitude of the corresponding HOR feedback current.

Comparing the EBSD IPF and SECM maps, it can be seen that planes with (111) orientation (Grains #4, #5) or (100) orientation (Grains #1, #3, #6, #7) have different activity. The reason for this is that the platinum single-crystal domains produced by electrolytic etching on polycrystalline platinum substrate are not true basal low-index planes, but actually high-index surfaces with (111), (110), and (100) representing the terrace orientation of all the grains. Table 4.1 lists the exact Miller indices for each grain calculated from the Euler angles (φ1, Φ, φ2) obtained in EBSD using conversion software (TexTools).

Since the notation for each single-crystal platinum grain can be simplified due to symmetry[19], an equivalent notation is used to describe the seven selected grains. Most of the seven planes have stepped surfaces except grain #2, which has a mixed terrace, step, and kink structure. Grains #4 and #5 have five-atom-wide terraces with (111) symmetry, but with a different step symmetry. Grain #4 has a monatomic (100) step while grain #5 has one-atom high (110)-oriented step sites. With different orientations for step sites, it is evident that grain #5 with (110) step sites exhibits higher catalytic activity than grain #4, as indicated by the color contrast of the HOR feedback current in the SECM current map (high tip current shows an intense red color). Moreover, the same behavior can be observed in grains with a (100) terrace. The grain without any (110)-orientation step site (grain #6) has the lowest electrocatalytic activity for the HOR. Notably, a clear correlation is determined between the increase in HOR activity and step-site density on a (100) base orientation. The order is as follows: (100) < (510) [= 5(100) × (110)] < (410) [=4(100) × (110)] < (310) [=3(100) × (110)]. These grains all have the same terrace orientation, which is (100). As the width of the terrace increases, the step atom density of the high-index grain becomes relatively low, and the corresponding catalytic activity of this grain decreases. The grain that does not have a step plane shows the lowest catalytic activity among the four grains (510), (410), (310), and (100). Therefore, the (110) orientation is ascribed to the variation of surface electrocatalytic current for the grains with the same base orientation.

Table 4.1 Crystallographic orientations of single-crystal platinum grains in Figure 4.16c

Grain #	Euler angles (φ1, Φ, φ2)	Exact Miller Index (hkl) [uwv]	Equivalent notation	Coded Color	Description
1	340.8, 15.4, 18	(0,1,4) [1,0,0]	(410)	red	(S)-[4(100) × (110)]
2	201.4, 38.1, 162.4	(1,-3,4) [4,0,-1]	(431)	green	Kinked surface (110) character
3	78, 17.2, 288.4	(-1,0,3) [3,0,1]	(310)	red	(S)-[3(100) × (110)]
4	231.7, 50.4, 139.3	(2,-2,3) [3,0,-2]	(322)	blue	(S)-[5(111) × (100)]
5	131.8, 49.8, 235.4	(-3,2,3) [3,-1,2]	(332)	blue	(S)-[5(111) × (110)]
6	314.6, 5.9, 47.8	(0,0,1) [1,0,0]	(100)	red	Basal plane
7	102.5, 12.2, 279.4	(-1,0,5) [4,-2,1]	(510)	red	(S)-[5(100) × (110)]

The surface catalytic activity for the HOR is in the order of (332) < (100) < (510) < (410) < (310) < (431) < (322) < (332) for the selected seven grains. Briefly, the surface catalytic activities of grains are in an order of Pt(100) < Pt(110) < Pt(111) where low Miller indices represent the terrace orientations for the high-index surfaces. The enhanced catalytic activity is closely correlated with the preferential adsorption sites for hydrogen atom at the step atoms.[7]

4.3.4 Effect of Substrate Potential

4.3.4.1 Influence of Substrate Potential on Electrocatalytic Activity Imaging of Pt Single-Crystal Electrodes

To investigate further the kinetic and mechanistic information of the HOR on Pt single crystallites, the area in Figure 4.15 was scanned at different substrate potentials, as shown in Figure 4.17. The rate of the HOR at different platinum grains is indicated by the magnitude of the tip current and the color contrast of the current contour images. For the correlation between surface catalytic activity and crystal structure information, the EBSD IPF map with all the grains labeled is shown in Figure 4.18. The crystallographic orientations of all the platinum single-crystal domains are listed in Table 4.2.

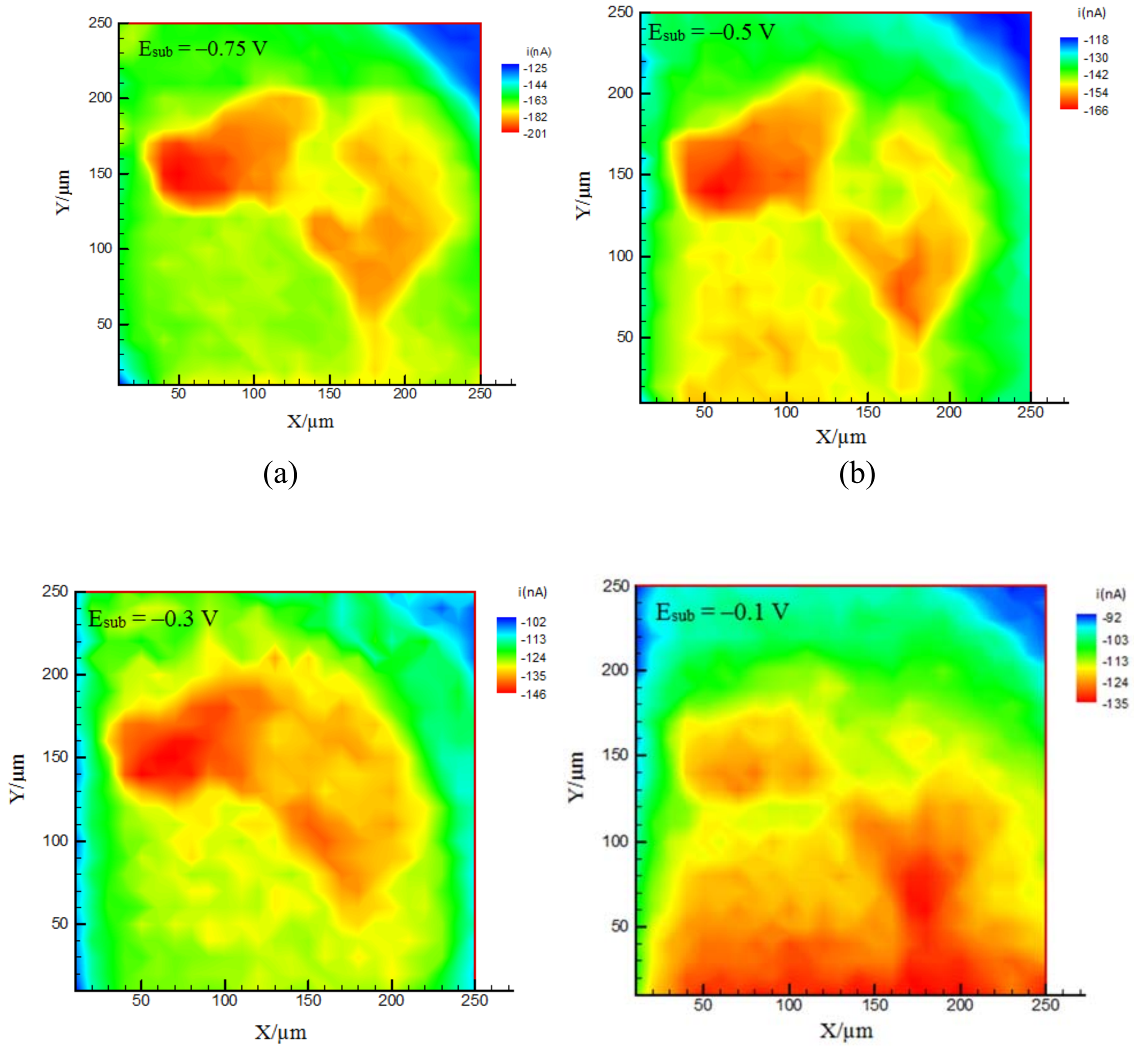

(a) (b)

(c) (d)

Figure 4.17 SECM images of the same area of platinum substrate biased toward HOR at different potentials: (a) −0.75 V, (b) −0.5 V, (c) −0.3 V, (d) −0.1 V, (e) +0.1 V, (f) +0.3 V (g) +0.6 V, (h) +0.8 V (vs. MSE).

Note: The tip-substrate distance was 5 µm. The SECM image was obtained in 10 mM H_2SO_4 and 0.1 M K_2SO_4 solution with a 10 µm diam Pt tip (i_{bulk} = −130 nA). E_{tip} = −1.5 V. Scan rate is 100 µm/s.

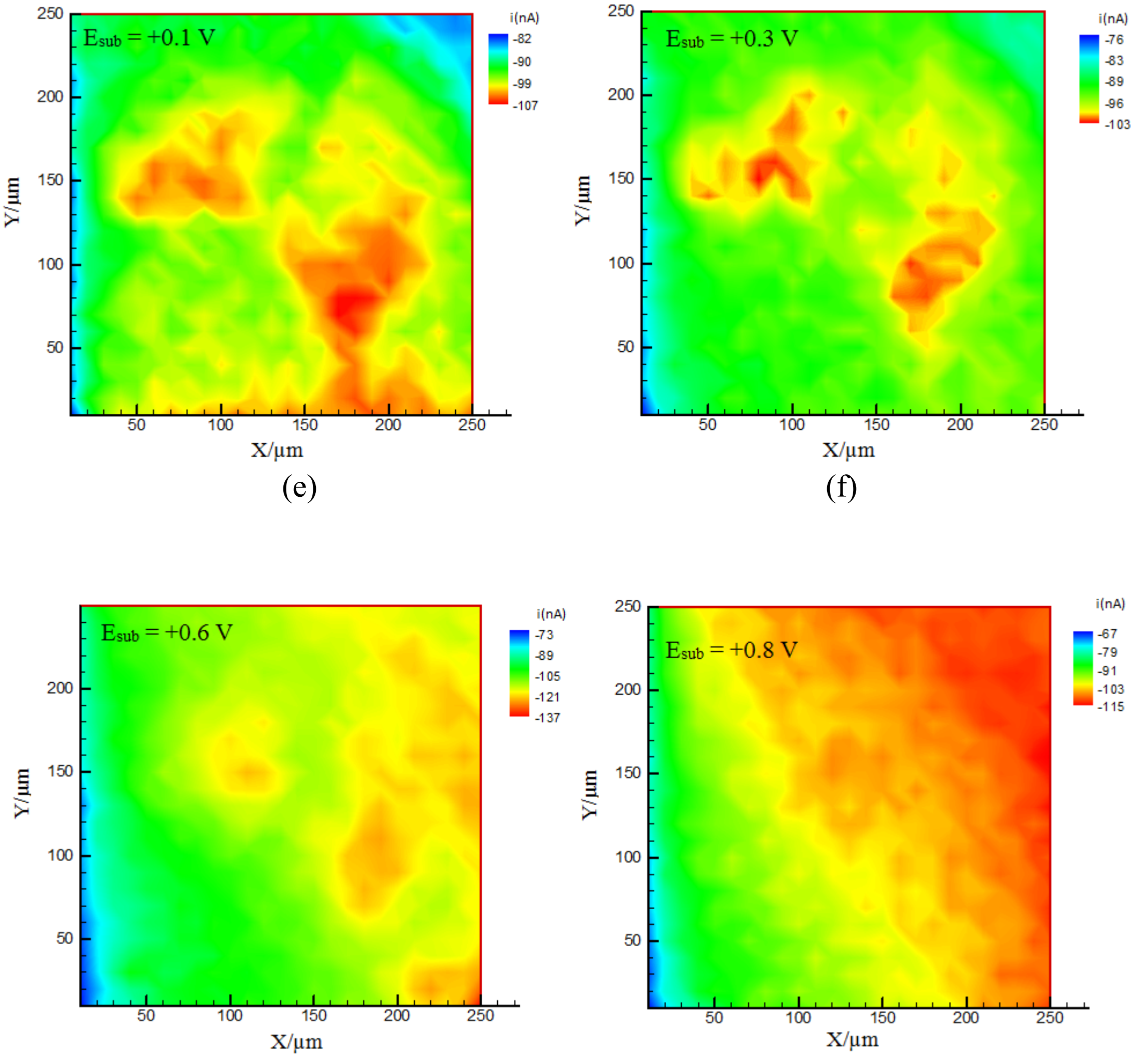

(e) (f)

(g) (h)

Figure 4.17 Continued.

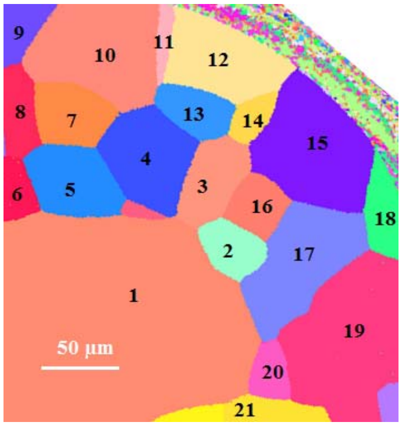

Figure 4.18 EBSD IPF map with grain number labeled.

Table 4.2 Crystallographic orientations of single-crystal platinum grains in Figure 4.18

Grain #	Exact Miller Index (hkl)[uwv]	Equivalent notation	Coded Color	Description
1	(0,1,4)[1,0,0]	(410)	red	(S)-[4(100) × (110)]
2	(1,-3,4)[4,0,-1]	(431)	green	(110) character
3	(-1,0,3)[3,0,1]	(310)	red	(S)-[3(100) × (110)]
4	(2,-2,3)[3,0,-2]	(322)	blue	(S)-[5(111) × (100)]
5	(-3,2,3)[3,-1,2]	(332)	blue	(S)-[5(111) × (110)]
6	(0,0,1)[1,0,0]	(100)	red	Basal Plane
7	(-1,0,5)[4,-2,1]	(510)	red	(S)-[5(100) × (110)]
8	(0,0,1)[6,-1,0]	(100)	red	Basal Plane
9	(2,2,3)[2,2,-3]	(322)	blue	(S)-[5(111) × (100)]
10	(0,1,4)[12,3,-2]	(410)	red	(S)-[4(100) × (110)]
11	(1,2,5)[3,1,-1]	(521)	red	(100) character
12	(0,1,2)[6,3,-2]	(210)	yellow	(S)-[2(100) × (110)] (S)-[2(110) × (100)]
13	(3,-2,3)[3,1,-3]	(332)	blue	(S)-[5(111) × (110)]
14	(0,1,3)[4,2,-1]	(310)	yellow	(S)-[3(100) × (110)]
15	(2,-2,3)[3,-2,1]	(322)	blue	(S)-[5(111) × (100)]
16	(-1,0,4)[4,0,1]	(410)	red	(S)-[4(100) × (110)]
17	(3,-2,4)[4,4,-1]	(432)	blue	(111) character
18	(1,-6,6)[6,0,-1]	(661)	green	(110) character
19	(-3,2,15)[5,0,1]	(15,3,2)	red	(100) character
20	(-2,-8,3)[5,-1,0]	(832)	red	(100) character
21	(0,1,3)[4,1,0]	(310)	yellow	(S)-[3(100) × (110)]

Figure 4.20 shows the SECM images obtained in the same area of Pt Sub #N at different bias potentials from −0.75 V to +0.8 V. The color contrast of tip current at Pt grain #2 is slightly lower compared to other grains in Figure 4.17b than that shown in Figure 4.17a. This suggests that the surface activity has decreased at grain #2, which possesses a (110) character, as the substrate potential increases from −0.75 V to −0.5 V. When a potential of −0.3 V was applied, the color contrast between planes with (111) and (100) terrace has significantly decreased as the differences in tip current recorded at these regions become smaller, as illustrated in Figure 4.17c. For example, the tip current at both grain #15 and grain #16 has decreased as substrate potential changes from −0.5 V to −0.3 V, as well as the color contrast between the two grains. As seen in the legend, the absolute tip current at these two grains is very close. The large variation in electrocatalytic behavior of Pt pseudo-single-crystal electrodes from Figure 4.17a-c is most likely due to the weakly bisulfate anion adsorption/desorption at the (110) and (110) orientation sites, which has an blocking effect for the HOR.[24] It was reported that the potential regions of bisulfate adsorption for Pt(110) and Pt (100) single-crystal electrodes were between −0.59 V and −0.265 V, and between −0.39 V and −0.24 V vs. MSE, respectively.[25,124,129] This will explain the decrease in the rate of the HOR at grains with (110) character (e.g. grain #2) as the biased substrate potential changes from −0.75 V to −0.5 V, and at grains with (100) step orientations (e.g. grain #15 [Pt(322) = 5(111) × (100)]). Even though the high-index surfaces coded in red color on IPF map also have (100) orientation, the influence of the bisulfate adsorption on grains having (100) step sites apparently is greater than on other surfaces. The effect of anion adsorption on step sites can be further seen in Figure 4.17d. It is observed that the tip current decreases dramatically at grain #13 [Pt(332) = 5(111) × (110)] and grain #15 [Pt(322) = 5(111) × (100)] at a substrate potential of −0.1 V, while grain #1 [Pt(410) = 4(100) × (110)] appears to be very active for the HOR. After careful comparison between EBSD and SECM current maps (Figure 4.17d), it seems that grains with (111) terrace orientations undergo a large decline in the rate of HOR. These phenomena are likely resulting from bisulfate anion adsorption at a (111) orientation since the adsorption of bisulfate anion at a (111) place takes place in a potential range between −0.24 V and −0.04 V (vs. MSE).[24] These results show that the blocking effect of the adsorption of bisulfate anion species at either terrace or step sites at the high-index surfaces, indicating the complicated behavior of high-index single-crystal electrodes toward the HOR at negative potentials vs. MSE. When the substrate potential is changed to +0.1 V, surface oxides (termed as Pt/O) begin to form at (100) grains. These species can fill in the surface lattice sites and inhibit the catalytic activity of Pt [25,77,129-130], causing a large decrease in the electrocatalytic activity of (100) grains for the HOR compared to that of (111) grains.[24-25,78] At +0.3V, the oxide film formation occurs at the whole polycrystalline Pt substrate electrode surface, causing the differences in the inhibition effect of Pt/O species to become small among Pt single-crystal grains. Therefore, a similar current contour image (Figure 4.17f) as the one shown in Figure 4.17a is obtained. Even though the magnitude of tip current has declined as the substrate potential increases, grains with (111) base orientation (for example, grain #4 and #5) still possess the highest catalytic activity toward the HOR compared with other grains, as suggested by SECM current contour images in Figures 4.17a-f.

In Figure 4.17g, negative feedback behavior starts to appear near the surrounding epoxy region and only a few domains (grain #4 and #17) having (111) base orientation remain active for the HOR. This suggests most of the surface is covered by Pt/O species which shields the Pt sites for hydrogen adsorption and desorption in the HOR.[131] Note, grain #4 [Pt(332)= 5(111) × (100)] hold the highest activity while the substrate potential increases from −0.75 V to +0.6 V. At +0.8 V (Figure 4.27h), the electrochemical features of the platinum single crystal surface are gone, implying the catalytic activity of the Pt substrate electrode is completely lost.

One may expect the rate of the HOR to increase with more positive substrate potentials. However, the experimental results show the oxidation reaction rate decreases as the substrate potential goes more positive rather than the expected increase. This further confirms the rate-determining step for the HOR is the initial adsorption of molecular hydrogen reaction on the Pt surface rather than the charge transfer reaction.[44] In addition, the significant variation in tip current between SECM contour images indicates that the catalytic activity behavior of Pt pseudo-single-crystal electrodes is evidently potential-dependent.

It should be noticed that the tip current decreases as the biased substrate potential increases from −0.75 V to +0.8 V as shown in Figures 4.17a to h. This reflects the decreasing rate of the HOR as substrate potential increases due to the blocking effect of platinum oxide growth for the HOR at the Pt substrate surface.

To further illustrate the potential dependent behavior of the HOR catalytic activity at the platinum surface and to show that the decrease in signal was not due to a time-dependent electrode passivation, an SECM scan was collected in the same area of the platinum substrate surface as the potential is returned to potentials of +0.1 V and −0.5 V as shown in Figure 4.19. It can be seen that the two SECM contour images are very close to the ones collected at the same potential in Figures 4.17e and b. Moreover, the overall tip current increases as the substrate potential is biased at more negative potential from +0.1 V to −0.5 V in Figure 4.19. This suggests the reversible reduction of Pt/O species to reveal active free Pt sites for the HOR.[48,77]

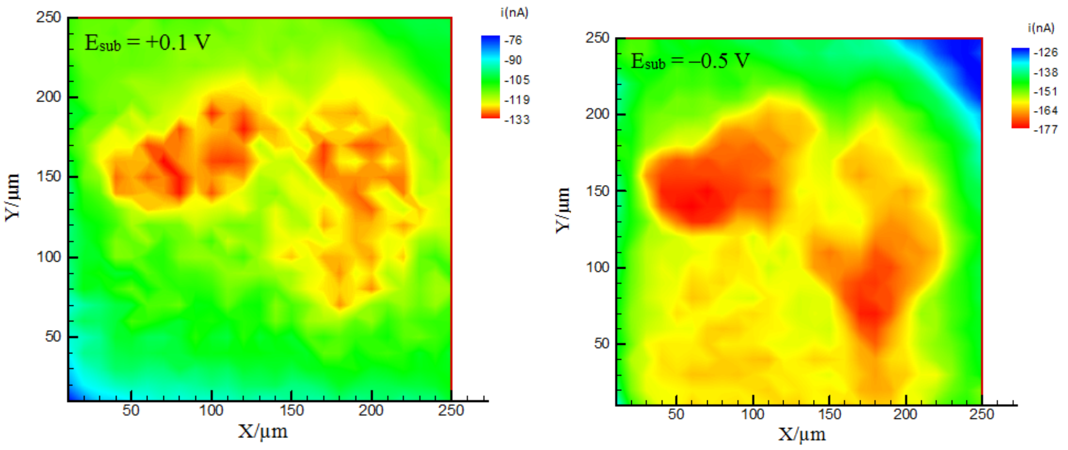

(a) (b)

Figure 4.19 SECM images of the same area of platinum substrate biased toward HOR at a potential of (a) +0.1 V, (b) −0.5 V under the same SECM imaging experiment conditions.

Overall, the observations in SECM imaging experiments at different substrate bias potentials demonstrate a more direct and effective characterization of the catalytic activity of Pt crystal catalysts with different crystallographic orientations in acidic media. A potential-dependent catalytic behavior of Pt single-crystal surfaces is demonstrated. Grains with (111) terrace orientation remain active over a large potential range. These images also verify that the threshold potential of bisulfate anion adsorption at Pt single-crystal electrode increases in the order of Pt(110) < Pt(100) < Pt(111).[25,124,129]

4.3.4.2 Influence of Substrate Potential on Tip Current at Various Pt Single-Crystallite Surfaces

The effect of substrate potential on the tip current was examined at various locations on Pt single crystallite surfaces. The seven grains marked in Figure 4.16 were selected for this study. The tip current was extracted from five different spots at each designated grain surface on the SECM current maps obtained at different substrate potentials (−0.75 V, −0.5 V, −0.3 V, −0.1 V, +0.1 V, +0.3 V, +0.6 V, and +0.8 V). The average tip current of the five extracted tip currents for each grain was plotted versus substrate potential in Figure 4.20. In the current-voltage (*I-E*) profile, the data for region R is collected over the surrounding nonactive epoxy near the edge of the Pt disk electrode to serve as a reference for the seven grains. In the potential region between −0.75 V and +0.3 V, the tip current decreases in magnitude as the substrate potential becomes more positive, showing a potential-dependent behavior. At a potential of +0.6 V and +0.8 V, the slight increase in tip current can be ascribed to the oxygen evolution which causes a decrease in pH at the local substrate surface.[77] In addition, the local concentration change at the Pt substrate and the close position near the conductive Pt disk electrode surface may also contribute in the tip current increase. Since the catalytic activity of the platinum electrode surface becomes very low at potential more positive than +0.6 V, as shown in the corresponding SECM current map in Figure 4.17g, the resulting tip current mostly reflects the surface topography. The current-potential plots in Figure 4.20 exhibit a grain-dependent behavior of Pt grains with each single crystal domain displaying a different current response from each other as the substrate potential varies. The results further confirm the discussions of the SECM imaging scan results shown in Figure 4.17 in a quantitative way. The catalytic activity of the seven grains is in the order of (111) > (110) > (100) where Miller indices represent the terrace orientations of the grain surface. It is worth noticing that the tip current in the *I-E* curve for region R in Figure 4.22 decreases with an increasing potential, which is possibly due to a local concentration change because the tip is positioned near the Pt disk electrode surface.

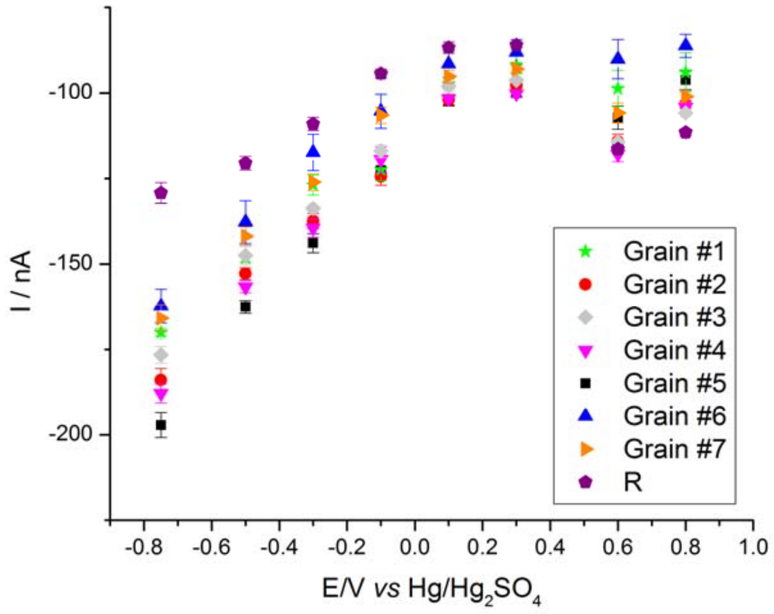

Figure 4.20 Current- potential (*I-E*) profiles of tip current as a function of the bias substrate potentials for seven grains labeled in Figure 4.16c.

Note: R is the reference point on the surrounding epoxy surface. The error bars indicate one standard deviation for *n* > 5 measurements.

For comparison, the tip current of grain # 5, # 2, #1 ($i = i_5$, $i_{2.}$ i_1) are plotted against the tip current of region R (i_R) as a function of substrate potential in Figure 4.21a. The current difference ($\Delta i = i - i_R$) versus different substrate potentials is illustrated in Figure 4.21b. The correlation between the decrease in current (Δi) with an increasing substrate potential is the same for Δi in *I-E* plots after subtracting i_R as that in Figure 4.21a. Figure 4.21c shows the current differences between the tip current of grain #5, #2, #1. It is evident that the overall catalytic activity of the three grains is in the order of grain #5 > #2 > #1 based on the magnitude of Δi. Note that the smallest current difference among the three grains is at a potential of +0.1 V. The current difference becomes larger at more positive potentials than +0.1 V until negative feedback begins to dominate at +0.6 V. This is probably due to the onset of overall oxide formation across the Pt substrate surface at +0.1 V, and the rate of oxide formation varies upon the orientation of the grains, causing the small current differences at +0.1 V and larger current difference at more positive potentials.[25,131 132]

Overall, the results show that the electrocatalytic activity of grain #5, #2, #1 is in the order (111) > (110) > (100), where Miller indices represent the grain terrace orientation. This further confirms the grain-dependent catalytic activity of platinum single crystal domains on polycrystalline platinum surface as determined by the SECM imaging experimental results. Four single crystallites with orientation Pt(310), Pt(410), Pt(510), and Pt(100) were selected to represent grains with the same terrace and step symmetry but having different step density. The rate of the HOR can be readily examined by tip current at these high-index surfaces in Figure 4.22.

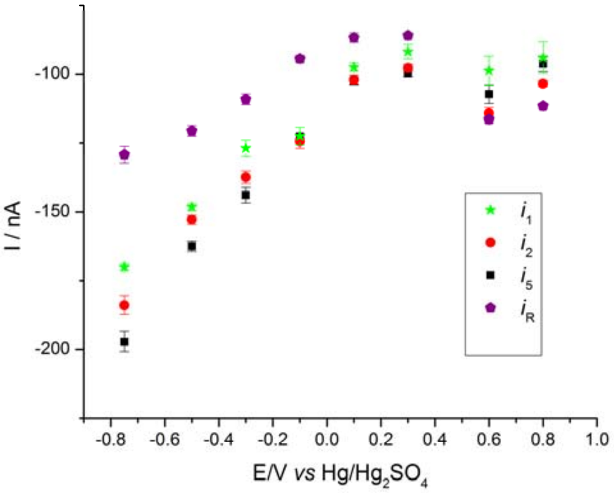

(a)

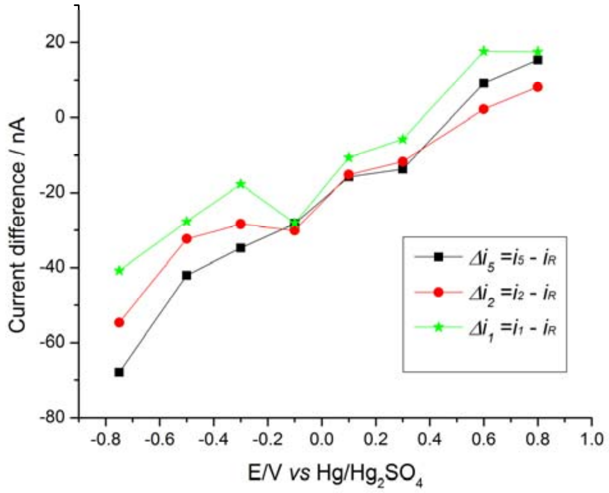

(b)

Figure 4.21 *I-E* profiles of grain #5, #2, and #1.

Note: (a) *I-E* profiles of tip current as a function of the bias substrate potentials for grain #5, #2, and #1 are shown by solid symbols on solid lines. R is the reference point on the surrounding epoxy surface. (b) The current difference ($\Delta i = i - i_R$) between each grain and the reference region is plotted in the same panel with solid symbols on solid lines. (c) *I-E* curves of tip current difference between grain #5, #2, and #1.

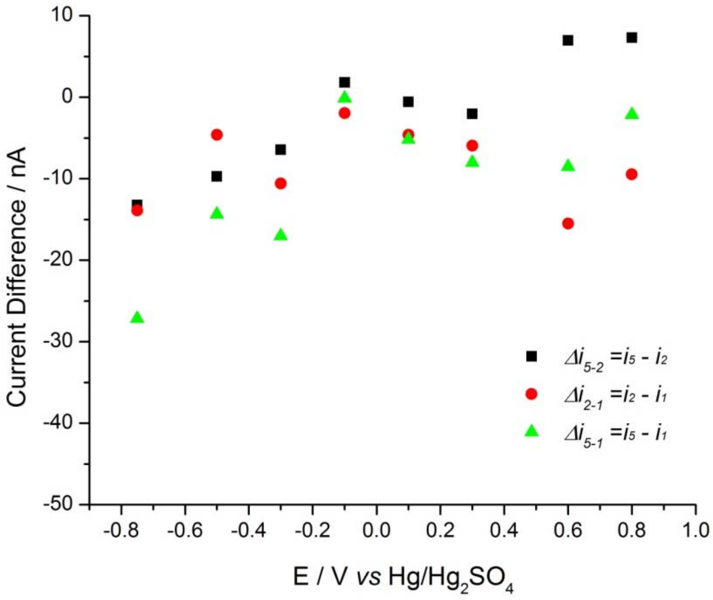

(c)

Figure 4.21 Continued

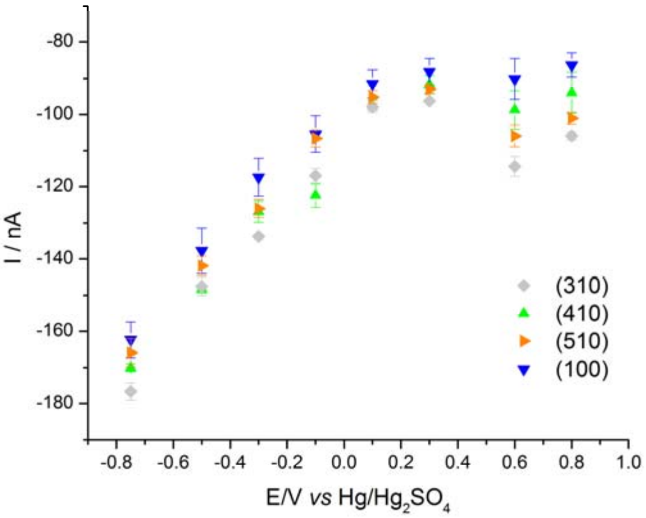

Figure 4.22 *I-E* profiles of tip current as a function of the bias substrate potentials for four single crystallites Pt(310), Pt(410), Pt(510), and Pt(100).

The *I-E* plots in Figure 4.22 show that the order of catalytic activity for these four grains are Pt(310) > Pt(410) > Pt(510) > Pt(100) only when the substrate is biased at −0.75 V. The activities of these grains varies upon the change of substrate potential at potential more positive than −0.75 V, suggesting the strong substrate potential-dependent behavior at these grains. The electrocatalytic activity of Pt(310) has dramatically changed between −0.5 V and +0.3 V compared with the other grains. Since Pt(310) has the largest step atom density among the four selected grains, the large drop in tip current with potential change compared with other grains, indicates the blocking effect caused by the Pt/O species at (110) planes greatly affect the rate of the HOR. The results further prove the (110) plane is the more active site for the HOR compared with (100) planes.

4.3.4.3 Quantitative Analysis of Localized Surface Reactivity at Different Substrate Potentials on Various Grains by SECM Approach Curves

SECM approach curve experiments were performed to measure the rate constants for the HOR at platinum single crystallite surfaces with different crystallographic orientations. In SECM approach curve experiments, the SECM UME probe is set at a potential where diffusion-limited tip current can be reached and then the tip electrode is moved vertically toward the area of interest on the substrate surface. The tip current, i_T, plotted versus tip-sample separation distance d is called an approach curve. By fitting the experimental approach curves with SECM theoretical expressions, the rate constant for heterogeneous electron transfer on the substrate can be extracted.[59]

The following approximate expressions have been proposed by Lefrou etc. al.[133]

$$Ni_T^{cond} \approx \alpha(R_g) + \frac{1}{\beta(R_g)}\frac{\pi}{4\tan^{-1}L} + \left(1 - \alpha(R_g) - \frac{1}{2\beta(R_g)}\right)\frac{2}{\pi}\tan^{-1}L \tag{4.1}$$

$$\alpha = \ln 2 + \ln 2\left(1 - \frac{2}{\pi}\cos^{-1}\frac{1}{R_g}\right) - \ln 2\left[1 - \left(\frac{2}{\pi}\cos^{-1}\frac{1}{R_g}\right)^2\right] \tag{4.2}$$

$$\beta = 1 + \frac{0.23}{(R_\mathrm{g}^3 - 0.81)^{0.36}} \tag{4.3}$$

$$Ni_T^{ins} \approx \left[\frac{\frac{2.08}{R_\mathrm{g}^{0.358}}\left(L - \frac{0.145}{R_g}\right) + 1.585}{\frac{2.08}{R_\mathrm{g}^{0.358}}(L + 0.0023R_g) + 1.57 + \frac{\ln R_g}{L} + \frac{2}{\pi R_g}\ln(1 + \frac{\pi R_g}{2L})}\right] \tag{4.4}$$

$$Ni_T(L, R_g, \kappa) \approx Ni_T^{cond}\left(L + \frac{1}{\kappa}, R_g\right) + \frac{Ni_T^{ins}(L, R_g) - 1}{(1 + 2.47R_\mathrm{g}^{0.31}L\kappa)(1 + L^{0.006R_g + 0.113}\kappa^{-0.0236R_g + 0.91})} \tag{4.5}$$

Where Ni_T is the normalized tip current, which is defined as the ratio of tip current by the diffusion-controlled tip current ($Ni_T = \frac{i_\mathrm{T}}{i_{\mathrm{T},\infty}}$). Ni_T^{cond} and Ni_T^{ins} are normalized tip current over conductive and insulating surfaces at a normalized distance *L*. *L* = *d/a*, where *d* is the tip-substrate separation distance and *a* is the radius of the microdisk. R_g (= r_glass/a) is the ratio of the radius of the disk electrode to the radius of the metal wire, where r_glass is the radius of the electrode glass sheath, *a* is the radius of the electrode. *κ* is a dimensionless kinetic parameter, defined as κ = *kd*/*D*, where *k* is the apparent heterogeneous rate constant (in cm/s), and *D* is the diffusion coefficient.

An advantages of these approximation expressions are the inclusion of both R_g and *L* as analytical variables (instead of simply *L,* previously), a wide valid range of parameters and variables (any $R_g < 20$, L > 0.1 and any κ), and quantitatively accurate SECM data treatments of first-order irreversible substrate kinetics compared to previous models.[134-137] Thus, these equations were used to measure the rate constant of the HOR in this study:

In the present study, the approach curves were obtained by setting the Pt tip potential at −1.5 V while the substrate potential is biased at different values. A series of approach curves were recorded as the tip approached different platinum single crystal domains (grain #5, #2, and #1 are selected for this study) at the applied potential from −0.5 V to +0.2 V.

Figure 4.23 shows the resulting approach curves at different substrate potentials. The black curve corresponds to the theoretical curve for a diffusion-controlled reaction (conductor behavior) in Figures 4.23a to d, and for pure negative feedback (insulator behavior) in 4.23e and h. The approach curves of grain #5, #2, and #1 in Figure 4.23a almost overlap the theoretical one, indicating a fast heterogeneous reaction rate at −0.5 V. When the substrate is biased at −0.3 V, the curves of grain #5, #2, and #1 show a large deviation from the theoretical curve of a conductor. Compared to the corresponding curves obtained at −0.5 V (Figure 4.23a), the heterogeneous reaction rate for all the three grains has dramatically decreased at this potential. The reaction rate decreases further for grains #5, #2, and #1 at a potential of −0.1 V. Although the rate for all three grains continues to decrease at 0 V, it seems the order of the rate stays as grain #5 > #2 > #1. In Figure 4.23e and h, the grains exhibit negative feedback behavior with a decreasing rate as the substrate potential biased from 0.1 V to 0.2 V, but still possess a relatively high HOR rate compared with pure insulator behavior.

These approach curves results are in accordance with previous discussed SECM imaging results and current-voltage (*I-E*) plots, and clearly illustrate the potential-dependent behavior of platinum single crystal domains for the HOR. The order for the heterogeneous reaction rate of the selected grains is grain #5 > #2 > #1 throughout the studied potential range, as seen in Table 4.3. The rate constant for each crystal domain is determined by fitting the experimental to theoretical approach curves. The logarithm of the rate constants for grain #5, #2, and #1 are plotted as a function of the substrate potential. The measured rate constants for the three investigated grains show a similar trend as in Figure 4.24. The rate constant decreases with an increase of substrate potential between −0.5 V and 0.2 V.

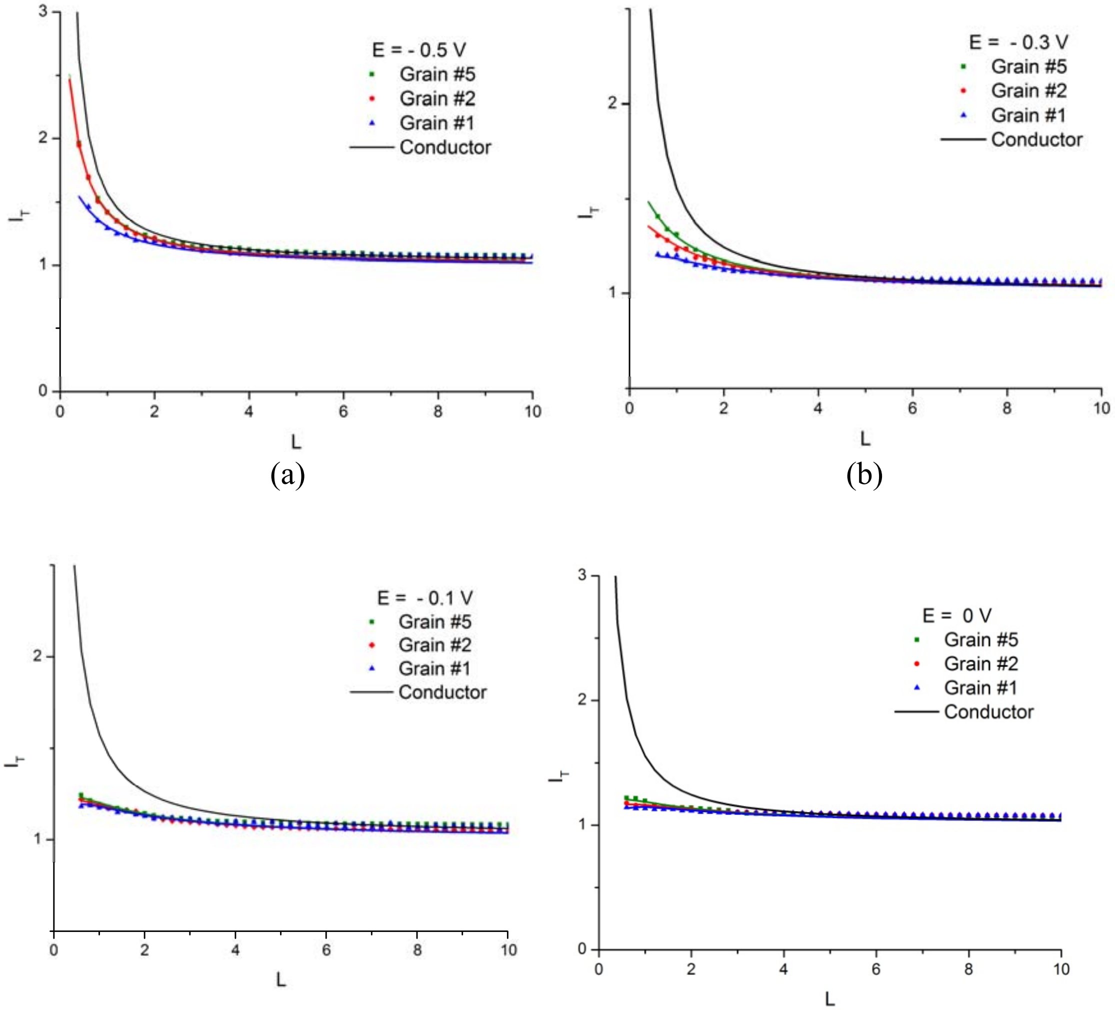

(a) (b)

(c) (d)

Figure 4.23 SECM approach curves toward grain #5 (green square), grain #2 (red circles) and grain #1 (blue diamond) on Pt substrate # N at substrate potentials between −0.5 V to 0.2 V.

Note: Solid colored lines represent best fits of the theoretical feedback response as a function of the heterogeneous rate constant at different potentials. The black lines correspond to theoretical approaching curves for either pure positive (conductor behavior) or pure negative (insulator behavior) feedback.

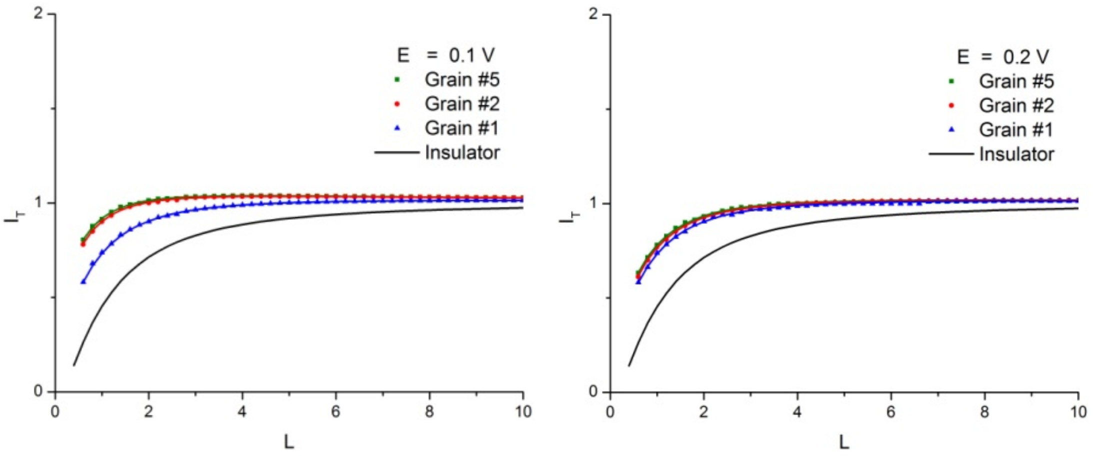

(e) (f)

Figure 4.23 Continued.

Table 4.3 The HOR rate of Pt pseudo-single-crystal electrodes at different substrate potentials

	Apparent reaction rate constant *k* (cm/s)		
E(V)	Grain #5	Grain #2	Grain #1
−0.5	6.58	4.61	0.26
−0.3	0.224	0.171	0.118
−0.1	0.132	0.125	0.115
0	0.118	0.103	9.21E-02
+0.1	3.16E-02	2.90E-02	1.05E-02
+0.2	1.45E-02	1.32E-02	9.7E-03

As is evident from Figure 4.24 the highest rate constant for the HOR in the studied potential range is obtained at −0.5 V, and decreases rapidly at −0.3 V for all three grains. From −0.1 V to 0.2 V, a plot of $\log_{10}k$ vs. substrate potential displays a linear relationship. When the potential is less than −0.5 V in the experiment, the behavior of Pt pseudo single crystal catalyst is kinetically controlled owing to the small value of the rate constant. Throughout the range of potential from −0.5 V to 0.2 V, grain #5 possess the highest rate constant toward the HOR, and grain #1 has the lowest rate constant. These results indicate that Pt stepped surfaces with (111) terraces have the highest electrocatalytic activity toward the HOR, surfaces with (100) terraces show the lowest reactivity, and grains with (110) character are intermediate.

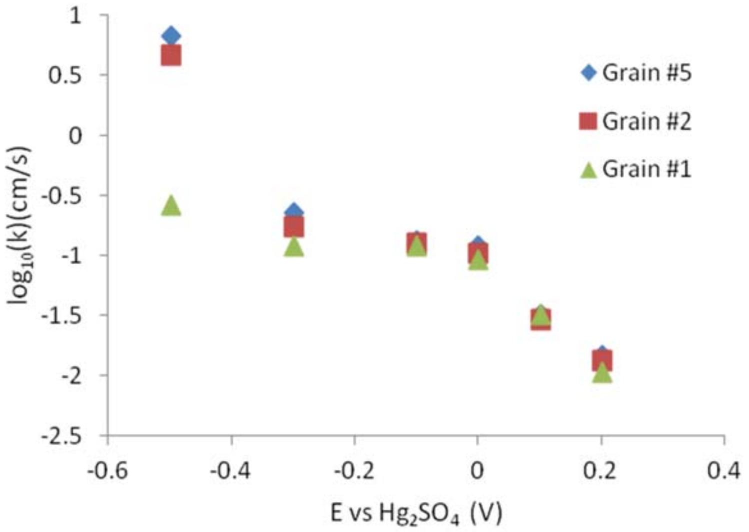

Figure 4.24 Logarithm of heterogeneous rate constant k at the surface of grain #5, #2, #1 with different substrate potentials.

4.4 Conclusions

In this chapter, the electrocatalysis of the anode reaction in PEMFCs, the hydrogen oxidation reaction (HOR) on Pt catalysts, was investigated in a proton/hydrogen mediator system. Both the ultramicroelectrode (UME) tip and the etched polycrystalline platinum substrate were characterized by cyclic voltammetry with $DMAFC^+/DMAFC^{2+}$ and H^+/H_2 redox couples, respectively. Appropriate potentials to bias both tip and substrate electrodes were found using cyclic voltammetry. A study of the effect of tip-sample distance in the SECM cell by SECM approach curves and SECM imaging experiments demonstrated the capability of SECM in positioning the tip over the substrate precisely and generating high resolution 2D and 3D scan images with vivid color contrast.

The topography contribution to the current response in SECM imaging scans obtained in a solution of 10 mM sulfuric acid and 0.1 M potassium sulfate was evaluated by the DMAFC^{+}/DMAFC^{2+} redox couple as a topography probe. Both electrochemical (SECM) and physical characterization (AFM) results indicate the topographic effects are minimal and they can be neglected under the experimental conditions.

SECM imaging scan results show a significant heterogeneity of electrocatalytic activity at platinum pseudo-single crystal electrode surfaces toward the hydrogen oxidation reaction. The correlation between SECM imaging results and the optical micrograph of the platinum substrate surface confirm that the pattern of the electrochemical features and the Pt electrode surface geometry are very well matched.

By comparing SECM current maps to EBSD images, the structure-reactivity relationship of pseudo-single-crystal electrodes can be obtained. The results show the structural sensitivity of platinum surfaces toward the HOR. The pseudo-single-crystal electrodes exhibit heterogeneity in catalytic activity with different potentials. It is found that the surface catalytic activity for the HOR is in the order of (332) < (100) < (510) < (410) < (310) < (431) < (322) < (332) for the seven selected grains with different crystallographic orientations. A Pt stepped surface with (111) terraces has the highest electrocatalytic activity toward the HOR, surfaces with (100) terraces shows the lowest reactivity, and grains with (110) character are in between. Moreover, it is observed that the presence of (110) steps on the high-index platinum surfaces with the same atomic width of (111) terrace affects the electrocatalytic activity of the surface to a certain degree, as indicated by the activity order of Pt(332) [=5(111) × (110)] > Pt(322) [=5(111) × (100)]. A dependence of electrocatalytic activity with step density is evident, with an activity order of Pt(310) > Pt(410) > Pt(510) > Pt(100) toward the HOR as step density decreases. The local reactivity of pseudo-single-crystal surfaces was quantitatively analyzed by fitting experimental SECM current-distance approach curves to theoretical analytical approximation expressions. The rate constants extracted from curve fitting for the HOR at different potentials are consistent with SECM imaging results. The HOR is under diffusion control at –0.5 V, and under kinetic control when the potential is more positive than –0.3 V.

Overall, the relationship of crystallographic orientations of pseudo-single-crystal electrodes and its corresponding electrocatalytic activity for HOR is successfully investigated by coupling SECM and EBSD, which proves that the proposed approach is very effective in studying structure-activity relationships of high-index polycrystalline electrode materials.

CHAPTER V

CONCLUSIONS

Traditional well-defined single-crystal electrodes have been used extensively for investigating the influence of surface structure on the electrochemical activity of metal electrodes. However, preparing low-index and high-index single crystal electrodes is very demanding. The methods for low-index single-crystal electrode fabrication, such as Clavilier's method and flame annealing approach,[25] requires expensive single-crystal materials requiring careful handling and orienting, cutting, and mechanical polishing processes which are very technically challenging and time-consuming.[138] The high-index single-crystal electrodes are also difficult to make, and they are hard to maintain as macroscopic single crystals due to high surface energy.[116]

Conventional electrochemical measurements, such as cyclic voltammetry or rotating disk electrode techniques, treat the electrode surface as uniformly active. This is misleading in the study of electrocatalysis on polycrystalline electrodes. Michaelis et al. characterized and modified the semiconductor surfaces with polycrystalline Ti/TiO_2 as an example, and reported that the electronic and the optical properties of the semiconducting TiO_2 films are closely associated with the texture of the substrate. The TiO_2 film thickness could be controlled by anodic potential applied during the illumination by means of focused UV-laser illumination. In addition, the film properties vary with the grain orientation in a systematic manner.[139] Zhu et al. reported the surface activity of freshly polished ASTM grade-7 titanium in an aerated, neutral solution of 0.1 M NaCl varies from region to region, and they proposed that the grain boundaries on Ti-7 have enhanced electrochemical activity compared with the oxide-covered TiO_2 by scanning electrochemical microscopy.[140]

Probing local electrochemical measurements at the electrode surfaces has been performed by different approaches. Yan et al. developed an approach to conduct electrochemical measurements on single crystal facets of a single-crystalline Au bead by employing a cone-shaped pipette tip in the electrochemical cell.[138] In addition, lithographic techniques have been used to prepare individual addressable electrodes, and the electrochemical measurements were carried out on selected grains on polycrystalline titanium surface.[141] Yu et al. investigated the facet-dependent electrochemical behavior of Co_3O_4 nanocrystals toward heavy metal ions adsorption by square wave stripping voltammetry and density-functional theory (DFT) calculations.[142] It was found that $Co_3O_4(111)$ facets could adsorb more metal ions than $Co_3O_4(100)$ facets, and DFT results suggested $Co_3O_4(111)$ has a relative larger adsorption energy, more adsorption sites, and a relative lower transition-state barrier than $Co_3O_4(100)$ toward the adsorption behavior of Pb ions. Other pipet-based imaging methods such as scanning micropipette contact method (SMCM)[143-144] and scanning electrochemical cell microscopy (SECCM)[145-146] have also demonstrated a capability for local electrochemical measurements. Recently, Unwin et al. reported an SECCM study coupled with electron backscatter diffraction in the investigation of the electrochemical activity of pseudo-single-crystal electrodes on platinum polycrystalline electrodes for the Fe^{2+}/Fe^{3+} redox reaction. The activity of Fe^{2+} oxidation was found to be grain-dependent in perchlorate medium, and the activity was greatly enhanced at grain boundaries in sulfate medium. However, the activity imaging with SECCM demands static point-by-pint measurements which is time-consuming and technically difficult.

In this study, we have established an approach to effectively produce Pt single-crystal surfaces in a comparatively simple and inexpensive procedure by metallurgical etching. Unlike single-crystal electrode preparation where only a single orientation surface is produced, several pseudo-single-crystal electrodes can be made in one etching experiment, which greatly enhanced the efficiency in the electrode fabrication process. Preparing well-defined crystallite facets requires attention to the electrolytic etching time and potential and depends on the composition and concentration of the etching solution, and the conditions of the electrode. The etching solutions, comprised of concentrated HCl and NaCl, exhibit high etching efficiency with relatively short etch times. Longer etching times resulted in the exposure of underlying mechanical polishing traces/scratches or erosion of the whole flat and smooth surface. In addition, it is demonstrated that heat treatment of polycrystalline platinum electrodes enables the electrolytic etching approach to be extended to unannealed Pt in addition to annealed electrodes.

The pseudo-single-crystal electrode facets prepared by electrolytic etching of polycrystalline platinum electrode was characterized by optical microscopy, optical profilometry, SEM, AFM, and EBSD. The grain boundaries and the surface topography of Pt crystallites on polycrystalline platinum electrodes were discerned by optical microscopy and SEM. The surface step depth and surface roughness due to etching was determined by AFM measurements, including 2D and 3D AFM maps and AFM line profiles. The examined step depth between two grains varied from tens of nm to several hundred nm, with a maximum surface step height of less than 500 nm. The crystallographic orientation of grains on the polycrystalline electrode surface was obtained from EBSD mapping. Etching rates of pseudo-single-crystal electrodes were evaluated with AFM measurement complemented by EBSD. It is evident that a correlation exists between the electrolytic etching rate and the crystallographic orientation of the platinum crystallite domains, and it is found that the etching rate is in the order of (110) < (111) < (100) where the Miller index represent the main contribution orientation.

In a study of the electrocatalysis of hydrogen oxidation reaction on an etched polycrystalline platinum electrode in sulfuric acid, the heterogeneity of the electrocatalytic activity of the polycrystalline platinum electrode surface is successfully visualized in a single scan experiment and displayed in vivid color contrast with scanning electrochemical microscopy imaging techniques. It is the first time that the electrocatalytic activity of high-index single-crystal surfaces is visualized toward HOR by means of SECM. The pattern of the electrochemical features found in the SECM image is well matched to the surface geometry (grain shape and size) revealed in optical and SEM micrographs. By comparing the SECM the current map to EBSD maps, it is evident that the variations in electrocatalytic activity of the hydrogen oxidation reaction depends on the crystallographic orientation of crystallite surfaces, which proves the structure sensitivity of platinum surface toward the HOR. The electrocatalytic activity of different single-crystal electrodes on a polycrystalline platinum substrate is generally determined to have an order of (111) > (110) > (100) where the Miller indices represent the terrace orientation of the higher-index single-crystal surfaces. It was demonstrated that a Pt stepped surface with (111) terraces had the highest electrocatalytic activity towards the HOR, following by a surface with (110) terrace, and a grain with (110) character. In addition, it is found that the surface catalytic activity for the HOR is in the order (332) < (100) < (510) < (410) < (310) < (431) < (322) < (332) for the seven pseudo-single-crystal electrodes with different crystallographic orientations.

Moreover, the impact of the presence of (110) steps on a crystallographic plane on the activity for the HOR is also observed as follows: high-index platinum surfaces with the same atomic width of (111) terrace but with a (110) step show higher activity than ones with (100) steps. In addition, an activity order of Pt(310) > Pt(410) > Pt(510) > Pt(100) is observed with a decrease in step-atom density. It has also been demonstrated that the catalytic activity of single-crystal grains have a potential-dependent behavior. The activity of the grains toward the HOR decreases as the substrate potential increases, possibly due to the bisulfate anion adsorption and oxide growth at the Pt substrate electrode surface.

A quantitative analysis of local reactivity of the pseudo-single-crystal surfaces on a polycrystalline platinum electrode surface for HOR was obtained by fitting the SECM current-distance experimental approach curves to an approximate analytical expression for the curve derived by Lefrou. et al.[134-136] The results show the HOR activity decreases logarithmically with decreasing substrate potential. The rate constants extracted from curve fitting for HOR at different potentials indicate the reaction is controlled by diffusion at −0.5 V, and it is under kinetic control at the more positive potentials.

Overall, the structure-activity relationship of pseudo-single-crystal electrodes is successfully established for the electrolytic reaction in HCl/NaCl etching solutions and the electrocatalysis of the HOR in sulfuric acid at polycrystalline platinum electrode surface by AFM, EBSD, and SECM techniques.

This approach overcomes challenges in probing local electrochemistry at complex surfaces. It suggests a new strategy in preparing electrochemical sensing interfaces at polycrystalline metal electrodes, facilitates electrochemical measurements–such as kinetic study on high-index single-crystal surfaces, and provides a platform for structure-activity relationship studies of surface-sensitive reactions or electrocatalytically active metal materials.

REFERENCES

1. Askeland, D. R.; Phulé, P. P. *Essentials of Materials Science and Engineering*. Thomson Learning: Stamford, CT, 2004.

2. Brandon, D.; Kaplan, W. D. *Microstructual Characterization of Materials*. 2nd ed.; Wiley: Chichester, U.K., 2008.

3. Ashby, M. F. *Materials Selection in Mechanical Design*. Elsevier Butterworth-Heinemann: Burlington, MA, 2005.

4. Jiang, X.; Goodman, D. W. Correlations Between Structure And Reactivity Of Metal Surfaces. In *Studies in Surface Science and Catalysis*, Grasselli, R. K.; Sleight, A. W., Eds. Elsevier: 1991; Vol. 67, pp 291-300.

5. Christensen, P. A.; Hamnett, A. *Techniques and Mechanisms in Electrochemistry*. Blakie Academic & Professional: Glasgow, UK, 1994.

6. Sau, T. K.; Rogash, A. L. *Adv. Mater.* **2010,** *22*, 1781-1804.

7. Tian, N.; Zhou, Z.-Y.; Sun, S.-G. *J. Phys. Chem.* **2008,** *112*, 19801-19817.

8. Ye, S.; Vijh, A. K. *Electrochem. Commun.* **2003,** *5*, 272-275.

9. Fernández, J. L.; Walsh, D. A.; Bard, A. J. *J. Am. Chem. Soc.* **2004,** *127*, 357-365.

10. Lykhnytskyi, K. V.; Jaskula, M.; Barsukov, V. Z. In *Perspective Catalysts for the Hydrogen Oxidation Reaction in Fuel Cells*, Association for Hydrogen Energy in Ukraine: 2005; pp 986-989.

11. Lee, Y.-H.; Kim, G.; Joe, M.; Jang, J.-H.; Kim, J.; Lee, K.-R.; Kwon, Y.-U. *Chem. Commun.* **2010,** *46*, 5656-8.

12. Bron, M.; Flechter, S.; Hilgendorff, M.; Bogdanoff, P. J. *J. Applied. Electrochem.* **2002,** *32*, 211-216.

13. Jang, J.-H.; Kim, J.; Lee, Y.-H.; Pak, C.; Kwon, Y.-U. *Electrochim. Acta* **2009,** *55*, 485-490.

14. Al-Odail, F. A.; Anastasopoulos, A.; Hayden, B. E. *Phys. Chem. Chem. Phys.* **2010,** *12*, 11398-11406.

15. Zen, J.-M.; Wang, C.-B. *J. Electrochem. Soc.* **1994,** *141*, L51-L52.

16. Ralph, T. R.; Hogarth, M. P. *Platinum Metals. Rev.* **2002,** *46*, 3-14.

17. Somorjai, G. A.; Li, Y., *Introduction to Surface Chemistry and Catalysis*. Wiley: New York, NY, 2010.

18. Santos, E.; Schmickler, W. *Catalysis in Electrochemistry: From Fundamentals to Strategies for Fuel Cell Development*. Wiley: Hoboken, New Jersey, 2011.

19. Masel, R. I. *Principles of Adsorption and Reaction on Solid Surfaces*. Wiley: New York, NY, 1996.

20. Bogue, R. *Assembly Automation* **2009,** *29*, 313-320.

21. http://www.chem.qmul.ac.uk/surfaces/scc/scat1_2.htm (accessed 2013 Sep 08).

22. Caracciolo, R.; Schmidt, L. D. *J. Electrochem. Soc.* **1983,** *130*, 603-607.

23. Stamenkovic, V.; Marković, N. M.; P. N. Ross, J, *J. Electroanal. Chem.* **2001,** *500*, 44-51.

24. Marković, N. M.; Ross Jr, P. N. *Surf. Sci. Rep.* **2002,** *45*, 117-229.

25. Korzeniewski, C.; Climent, V.; Feliu, J. M. Electrochemistry at Platinum Single Crystal Electrodes. In *Electroanalytical Chemistry: A Series of Advances*, Bard, A. J.; Zoski, C. G., Eds. CRC Press: Boca Raton, FL, 2012; Vol. 24, pp 75-169.

26. Conway, B. E. *Interfacial Electrochemistry Theory, Experiment, and Applications*. Marcel Dekker: New York, NY, 1999; p 131.

27. Herrero, E.; Franaszczuk, K.; Wieckowski, A. *J. Phys. Chem.* **1994,** *98*, 5074-5083.

28. Housmans, T. H. M.; Koper, M. T. M. *J. Phys. Chem. B* **2003,** *107*, 8557-8567.

29. Housmans, T. H. M.; Wonders, A. H.; Koper, M. T. M. *J. Phys. Chem. B* **2006,** *110*, 10021-10031.

30. Lai, S. C. S.; Lebedava, N. P.; Housmans, T. H. M.; Koper, M. T. M. *Top. Catal.* **2007,** *46*, 320-333.

31. Tripkovic, A. V.; Popovic, K. D. *Electrochim. Acta* **1996,** *41*, 2385-2394.

32. Lebedava, N. P.; Koper, M. T. M.; Herrero, E.; Feiliu, J. M.; van Santen, R. A. *J. Electroanal. Chem.* **2000,** *487*, 37-44.

33. Lebedava, N. P.; Koper, M. T. M.; Feiliu, J. M.; van Santen, R. A. *J. Phys. Chem. B* **2002,** *106*, 12938-12947.

34. Garcia, G.; Koper, M. T. M. *Phys. Chem. Chem. Phys.* **2008,** *10*, 3802-3811.

35. Kuzume, A.; Herrero, E.; Feiliu, J. M. *J. Electroanal. Chem.* **2007,** *599*, 333-343.

36. Macia, M. D.; Campina, J. M.; Herrero, E.; Feiliu, J. M. *J. Electroanal. Chem.* **2004,** *564*, 141-150.

37. Tripkovic, D. V.; Strmcnik, D.; van der Vilet, D.; Stamenkovic, V.; Marković, N. M. *Faraday Discuss.* **2008,** *140*, 25-40.

38. Adzic, R. R.; Wang, J. X. *Electrochim. Acta* **2000,** *45*, 4203-4210.

39. Tarnowski, D. J.; Korzeniewski, C. *J. Phys. Chem. B* **1997,** *101*, 253-258.

40. Sun, S. G.; Chen, A. C.; Huang, T. S.; Li, J. B.; Tian, Z. W. *J. Electroanal. Chem.* **1992,** *340*, 213-226.

41. Lipkowski, J.; Ross, P. N. In *Electrocatalysis: Frontiers of Electrochemistry*, Wiley: New York, 1998.

42. Marković., N. M.; Ross, P. N. In *Interfacial Electrochemistry: Theory, Experiments and Applications*, Wieckowski, A., Ed. Marcel Dekker: New York, 1999; p 821.

43. Koper, M. T. M. Fuel cell Catalysis, A Surface Science Approach;. In *Electrocatalysis and Electrochemistry*, Wieckowski, A., Ed. Wiley: Hoboken, New Jersey, 2009.

44. Zoski, C. G. *J. Phys. Chem. B* **2003,** *10*7), 6401-6405.

45. Weng, Y.-C.; Hsieh, C.-T. *Electrochim. Acta* **2011,** *5*6, 1932-1940.

46. Marković, N. M.; Grgur, B. N.; Ross, P. N. *J. Phys. Chem. B* **1997,** *101*, 5405-5413.

47. Bagotzky, V. S.; Osetrova, N. V. *J. Electroanal. Chem. Interfacial Electrochem.* **1973,** *43*, 233-249.

48. Silverster, D. S.; Aldous, L.; Hardacre, C.; Compton, R. G. *J. Phys. Chem. B* **2007,** *111*, 5000-5007.

49. Gasteiger, H. A.; Marković, N. M.; Ross, P. N., Jr. *J. Phys. Chem.* **1995,** *99*, 16757-67.

50. Wang, C.; Chi, M.; Li, D.; van, d. V. D.; Wang, G.; Lin, Q.; Mitchell, J. F.; More, K. L.; Marković, N. M.; Stamenkovic, V. R. *ACS Catal.* **2011,** *1*, 1355-1359.

51. Ahmed, S.; Ji, S.; Petrik, L.; Linkov, V. M. *Appl. Sci.* **2004,** *20*, 1283-1287.

52. Wang, D.; Subban, C. V.; Wang, H.; Rus, E.; DiSalvo, F. J.; Abruña, H. D. *J. Am. Chem. Soc.* **2010**,*132*, 10218-10220.

53. Marković, N. M.; Sarraf, S. T.; Gasteiger, H. A.; Ross, P. N. J. *J. Chem. Soc., Faraday Trans.* **1996,** *92*, 3719-3725.

54. Marković, N. M.; Gasteiger, H. A.; Ross, P. N., Jr. *J. Phys. Chem.* **1995,** *99*, 3411-3415.

55. Nicholson, P. G.; Zhou, S.; Hinds, G.; Wain, A. J.; Turnbull, A. *Electrochim. Acta* **2009,** *54*, 4525-4533.

56. Barber, J. H.; Conway, B. E. *J. Electroanal. Chem.* **1999,** *461*, 80.

57. Barber, J. H.; Morin, S.; Conway, B. E. *J. Electroanal. Chem.* **1998,** *446*, 125.

58. Kita, H.; Gao, Y.; Nakato, T.; Hattori, H. *J. Electroanal. Chem.* **1994,** *373*, 177-83.

59. Bard, A. J.; Mirkin, M. V., Eds,; Scanning Electrochemical Microscopy. Marcel Dekker: New York, NY, 2001.

60. Sun, P.; Laforge, F. O.; Mirkin, M. V. *Phys. Chem. Chem. Phys.* **2007,** *9*, 802-23.

61. Lu, X.; Wang, Q.; Liu, X. *Anal. Chim. Acta* **2007,** *601*, 10-25.

62. Shao, Y. H.; Mirkin, M. V. *J. Phys. Chem. B* **1998,** *102*, 9915-9921.

63. Cannes, C.; Kanoufi, F.; Bard, A. J. *Langmuir* **2002,** *18*, 8134-8141.

64. Eckhard, K.; Schuhmann, W. *The Analyst* **2008,** *133*, 1486-97.

65. Mirkin, M. V.; Horrocks, B. R. *Anal. Chim. Acta* **2000,** *406*, 119-146.

66. Bard, A. J.; Mirkin, M. V., Eds,; Scanning Electrochemical Microscopy. 2nd ed.; CRC Press Taylor & Francis Group: Boca Raton, FL, 2012.

67. Wittstock, G.; Burchardt, M.; Pust, S. E.; Shen, Y.; Zhao, C. *Angew. Chem.* **2007,** *46*, 1584-617.

68. Wagner, F. T.; Ross, P. N., Jr. *J. Electroanal. Chem. Interfacial Electrochem.* **1988,** *250*, 301-20.

69. Adzic, R. R.; Marković, N. M. *J. Electroanal. Chem. Interfacial Electrochem.* **1979,** *102*, 263-70.

70. Schmidt, T. J.; Stamenkovic, V. R.; Lucas, C. A.; Marković, N. M.; Ross, P. N., Jr. *Phys. Chem. Chem. Phys.* **2001,** *3*, 3879-3890.

71. Hoshi, N.; Asaumi, Y.; Nakamura, M.; Mikita, K.; Kajiwara, R. *J. Phys. Chem. C* **2009,** *113*, 16843-16846.

72. Babic, B.; Gulicovski, J.; Gajic-Krstajic, L.; Elezovic, N.; Radmilovic, V. R.; Krstajic, N. V.; Vracar, L. M. *J. Power Sources* **2009,** *193*, 99-106.

73. Marković, N. M.; Sarraf, S. T.; Gasteiger, H. A.; Ross, P. N., Jr. *J. Chem. Soc., Faraday Trans.* **1996,** *92*, 3719-3725.

74. V. Stamenkovic; Marković, N. M.; Ross, P. N. *J Electroanal Chem* **2001,** *50*0, 44-51.

75. Jambunathan, K.; Shah, B. C.; Hudson, J. L.; Hillier, A. C. *J. Electroanal. Chem.* **2001,** *500*, 279-289.

76. Jayaraman, S.; Hillier, A. C. *Langmuir* **2001,** *17*, 7857.

77. Zhou, J. F.; Zu, Y. B.; Bard, A. J. *J. Electroanal. Chem.* **2000,** *491*, 22.

78. Bard, A. J.; Faulkner, L. R. Electrochemical Methods: Fundamentals and Applications. Wiley: New York, 2001.

79. Bard, A. J.; Fan, F. R.; Mirkin, M. V. Scanning Electrochemical Microscopy. In *Electroanalytical Chemistry*., Bard, A. J., Ed. Marcel Dekker: New York, NY, 1994; Vol. 18, pp 243-373.

80. Kucernak, A. R.; Chowdhury, P. B.; Wilde, C. P.; Kelsall, G. H.; Zhu, Y. Y.; WIlliams, D. E. *Electrochim. Acta* **2000,** *45*, 4483.

81. Xiang, X. D.; Sun, X. D.; Briceño, G. B.; Lou, Y. L.; Wang, K. A.; Chang, H. Y.; Wallace-Freeman, W. G.; Chen, S. W.; Schultz, P. G. *Science* **1995,** *268*, 1738.

82. Jayaraman, S.; Hillier, A. C. *J. Phys. Chem. B* **2003,** *107*, 5221-5230.

83. Goldstein, J.; Newbury, D. E.; Joy, D. C.; Lyman, C. E.; Echlin, P.; Lifshin, E.; Sawyer, L.; Michael, J. R. *Scanning Electron Microscopy and X-ray Microanalysis: A Text for Biologists, Materials Scientists, and Geologists.* Plenum Press: New York, NY, 1981.

84. Medevielle, A.; Hugon, I.; Dugne, O. *Microstruct. Sci.* **1998,** *26*, 26-29.

85. Boehm-Courjault, E. Electron Backscatter Diffraction: Principle and Applications.http://cime.epfl.ch/files/content/sites/cime2/files/shared/Files/Teaching/MSE_603_2012_spring/Chapter%207%20-%20EBSD.pdf (accessed Jan 07, 2013).

86. Stojakovic, D. *Process. Appl. Ceramics* **2012,** *6*, 1-13.

87. Wilkinson, A. J.; Britton, T. B. *Materials Today* **2012,** *15*, 366-376.

88. Nappé, J. C.; Maurice, C.; Grosseau, P.; Audubert, F.; Thomé, L.; Guilhot, B.; Beauvy, M.; Benabdesselam, M. *J. Eur. Ceram. Soc* **2011,** 31, 1503-1511.

89. Nowell, M. M.; Wright, S. I. *J. Microsc.* **2004,** *213*, 296-305.

90. Seo, Y.; Jhe, W. *Rep. Prog. Phys.* **2008,** *71*, 016101/1-016101/23.

91. Theory and Simulation of SPM. http://invsee.asu.edu/srinivas/spmmod/afm.html. (accessed Apr 23, 2013)

92. Gardner, C. E.; Macpherson, J. V. *Anal. Chem.* **2002,** *74*, 576A-584A.

93. Casero, E.; Vazquez, L.; Parra-Alfambra, A. M.; Lorenzo, E. *The Analyst* **2010,** *135*, 1878-903.

94. Chen, C. J. Introduction to Scanning Tunneling Microscopy. Oxford University Press: Oxford Scholarship Online, 2007.

95. Jalili, N.; Laxminarayana, K. *Mechatronics* **2004,** *14*, 907-945.

96. Nanotechnology/AFM. http://en.wikibooks.org/wiki/Nanotechnology/AFM (accessed Feb 27, 2013).

97. Sudbrake, C. *LaborPraxis* **2004,** *28*, 44-45.

98. Bruker AFM Probes. http://blog.brukerafmprobes.com/category/guide-to-spm-and-afm-modes/ (accessed Sep 27, 2013).

99. Demanet, C. M. *S. Afr. J. Sci.* **1997,** *93*, 298-302.

100. Contreras-Torres, F. F.; Basiuk, E. V.; Rodriguez-Galvan, A. *J. Adv. Microsc. Res.* **2010,** *5*, 159-176.

101. Gewirth, A. A.; LaGraff, J. R. Atomic Force Microscopy. In *Handbook of Surface Imaging and Visualization*, Hubbard, A. T., Ed. CRC Press: Boca Raton, FL 1995; pp 23-31.

102. Darling, R. M.; Meyers, J. P. *J. Electrochem. Soc.* **2003,** *150*, 1523-1527.

103. Parsons, R.; VanderNoot, T. *J. Electroanal. Chem.* **1998,** *257*, 9-45.

104. Ross, P. N. Surface Crystallography at the Metal-Solution Interface. VCH: New York, 1993.

105. Marković, N.; Gasteiger, H.; Ross, P. N. *J. Electrochem. Soc.* **1997,** *144*, 1591-1597.

106. Kita, h.; Ye, S. *J. Electroanal. Chem.* **1990,** *295*, 317-331.

107. Petzow, G. Metallographic Etching: Techniques for Metallography, Ceramography, Plastography. 2nd ed.; ASM International: Materials Park, OH, 1999; p 132.

108. Battaini, P. *Platinum Metals Rev.* **2011,** *55*, 71-72.

109. Priester, L. Grain Boundaries From Theory to Engineering. In Springer Series in Material Science, Springer: Dordrecht, 2013.

110. Loginov, Y. N.; Yermakov, A. V.; Grohovskaya, L. G.; Studenok, G. I. *Platinum Metals Rev.* **2007,** *51*, 178-184.

111. Pourbaix, M. Atlas of Electrochemical Equilibria in Aqueous Solutions. 2nd ed.; National Association of Corrosion Engineers: Houston, TX, 1974.

112. Liopis, J.; Sancho, A. *J. Electrochem. Soc.* **1961,** *108,* 720-726.

113. Bittles, J. A.; Littauer, E. L. *Corros. Sci.* **1970,** *10,* 29-41.

114. Schuldiner, S. *J. Electrochem. Soc.* **1961,** *108*, 384-387.

115. Jerkiewicz, G.; Vatankhah, G.; Lessard, J.; Soriaga, M. P.; Park, Y.-S. *Electrochim. Acta* **2004,** *49*, 1451-1459.

116. Wen, Y. N.; Zhang, H. M. *Solid State Commun*. **2007**, *144*, 163-167

117. Alpuche-Aviles, M. A.; Wipf, D. O. *Anal. Chem.* **2001,** *73*, 4873-4881.

118. Wightman, R. M.; Wipf, D. O. In *Electroanalytical Chemistry*, Bard, A. J., Ed. Marcel Dekker: New York, 1989; Vol. 15, pp 267-353.

119. Wipf, D. O.; Bard, A. J. *J. Electrochem. Soc.* **1991,** *138*, 469-474.

120. Zoski, C. G. Handbook of Electrochemistry. Elsevier: Oxford, UK, 2007.

121. Wipf, D. O. *Colloid Surf. A* **1994,** *93*, 251-261.

122. Seegmiller, J. C.; Buttry, D. A. *J. Electrochem. Soc.* **2003,** *150*, B413-B418.

123. Minguzzi, A.; Alpuche-Aviles, M. A.; Lopez, J. R.; Rondinini, S.; Bard, A. J. *Anal. Chem.* **2008,** *80*, 4055-4064.

124. Conway, B. E. In *Electrodes of Conductive Metallic Oxides*. Part B, Trasatti, S., Ed. Elsevier: The Netherlands, 1981; pp 433-519.

125. Jensen, M. B.; Guerard, A.; Tallman, D. E.; Bierwagen, G. P. *J Electrochem. Soc.* **2008,** *155*, C324-C332.

126. Marković, N. M.; Marinkovic, N. S.; Adzic, R. R. *J. Electroanal. Chem. Interfacial Electrochem.* **1988,** *241*, 309-28.

127. Schmidt, T. J.; Marković, N. M. In *Electrocatalysis of Inorganic Reactions: Pure Platinum Surfaces*, Taylor & Francis: 2012; pp 2032-2047.

128. Stamenkovic, V.; Marković, N. M. *Langmuir* **2001,** *17*, 2388-2394.

129. Hamann, C. H.; Hamnett, A.; Vielstich, W. *Electrochemistry*. Wiley: Verlag GmbH & Co. KGaA, Weinheim: 2007.

130. Biegler, T.; Rand, D. A. J.; Woods, R. *J. Electroanal. Chem.* **1971,** *29*, 269.

131. Zhou, J.; Zu, Y.; Bard, A. J. *J. Electroanal. Chem.* **2000,** *491*, 22-29.

132. Bockris, J. O'M; Srinivasan, S. *Fuel Cells: Their Electrochemistry*. McGraw-Hill: New York, 1969.

133. Cornut, R.; Bhasin, A.; Lhenry, S.; Etienne, M.; Lefrou, C. *Anal. Chem.* **2011,** *83*, 9669-9675.

134. Lefrou, C. *J. Electroanal. Chem.* **2007,** *601*, 94-100.

135. Cornut, R.; Lefrou, C. *J. Electroanal. Chem.* **2007,** *604*, 91-100.

136. Cornut, R.; Lefrou, C. *J. Electroanal. Chem.* **2008,** *621*, 178-184.

137. Wei, C.; Bard, A. J.; Mirkin, M. V. *J. Phys. Chem.* **1995,** *99*, 16033-16042

138 Yan, J. W.; Sun, C. F.; Zhou, X. S.; Tang, Y. A.; Mao, B. W. *Electrochem. Commun.* **2007**, 9, 2716-2720

139 Michaelis, A.; Kudelka, S.; Schultze, J. W. *Materials Research Society Symposium − Proceedings* **1997,** *451*, 289-300.

140 Zhu, R.; Qin, Z.; Noël, J. J.; Shoesmith, D. W.; Ding, Z. *Anal Chem* **2008**, *80*, 1437-1447.

141 König, U.; Davepon, B. *Electrochim. Acta.* **2001**, *47*, 149-160.

142 Yu, X. Y.; Meng, Q. Q.; Luo, T.; Jia, Y.; Sun, B.; Li, Q. X.; Liu, J. H.; Huang, X. J. *Sci. Rep.* **2013**, *3*, art. no. 2886.

143 Williams, C. G.; Edwards, M. A.; Colley, A. L.; Macpherson, J. V.; Unwin, P. R. *Anal. Chem.* **2009**, *81*, 2486-2495.

144 Day, T. M.; Unwin, P. R.; Macpherson, J. V. *Nano Lett.* **2007**, *7*, 51-57.

145 Ebejer, N.; Güell, A. G.; Lai, S. C. S.; McKelvey, K.; Snowden, M. E.; Unwin, P. R. *Ann. Rev. Anal. Chem.* **2013**, *6*, 329-351.

146 Aaronson, B. D. B.; Chen, C.; Li, H.; Koper, M. T. M.; Lai, S. C. S.; Unwin,P. R. *J. Am. Chem. Soc.* **2013**, *135*, 3873-3880.